energies

Wind Turbine Power Optimization Technology

Edited by
Francesco Castellani and Davide Astolfi
Printed Edition of the Special Issue Published in *Energies*

MDPI

Wind Turbine Power Optimization Technology

Wind Turbine Power Optimization Technology

Special Issue Editors

Francesco Castellani
Davide Astolfi

MDPI

Special Issue Editors

Francesco Castellani
Department of Engineering,
University of Perugia
Italy

Davide Astolfi
Department of Engineering,
University of Perugia
Italy

This is a reprint of articles from the Special Issue published online in the open access journal *Energies* (ISSN 1996-1073) (available at: https://www.mdpi.com/journal/energies/special_issues/Wind_Turbine_Power_Optimization).

For citation purposes, cite each article independently as indicated on the article page online and as indicated below:

LastName, A.A.; LastName, B.B.; LastName, C.C. Article Title. *Journal Name* **Year**, *Article Number*, Page Range.

Cover image courtesy of Francesco Castellani.

Contents

About the Special Issue Editors

Francesco Castellani is an Associate Professor in Machine Engineering at the University of Perugia where he is teaching Applied Mechanics in the Bachelor and Master Degree program in Mechanical Engineering. He is also a member of the Board of the PhD Program in Information Technology and Industrial Engineering of the University of Perugia. Since 2014 he has also been the Scientific Coordinator for the Wind Tunnel Test laboratory "R. Balli" at the University of Perugia. His main research interests include mechanical system dynamics, rotating machines health monitoring, hydraulic and pneumatic systems, and vehicle aerodynamics. He has been involved in wind energy research and industry since 1999. At first he mainly worked on resource assessment through experimental measurements and CFD numerical modeling. Then, the focus of his research shifted to wind turbines and wind farms with the study of operation conditions in complex terrains and wake interactions. He is also currently working on machine vibrations and aeroelasticity; scaled model wind tunnel testing; fault diagnosis; and condition monitoring. Francesco Castellani has been reviewing articles for many journals within the research fields of energy, mechanical systems, and applied fluid dynamics. He is also a member of the Editorial Boards of Energies (MDPI) and Applied Mechanics (MDPI). His scientific production includes almost one hundred research articles indexed in Scopus with an overall of 733 citations and an H-Index of 17.

Davide Astolfi is a post-doctoral fellow at the Department of Engineering of the University of Perugia. He earned a Ph.D. in Physics at the University of Perugia in 2008. Since 2012, his research activities have dealt mainly with wind energy and he has been regularly cooperating with international scholar partnerships and the wind turbine technology industry. He has been contributing to several aspects of wind turbine behaviour characterization through the analysis of operation data: he has addressed the issues of wind turbine performance control, especially in harsh conditions as wakes in complex terrain; he has also studied the on-site assessment of wind turbine control and aerodynamic optimization technology through innovative applications of statistical methods; he has analysed the yawing behaviour of wind turbines and studied the detection of systematic yaw misalignment; he has studied the use of drive-train sub-component temperature measurements for wind turbine condition monitoring. Furthermore, he has researched innovative wind turbine vibration measurements and signal processing techniques with the objective of gears and bearings condition monitoring. His expertise in experimental wind turbine analysis has been corroborated by regular feedback with theoretical and numerical models, and on these grounds he has developed a wide expertise in applied mechanics methodologies and condition monitoring, aero-elastic wind turbine simulations, and computational fluid dynamics. He regularly contributes and participates in the most renowned international wind energy conferences and workshops organized by the European Academy of Wind Energy. He is the author of around 70 Scopus-indexed articles and he has served as Guest Editor of several scientific journals: Energies, Machines, Clean Technologies, and Stats and Applied Mechanics from MDPI; Diagnostyka from the Polish Society of Technical Diagnostics.

Editorial on Special Issue "Wind Turbine Power Optimization Technology"

Francesco Castellani *,† and **Davide Astolfi** †

Department of Engineering, University of Perugia, Via G. Duranti 93, 06125 Perugia, Italy;
davide.astolfi@unipg.it

* Correspondence: francesco.castellani@unipg.it; Tel.: +39-075-585-3709

† These authors contributed equally to this work.

Abstract: This Special Issue collects innovative contributions in the field of wind turbine optimization technology. The general motivation of the present Special Issue is given by the fact that there has recently been a considerable boost of the quest for wind turbine efficiency optimization in the academia and in the wind energy practitioners communities. The optimization can be focused on technology and operation of single turbine or a group of machines within a wind farm. This perspective is evidently multi-faced and the seven papers composing this Special Issue provide a representative picture of the most ground-breaking state of the art about the subject. Wind turbine power optimization means scientific research about the design of innovative aerodynamic solutions for wind turbine blades and of wind turbine single or collective control, especially for increasing rotor size and exploitation in offshore environment. It should be noticed that some recently developed aerodynamic and control solutions have become available in the industry practice and therefore an interesting line of development is the assessment of the actual impact of optimization technology for wind turbines operating in field: this calls for non-trivial data analysis and statistical methods. The optimization approach must be 360 degrees; for this reason also offshore resource should be addressed with the most up to date technologies such as floating wind turbines, in particular as regards support structures and platforms to be employed in ocean environment. Finally, wind turbine power optimization means as well improving wind farm efficiency through innovative uses of pre-existent control techniques: this is employed, for example, for active control of wake interactions in order to maximize the energy yield and minimize the fatigue loads.

Keywords: wind energy; wind turbines; control and optimization; aerodynamics; structures

---

Wind turbines are widely recognized as one of the most efficient technologies for electrical energy production from a renewable source and the expectation is that the efficiency is going to further grow, primarily because of the increasing rotor size and secondarily because of the technology optimization.

Wind turbine technology optimization has therefore become in the latest years a core topic in wind energy research. The purpose of this Special Issue is collecting innovative contributions to the multi-faced issue of wind turbine power optimization technology.

The power output of a wind turbine has a complex dependence on ambient conditions and operation parameters; nevertheless it can fairly be stated that the most important aspect for power extraction optimization is the aerodynamic efficiency. For this reason, a remarkable line of research deals with optimization of wind turbine blades technology. For wind farms already operating, a typical intervention is blades retrofitting through the installation of active (like Air Jet Vortex Generators) or passive (Vortex Generators, Gurney Flaps and so on) flow control devices. For new installations, in the context of wind turbine design, it is important to optimize the blade design and the flow control

devices for increasing rotor size and efficiency also in particular in the context of floating wind turbines, whose technology should be appropriate for exploitation in ocean environment.

Two contributions about the above aspects are featured in the present Special Issue.

The study in [1] is devoted to the optimization of the Gurney Flaps for a DU91W(2)250 airfoil: Reynolds-Averaged Navier–Stokes simulations are performed with Gurney Flaps from 0.25% to 3% of the chord length at angles of attack from $-6°$ to $8°$, assuming a Reynolds number Re $= 2 \times 10^6$. The highest increase of lift-to-drag ratio is obtained when the Gurney Flaps length is 0.5% of the chord length and the angle of attack is $2°$; the influence of the Gurney Flaps is shown to decrease when the angle of attack exceeds $5°$. The main lesson from the study in [1] is that a fixed Gurney Flaps length would not reach the optimal lift-to-drag ratio for all the values of the angle of attack: this suggests that Gurney Flaps could more profitably be employed as active flow control devices (differently from their typical use), adapting their size on the working conditions. For this reason, in [1] an Artificial Neural Network has been trained and employed for predicting the aerodynamic efficiency of the airfoil in terms of the lift-to-drag ratio.

The objective of the study in [2] is the optimization of the blades of the NREL 5MW wind turbine: this model has been analyzed in several studies and it stands as a scientific prototype for large offshore wind turbines. The methods proposed in [2] are remarkably innovative: a Particle Swarm Optimization algorithm combined with the FAST (Fatigue, Aerodynamics, Structures and Turbulence) software (developed at the NREL) is employed for blade design optimization and the results are compared against traditional blade design methods (like the Glauert method). Furthermore, the aerodynamic performance of the blades is optimized for application to floating wind turbines, taking into account the motion of the platform caused by the sea waves; a meaningful site is selected as test operation site and the main result is that the proposed optimized blade design can provide a 3.8% improvement of the maximum power of the wind turbine.

The design of innovative wind turbine controls is a keystone of technology optimization. Several solutions have recently become available also in the industry and deal, for example, with the optimization of the yaw control (in order to maximize the operation time with zero or almost zero yaw angle) and of the pitch control (especially near the cut-in and rated speeds). The present Special Issue features a contribution about innovation design of wind turbine control and the investigation object is once again the NREL 5MW: in [3], the proposed approach is a nonlinear economic model predictive control which considers the tower and gearbox dynamics. The optimization of this control considers all the actuator constraints (pitch angle, and torque constraints with their rate of change constraints) and the hard constraints (rotor speed, generator speed, and electrical power): the objective is achieving the maximum generated power against the competing penalties constituted substantially by the fatigue loads. Several sample configurations are analyzed through FAST simulations, in order to support the practical application of the proposed control.

Another meaningful contribution dealing with the NREL 5MW wind turbine is included in this Special Issue: in the context of floating wind turbines technology, the object of [4] is the design optimization of a tension leg platform through the addition of further mooring lines with respect to a traditional system. The rationale for this choice is increasing the horizontal stiffness of the system and thereby reducing the dominant motion of the platform. An experimental analysis is performed by applying Froude scaling: the experiment set up is a lab-scale wave flume generating regular periodic waves by means of a piston-type wave generator. Two main results are achieved: it is shown that the optimized design in general improves the stability of the platform and reduces the overall motion of the system; furthermore an extreme wave conditions analysis is conducted and it results that the optimized design reduces the wave loads.

It should be noticed that some innovative aerodynamic and control design solutions have recently become available in the wind energy practitioners community and this has stimulated a further line of research, thanks to the availability of large amounts of Supervisory Control And Data Acquisition (SCADA) data from operating wind farms: the objective is the on-site assessment of wind turbine

optimization technology through operation data analysis. This task is challenging because practically it translates in the necessity of comparing the measured power against a reliable estimate of how much the power would have been if the upgrade had not taken place. Therefore, a precise data-driven model for the power of the wind turbines of interest must be constructed and trained with pre-upgrade data sets and this is complex because the power of a wind turbine has a multivariate dependence on ambient conditions and working parameters and because there commonly is a wind field data quality issue as regards cup anemometers mounted behind the wind turbine rotors. These critical points are circumvented in an innovative manner in the study [5], included in the present Special Issue. The underlying idea is based on the fact that power optimization technologies are typically tested on pilot wind turbines and therefore the remainder wind turbines from a given wind farm can be employed as reference. In [5], it is shown that a multivariate linear model is adequate for the task of interest: the power of the upgraded wind turbines is modelled as linear function of the operation variables of the nearby wind turbines. Several test cases have been addressed in [5] and the main result is that aerodynamic optimization technologies can improve the energy up to the order of 2% of the Annual Energy Production, while control optimization typically weights for the order of 1%.

One of the most timely topics in wind energy literature is wind farm control: the general idea is upstream wind turbine wakes active control, in order to maximize energy yield and minimize loads. At this aim, it is of fundamental importance to develop computationally affordable techniques for wakes modelling. The present Special Issue features a contribution about the topic of wake modelling: in particular, the object of [6] is the modelling of multiple upwind wakes. The peculiarity of this situation is that the higher turbulence level and shear stress profile generated by upwind turbines in the superposed area leads to faster wake recovery: this implies that it is not appropriate to model the multiple wakes as a simple superposition of wakes. In [6], a mixing coefficient is introduced in the energy balance wake superposition model. The correction coefficient depends on the average distance, in units of rotor diameters, among the sequence of downstream wind turbines. The proposed model is evaluated using data from the Lillgrund and the Horns Rev I offshore wind farms, which are two typical test cases for wake models validation in wind energy literature.

Finally, the present Special Issue features a contribution about the optimization of Vertical-Axis Wind Turbines (VAWT). The object of the study in [7] is dynamic stall control of VAWTs through plasma actuation. Unsteady Reynolds-Averaged Navier-Stokes (URANS) simulations are used to study the dynamic stall phenomenon of VAWT at different tip speed ratios, and the azimuthal position corresponding to the start and end of dynamic stall is found. The main result of [7] is that pulsed plasma actuation can be profitable for enhancing the power extraction efficienct of VAWTs and the actuation from $60°$ to $120°$ is optimal.

In summary, this Special Issue presents remarkable research activities in the timely subject of wind turbine power optimization technology, covering various aspects on single turbine technology as well as wind farm and site optimal exploitation. The collection of seven research papers is believed to benefit readers and contribute meaningfully to the wind power industry.

References

1. Aramendia, I.; Fernandez-Gamiz, U.; Zulueta, E.; Saenz-Aguirre, A.; Teso-Fz-Betoño, D. Parametric Study of a Gurney Flap Implementation in a DU91W (2) 250 Airfoil. *Energies* **2019**, *12*, 294. [CrossRef]
2. Ma, Y.; Zhang, A.; Yang, L.; Hu, C.; Bai, Y. Investigation on optimization design of offshore wind turbine blades based on particle swarm optimization. *Energies* **2019**, *12*, 1972. [CrossRef]
3. Kong, X.; Ma, L.; Liu, X.; Abdelbaky, M.A.; Wu, Q. Wind Turbine Control Using Nonlinear Economic Model Predictive Control over All Operating Regions. *Energies* **2020**, *13*, 184. [CrossRef]
4. Song, J.; Lim, H.C. Study of Floating Wind Turbine with Modified Tension Leg Platform Placed in Regular Waves. *Energies* **2019**, *12*, 703. [CrossRef]
5. Astolfi, D.; Castellani, F. Wind turbine power curve upgrades: part II. *Energies* **2019**, *12*, 1503. [CrossRef]
6. Shao, Z.; Wu, Y.; Li, L.; Han, S.; Liu, Y. Multiple Wind Turbine Wakes Modeling Considering the Faster Wake Recovery in Overlapped Wakes. *Energies* **2019**, *12*, 680. [CrossRef]
7. Ma, L.; Wang, X.; Zhu, J.; Kang, S. Dynamic Stall of a Vertical-Axis Wind Turbine and Its Control Using Plasma Actuation. *Energies* **2019**, *12*, 3738. [CrossRef]

Parametric Study of a Gurney Flap Implementation in a DU91W(2)250 Airfoil

Iñigo Aramendia [1], Unai Fernandez-Gamiz [1,*], Ekaitz Zulueta [2], Aitor Saenz-Aguirre [2] and Daniel Teso-Fz-Betoño [2]

[1] Nuclear Engineering and Fluid Mechanics Department, University of the Basque Country UPV/EHU, Nieves Cano 12, 01006 Vitoria-Gasteiz, Spain; inigo.aramendia@ehu.eus
[2] Automatic Control and System Engineering Department, University of the Basque Country UPV/EHU, Nieves Cano 12, 01006 Vitoria-Gasteiz, Spain; ekaitz.zulueta@ehu.eus (E.Z.); asaenz012@ikasle.ehu.eus (A.S.-A.); daniel.teso@ehu.eus (D.T.-F.-B.)
*   Correspondence: unai.fernandez@ehu.eus

Abstract: The growth in size and weight of wind turbines over the last years has led to the development of flow control devices, such as Gurney flaps (GFs). In the current work, a parametric study is presented to find the optimal GF length to improve the airfoil aerodynamic performance. Therefore, the influence of GF lengths from 0.25% to 3% of the airfoil chord c on a widely used DU91W(2)250 airfoil has been investigated by means of RANS based numerical simulations at Re = 2×10^6. The numerical results showed that, for positive angles of attack, highest values of the lift-to-drag ratio C_L/C_D are obtained with GF lengths between 0.25% c and 0.75% c. Particularly, an increase of 21.57 in C_L/C_D ratio has been obtained with a GF length of 0.5% c at 2° of angle of attack AoA. The influence of GFs decreased at AoAs larger than 5°, where only a GF length of 0.25% c provides a slight improvement in terms of C_L/C_D ratio enhancement. Additionally, an ANN has been developed to predict the aerodynamic efficiency of the airfoil in terms of C_L/C_D ratio. This tool allows to obtain an accurate prediction model of the aerodynamic behavior of the airfoil with GFs.

Keywords: wind turbine; flow control; Gurney flap; aerodynamics; ANN

1. Introduction

The wind power capacity installed in the last years has been showing an increase and, consequently, the requirement for bigger rotor wind turbines is becoming increasingly more necessary. This growth in size and weight of the wind turbines results in longer rotor blades which cannot be controlled as they were some years ago. Large wind turbines are exposed to severe structural and fatigue loads that must be reduced by means of the use of new flexible-soft materials and with novel load control techniques. Johnson et al. [1] gathered most of the main flow control devices with potential to be applied in wind turbines, assuring a better efficiency and a safe operation under a variety of adverse atmospheric conditions.

Flow control devices were first researched and developed for the aeronautical field with promising results; see the study of Taylor [2]. Then, the aim was to introduce and optimize them for their implementation in wind turbines to improve rotor blades' aerodynamic performance as well as to reduce fatigue loads. Wood [3] developed a scheme to classify the different concepts involved in all flow control devices such as their location, operation principle or working conditions. Aramendia et al. [4] provided an overview of how these devices are classified into passive and active, depending on their operating principle. Active flow control devices need a secondary power source for their activation, while passive flow control devices, as the Gurney flaps (GFs) of the current study, do not require

---

external energy consumption. Other passive devices such as the vortex generators (VGs) have also been studied extensively. Fernandez-Gamiz et al. [5,6] performed numerical simulations to study the characteristics of the primary vortex downstream of a rectangular VG along with a prediction model.

Due to their low cost, simplicity and reliable performance, GFs are being taken into consideration within passive flow control devices, showing promising results to extend the lifetime of future wind turbines [7]. A GF consists of a small tab placed normal to the airfoil surface and close to the trailing edge, either in the upper or in the lower side. The size of these GFs, measured with respect to the airfoil chord length (*c*), usually varies from 0.1% *c* and 3% *c*. They were first used in 1971 by Daniel Gurney, a race car driver who noticed improvements in cornering speeds and in the stability of his vehicle as a consequence of an increase in the downforce. Liebeck [8] discussed first this application and, subsequently, several experiments were carried out by Jeffrey et al. [9] on a NACA 0012 airfoil to investigate the effects of GFs and how they provide a lift improvement and a drag reduction once properly sized. They have been more widely researched for lift enhancement in aeronautics, where their advantages and applications were extensively studied by Wang et al. [10] Additionally, Pastrikakis et al. [11] compared the performance of a helicopter rotor with GFs at low and high forward flight speeds. Tang et al. [12], working with a NACA 0012 airfoil as well, studied a fixed and an oscillating trailing edge GF with the aim of evaluating the aerodynamics loadings by means of an incompressible Navier-Stokes code. Lee et al. [13] also studied the aerodynamic characteristics and the impact of GFs installed in a NACA 0015 along with a trailing edge flap. Different GFs heights and perforations were analyzed using particle image velocimetry (PIV) to measure the development of the tip vortex generated. According to Shukla et al. [14], the implementation of GFs in NACA0012 and NACA0015 symmetrical airfoils results in an improvement in the lift coefficient and lift force. Cole et al. [15] showed with different GF heights the importance of the airfoil shape in the aerodynamic performance of the airfoil. The influence of passive devices such as VGs and GFs was also studied by Fernandez-Gamiz et al. [16]. This work evaluated the improvement of a 5 MW wind turbine in terms of power output. Multiple device configurations and wind speed realizations were studied with the results showing an overall increase on the average power output of the wind turbine. Astolfi et al. [17] presented three test cases to evaluate the wind turbine power curve upgrades under different possible scenarios through operational data. In addition, a multivariate linear method for selecting the most appropriate input for modeling a given output was proposed by Terzi et al. [18] and applied to a multi-megawatt wind turbine with different passive flow control devices installed.

GFs have also been studied as active flow control devices, as shown in the work of Camocardi et al. [19], where the characteristics and structures of the flow pattern downstream the airfoil in the near wake were experimentally investigated. Recently, Han et al. [20] analyzed the influence of fixed and retractable GFs in the performance of variable speed helicopter rotors. Their results showed that both fixed and retractable GFs enhanced the performance of the rotor and expanded the flight envelope. However, the retractable one led to a better behavior in rotor power savings. In the wind turbine research field, the goal of this type of devices is to increase the lift on the rotor blades and, therefore, to increase the mechanical torque applied by the wind in the rotor. A lift enhancement of nearly 15% was observed in the study of Storms et al. [21] with a GF length of 0.5% *c* on a NACA 4412. Similarly, in the work of Mohammadi et al. [22], lift improvements were achieved with different GF shapes when compared to the clean DU91W(2)250 airfoil. Numerical methods have been developed and improved over the last years to study, as shown in the work of Gebhardt et al. [23], to study the behavior of large horizontal-axis wind turbines. Computational Fluid Dynamic (CFD) techniques are also frequently used to study the advantages and limitations of different flow control devices [24]. Recently, Woodgate et al. [25] used an in-house CFD solver to evaluate the implementation of GFs on wings and rotors. Different methods of modeling a GF were discussed and 2D cases were simulated to compare thick and infinitely thin GFs. Furthermore, they tested the solver also with 3D cases including rotors in hover and forward flight. In the study of Fernandez-Gamiz et al. [26], CFD simulations were made to find the optimal position of a microtab to improve the power output of a 5 MW wind turbine.

Additionally, Fernandez-Gamiz et al. [27] carried out a parametric study to find the most favorable dimension of a GF on a S810 airfoil by means of Proper Orthogonal Decomposition (POD) methods.

A parametric study is presented in the present work to analyze the effect of the GF length on the aerodynamic performance in a widely used DU91W(2)250 airfoil in multi-megawatt Horizontal Axis Wind Turbines (HAWT). In order to achieve this purpose, numerical RANS based simulations have been made and validated with the wind tunnel experimental data provided by Timmer et al. [28]. In addition, an Artificial Neural Network (ANN)-based model is presented to predict the effects of GFs on the aerodynamic efficiency in the DU91W(2)250 airfoil.

2. Numerical Setup

The behavior of the implementation of GFs was studied by means of Computational Fluid Dynamic (CFD) tools. In the current work, the commercial code STAR CCM+ v.11.02 [29] has been chosen to simulate the behavior of different GF lengths on a DU91W(2)250 airfoil.

The UpWind algorithm was employed for the pressure-velocity coupling and a linear upwind second order scheme was used to discretize the mesh. The numerical simulations were performed in steady state and ran fully turbulent using Reynolds Averaged Navier-Stokes (RANS) equations. Specifically, the Menter [30] k-ω SST shear stress turbulence model was used since it leads to a significant improvement in handling non-equilibrium boundary layer regions such as those close to separation, as addressed, as addressed by Kral [31] and Gatski [32]. This turbulent model combines both the standard k-ε model and k-ω model, retaining the properties of k-ω close to the wall and gradually blending into the standard k-ε model away from the wall. Mayda et al. [33] presented different tab configurations applying RANS calculations with the SST turbulence model. An O-mesh domain was defined for the numerical simulations, where the size of the computational domain was set to be 42 times the airfoil chord length c, R = 42 c, according to the recommendation of Sørensen et al. [34].

All the simulations were performed with a Reynolds number of Re = 2×10^6. The generation of an optimized grid represents the most important step before running the numerical solution in order to achieve reliable results. The grid domain consists of 65348 structured elements, where the height of the first cell normalized by the airfoil chord length was determined to be $\Delta z/c$ of 1.35×10^{-6}. The stretching in both normal and chord-wise direction is achieved by *tanh* functions based on Vinokur [35]. With the aim of resolving the viscous sublayer inside the turbulent boundary layer, the mesh was designed to achieve a dimensionless wall distance $y+$ at the first node adjacent to the airfoil wall less than 1 ($y+ < 1$). Figure 1 shows the cell distribution close to the trailing edge of the airfoil and around the GF, where the mesh refinement plays a major role due to the high velocity gradients expected in this region.
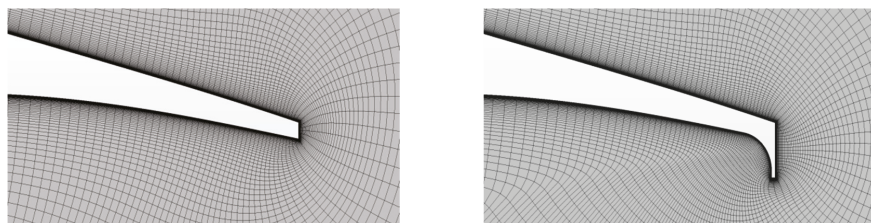

Figure 1. Mesh distribution on the trailing edge; with the clean airfoil and with a GF of 1.5% *c* implemented.

The walls of the airfoil and the GFs were set as non-slip boundary type. The validation of the numerical simulations without the implementation of the GF on the DU91W(2)250 airfoil was carried out with the wind tunnel results obtained by Timmer [28].

A mesh dependency study was made by means of the Richardson's extrapolation to verify that the solution obtained numerically is not dependent on the mesh size, following the procedure carried out by Fernandez-Gamiz et al. [27]. Three different grids were created with a mesh refinement ratio of 2. A fine, medium and coarse mesh of 65348, 32674 and 16337 cells have been designed, respectively. The results are summarized in Table 1, where RE indicates Richardson's extrapolation solution, p defines the order of accuracy and R the ratio of error. R values less than 1 were obtained, indicating that we are within the asymptotic range of convergence for all angles of attack. Figure 2 illustrates the lift-to-drag ratios achieved with each mesh level. The fine mesh provided the best results compared with the experimental wind tunnel results of Timmer et al. [28]. Thus, the fine mesh was used in the numerical simulations presented in the current work.

Table 1. Mesh dependency study results.

AoA	Mesh			Richardson Extrapolation		
	Coarse	Medium	Fine	RE	p	R
−6	−35.09	−49.94	−53.98	−52.47	1.87	0.27
−5	−25.97	−37.36	−39.95	−39.19	2.13	0.23
−4	−15.62	−22.35	−24.04	−23.47	2.00	0.25
−3	−4.86	−6.72	−7.15	−7.02	2.12	0.23
−2	6.24	8.98	9.61	9.42	2.13	0.23
−1	16.90	24.18	26.00	25.39	2.00	0.25
0	28.53	39.43	41.95	41.19	2.12	0.23
1	37.37	53.47	57.50	55.14	1.44	0.37
2	47.24	66.87	72.68	70.23	1.75	0.30
3	56.90	78.79	87.54	81.70	1.32	0.40
4	66.38	95.49	102.13	100.16	2.13	0.23
5	74.38	105.86	114.44	111.22	1.87	0.27
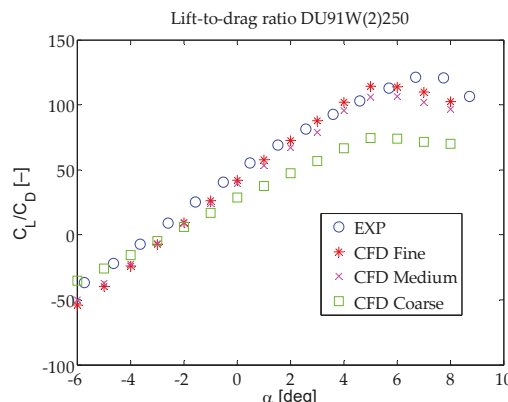
**Figure 2.** Results of the lift-to-drag ratio with each mesh level of the numerical simulations (CFD) vs. the experimental data of the DU91W(2)250 clean airfoil without the implementation of any GF.

Both lift and drag dimensionless coefficients were calculated with the Equations (1) and (2), respectively:

$$C_L = \frac{L}{\frac{1}{2}\rho U_\infty^2 c} \tag{1}$$

$$C_D = \frac{D}{\frac{1}{2}\rho U_\infty^2 c} \tag{2}$$

An air density value of ρ = 1.204 kg/m^3 was set, the dynamic viscosity was defined by μ = 1.855 $\times$ 10^{-5} Pa$\cdot$s and the free stream velocity corresponds to U_∞ = 30 m/s. The airfoil chord length is c = 1 m. Since the numerical simulations have been performed in two-dimensions, the parameters L and D represent the lift and drag forces per unit of area.

Gurney Flap Layout

The position and size of the GF is displayed in Figure 3. The dimension c represents the airfoil chord length and the dimension y the GF length. Twelve cases have been considered depending on the GF length, which is expressed as a percentage of the airfoil chord length, as shown in Table 2. Each case has been studied for fifteen different angles of attack, from $-6°$ to $8°$. The combination of all these GF positions for each angle of attack gives 195 different cases to study. All these cases have been designed following the procedure of previous studies carried out by Fernandez-Gamiz et al. [26,27]. The airfoil without any flow control device was also taken into account and simulated in order to compare the influence of the GFs on the airfoil aerodynamic performance.
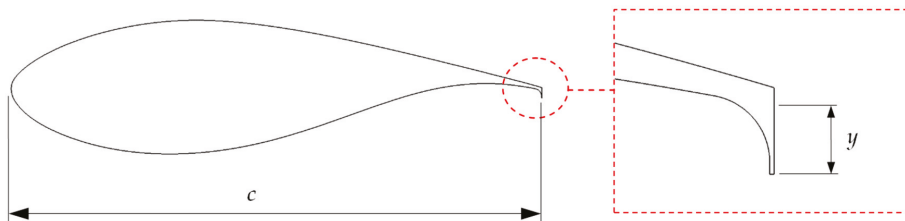

Figure 3. Detailed view of GF on a DU91W(2)250.

Table 2. Test cases considered in the study.

Test ID	TEST CASE	y (% c)
0	DU91W250	no GF
1	DU91W(2)250GF025	0.25
2	DU91W(2)250GF05	0.50
3	DU91W(2)250GF075	0.75
4	DU91W(2)250GF1	1.00
5	DU91W(2)250GF125	1.25
6	DU91W(2)250GF15	1.50
7	DU91W(2)250GF175	1.75
8	DU91W(2)250GF2	2.00
9	DU91W(2)250GF225	2.25
10	DU91W(2)250GF25	2.50
11	DU91W(2)250GF275	2.75
12	DU91W(2)250GF3	3.00

3. Results

The influence of the GF length was evaluated with the lift-to-drag ratio C_L/C_D for every angle of attack α studied, as illustrated in Figure 4. For each AoA, the evolution of the lift-to-drag ratio C_L/C_D with the GF length was compared with the clean airfoil case, i.e., no GF implementation. With regard to negative AoAs, from $-6°$ to $-4°$, as the GF length increases the lift-to-drag ratio increases as well. In all these cases the effect of the GF enhances the aerodynamic efficiency of the airfoil, except for the case of $-6°$ with a GF length of 0.25% c. However, in the range of AoAs from $-3°$ to $-1°$, a peak value of C_L/C_D is achieved before the maximum GF length of 3% c. For $-3°$ of AoA, a C_L/C_D ratio of 18.99 was obtained with a GF length of 2% c. Similarly, the peak values of C_L/C_D for $-2°$ and $-1°$ of AoA correspond to GF lengths of 1.5% c and 1% c, respectively.

On the other hand, a different behavior is observed for positive angles of attack. From 0° to 3°, the influence of the GF length on the C_L/C_D ratio follows the same pattern. With 0° of AoA, a maximum C_L/C_D value of 61.75 is obtained corresponding to a GF length of 1% *c*. Furthermore, the optimal GF length for 1° of AoA corresponds to 0.75% *c* with a C_L/C_D ratio of 78.91. As the angle of attack increases larger C_L/C_D maximum values are obtained, 92.37 and 102.65 for 2° and 3° of AoA, respectively. As can be seen from the plots at 2° and 3° of AoA, the effect of the GF is not favorable for all lengths. For 2° of AoA, GFs with lengths of 2.75% *c* and 3% *c* do not provide an increase in the C_L/C_D ratio compared with the clean airfoil. Similarly, in the case of 3° of AoA, GF lengths larger than 2% *c* do not present beneficial effects in the aerodynamic performance of the airfoil.
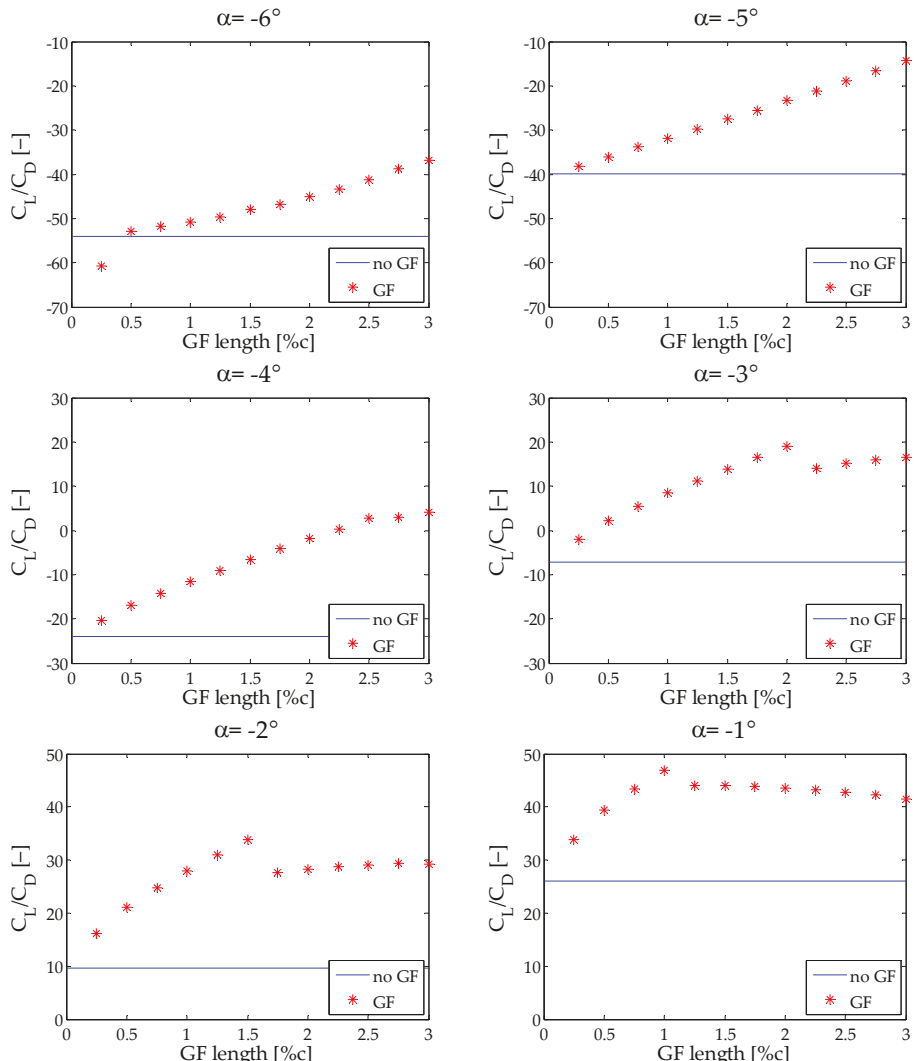

**Figure 4.** *Cont.*
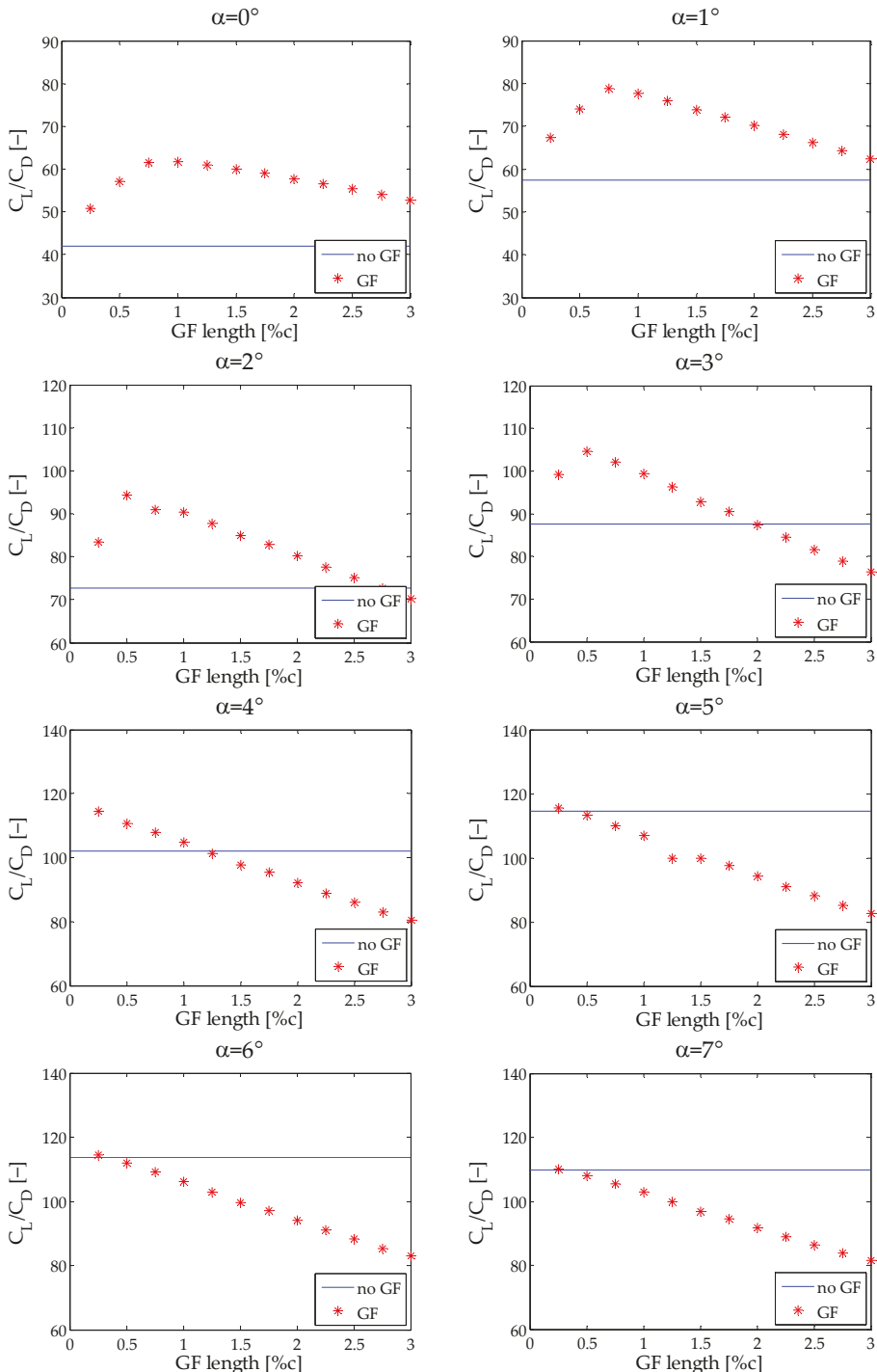
Figure 4. *Cont.*
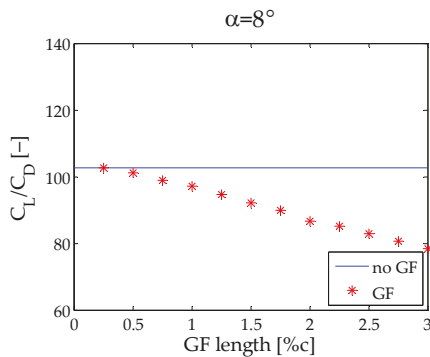
Figure 4. Lift-to-drag ratio (C_L/C_D) for the range of AoAs studied in the present work. The C_L/C_D ratio along the GF length (red asterisks) vs. the clean airfoil (solid blue line) is represented.

From 4° to 7° a different trend is observed in the evolution of the influence with the GF lengths studied. A GF length of 0.25% *c* presents the best C_L/C_D ratio, with a slightly improvement compared with the clean airfoil. However, from 5° to 7°, the C_L/C_D difference obtained with respect to the clean airfoil at these AoAs varies only between 0.29 and 1.25. At these AoAs, GFs larger than 0.25% *c* do not contribute to enhance the aerodynamic performance of the airfoil.

At 8° of AoA, any of the GF lengths studied in the current work presents a better performance in the C_L/C_D ratio than the clean airfoil. At this AoA, as the GF length increases no improvement in the airfoil aerodynamic performance is found. Table 3 represents the best GF length for each AoA in terms of maximum lift-to-drag ratio: C_L/C_D max. Fourth column of Table 3 represents the C_L/C_D with no GF and the last column represents the variation with respect to the airfoil with no GF implemented: Δ C_L/C_D. The largest value of lift-to-drag C_L/C_D 115.68 is achieved at an AoA of 5° and corresponds to a GF length of 0.25% of the airfoil chord length *c*.

Table 3. Optimum GF length for each angle of attack studied and the increment in lift-to-drag ratio with respect to the case with no GF implementation.

AoA (°)	C_L/C_D Max.	GF Length (% *c*)	C_L/C_D no GF	$\Delta C_L/C_D$
−6	−36.86	3.00	−53.98	17.13
−5	−14.27	3.00	−39.95	25.68
−4	4.16	3.00	−24.04	28.19
−3	18.99	2.00	−7.15	26.14
−2	33.87	1.50	9.61	24.26
−1	46.93	1.00	26.00	20.93
0	61.75	1.00	41.95	19.80
1	78.91	0.75	57.50	21.41
2	94.25	0.50	72.68	21.57
3	104.52	0.50	87.54	16.98
4	114.48	0.25	102.13	12.36
5	115.68	0.25	114.44	1.25
6	114.41	0.25	113.81	0.60
7	110.10	0.25	109.81	0.29
8	102.55	0.00	102.73	0.00

For negative AoAs, the maximum increment in the C_L/C_D ratio is obtained with −4° of AoA with a peak value of 28.19. On the other hand, for positive AoAs, a GF length of 0.5% *c* achieves the largest difference in C_L/C_D ratio compared with the clean airfoil, with a value of 21.41 at 2° of AoA.

Figure 5 shows the streamwise velocity distribution around the GF for the lengths which provided the best cases in terms of C_L/C_D ratio. The presence of the GF changes the trailing edge flow pattern

and, therefore, modifies the effective camber of the airfoil resulting in a lift enhance. As the GF size increases, the presence of the two vortices behind the GF is more visible. The GF jets the flow in the boundary layer away from the airfoil surface and, thus, the circulation in the region behind the GF is enhanced.


(**a**) No GF

(**b**) GF 0.25% *c*

(**c**) GF 0.50% *c*

(**d**) GF 0.75% *c*

(**e**) GF 1% *c*
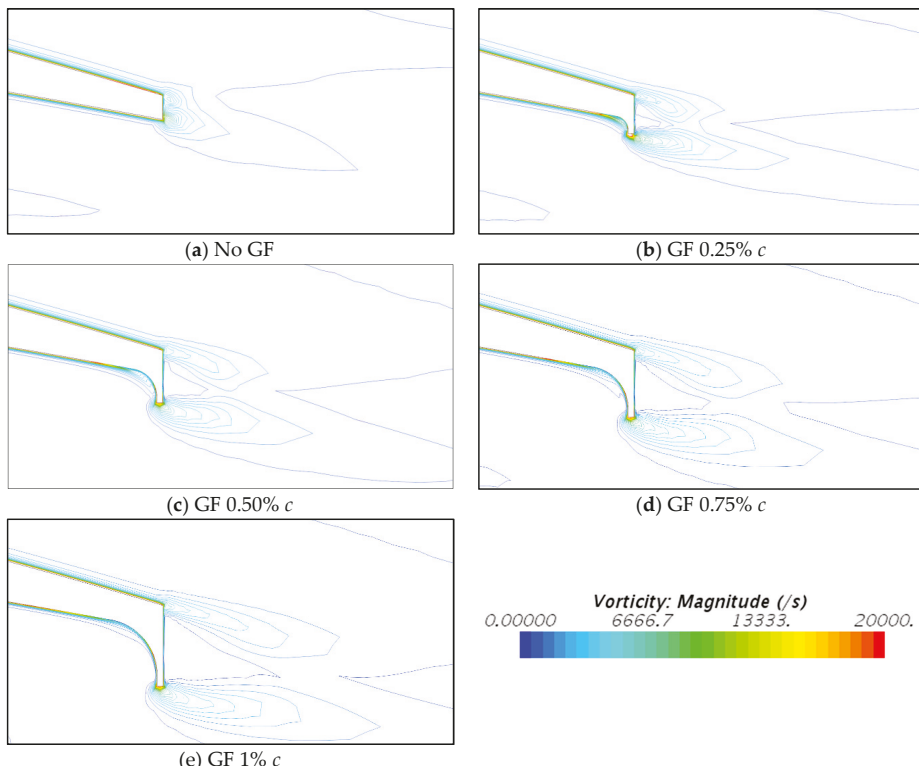
Figure 5. Streamwise vorticity fields for the case without GF and GF lengths of 0.25% *c*, 0.50% *c*, 0.75% *c* and 1% *c* at an angle of attack $\alpha = 0°$.

Figure 6 shows the pressure distributions on the surface of the clean airfoil DU91W(2)250 and the airfoil with GFs of 0.25% *c*, 0.50% *c*, 0.75% *c* and 1% *c* which have been considered that provide the best aerodynamic performance in terms to C_L/C_D ratio. The airfoil geometry, with a continuous black line, is illustrated as well. In the cases with the GF implemented, the aft loading of the airfoil increases and a positive gap with respect to the clean airfoil is visible at all AoAs.

ANN-Based Predicition Model

Artificial Neural Networks (ANNs) represent an exceptional tool in the modeling of different type of systems due to their several advantages and outstanding properties. One of them is related with the capability of learning, as they can learn complex non-linear black box models with an appropriate selection of the training algorithm and the input/output values. If neural networks are properly trained, i.e., the training patterns are carefully chosen, their response in new situations (new inputs) will be suitable with high probability, which means that will have the so-called generalization property. Lastly, as neural networks have an inherent parallel internal structure, their response after they have been trained is very fast, providing them real time capabilities to develop prediction models with large

datasets, see Lopez-Guede et al. [36]. All these properties make ANNs a method of major importance in a wide number of applications.
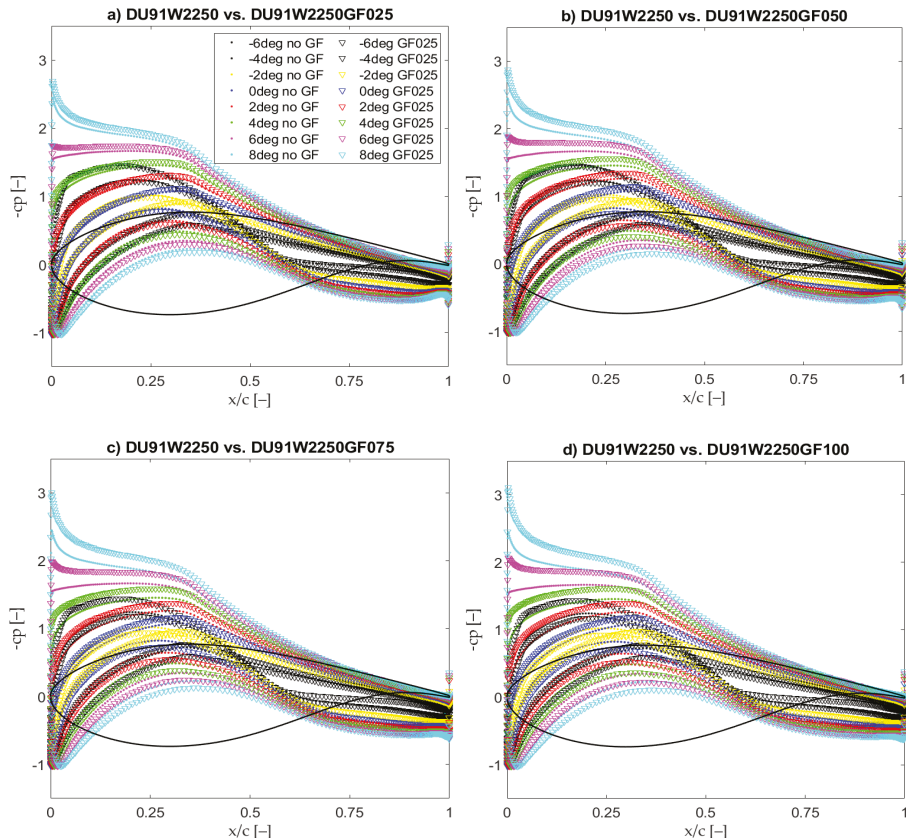

Figure 6. Pressure coefficient cp comparison between the clean airfoil DU91W2250 (no GF) and the best cases: (**a**) DU91W(2)250GF025; (**b**) DU91W(2)250GF050; (**c**) DU91W(2)250GF075; (**d**) DU91W(2) 250GF100.

Once studied the influence of different GF lengths and angles of attack in the airfoil aerodynamic performance by means of CFD techniques, a prediction model has been developed with an artificial neural network (ANN). The aim of this model is to predict the aerodynamic efficiency (C_L/C_D ratio) of the airfoil following the strategy based on the study by Lopez-Guede et al. [37]. In the current study, a multi-layer model with two hidden layers has been used. The C_L/C_D ratio is obtained by Equation (3), whereas the outputs of each hidden neuron follow a sigmoid function as defined in Equation (4). All these parameters represent a typical configuration of Multilayer Perceptron with Backpropagation (BP-MLP) neural networks. The postsinaptical h_i of each i neuron is calculated using a linear combination by means of Equation (5), where ω_i denotes the output layer weights and ω_{ij} the input (hidden) layer weights:

$$\frac{C_L}{C_D} = \sum_{i=1}^{i=Nhidden} \omega_i \cdot g_i\left(\vec{x}\right) + \theta \tag{3}$$

$$g_i(\vec{x}) = \frac{1}{1 + e^{-h_i}} \tag{4}$$

$$h_i(\vec{x}) = \sum_{j=1}^{j=Ninputs} \omega'_{i,j} \cdot x_j + \theta'_i \tag{5}$$

Matrices 6–9 contain the synaptic weights obtained by the neural network for the prediction of the C_L/C_D ratio:

$$Input\ hidden\ layer\ weights\ (\omega_{ij}) = \begin{bmatrix} -2.4229 & -0.9914 \\ 1.7982 & 0.2139 \end{bmatrix} \tag{6}$$

$$Output\ layer\ weights\ (\omega_i) = \begin{bmatrix} 1.2220 & 3.6533 \end{bmatrix} \tag{7}$$

$$Hidden\ layer\ threshold\ parameters\ (\sigma) = \begin{bmatrix} 1.4471 \\ 0.7852 \end{bmatrix} \tag{8}$$

$$Output\ layer\ threshold\ parameters\ (\sigma') = [-2.9805] \tag{9}$$

The ANN has two input neurons corresponding to the two real valued inputs (AoA and GF length) and one unique output neuron for the valued target (CL/CD ratio), as shown in Figure 7. The datasheet has been partitioned, i.e, 70% for training the ANN, 20% for validation and 10% for testing the quality of learned model.
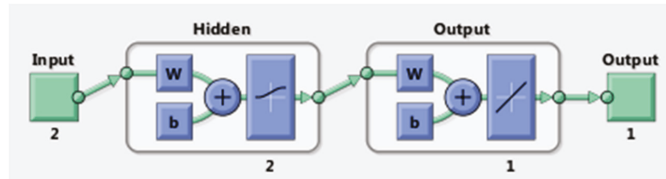
Figure 7. Diagram of the internal structure of the ANN designed.

Figure 8 shows the ANN results for all GF lengths and all AoAs studied in the present work. The colored surface illustrates the C_L/C_D values calculated by the proposed ANN and the CFD results are represented by black asterisks. The neural network predicts accurately the lift-to-drag ratios obtained by the numerical computations.
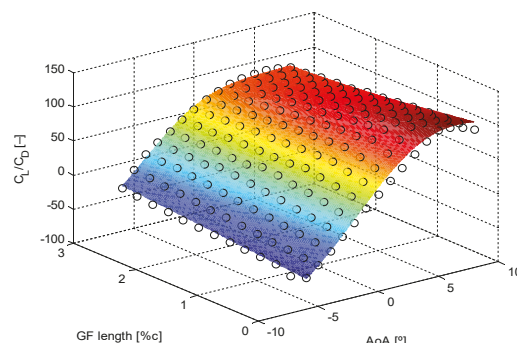
Figure 8. Neural network prediction surface of the CFD results of the airfoil aerodynamic performance C_L/C_D as a function of the GF length and the angle of attack (AoA). Black circles represent the CFD results.

The correlation coefficients (R-value) are shown in Figure 9. The regression line (highlighted in red) is drawn over expected C_L/C_D ratio and its neural prediction. The horizontal axis shows the expected C_L/C_D ratio and the vertical axis the C_L/C_D ratio prediction given by the neural network. The correlation coefficient value was determined as 0.99671 which indicates a good correlation between the results given by the ANN and the followed target. This result for the simulated GF lengths allows the algorithm to calculate and predict the C_L/C_D ratio for any GF length in the conditions studied of Reynolds number Re = 2×10^6.
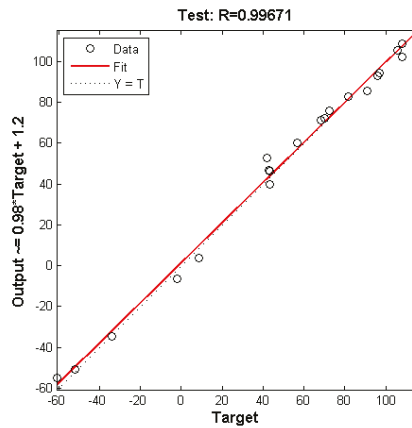

Figure 9. ANN training correlation coefficients.

4. Conclusions

The current work presents a parametric study to evaluate the influence of different GF lengths in the aerodynamic performance of a DU91W(2)250 airfoil. Two-dimensional CFD simulations have been carried out, using RANS equations at Reynolds number of Re = 2×10^6. Firstly, a clean airfoil without any flow control device implemented has been simulated and the results in terms of lift-to-drag ratio have been validated with experimental data. Then, simulations have been performed with GFs from 0.25% *c* to 3% *c* at angles of attack from $-6°$ to $8°$ to investigate the airfoil aerodynamic performance. The results showed that, for positive angles of attack, peak values are obtained with GF lengths between 0.25% *c* and 0.75% *c*. Specifically, an increase of 21.57 in C_L/C_D ratio has been obtained with a GF length of 0.5% *c* at $2°$ of AoA. The influence of GFs decreased at AoAs larger than $5°$, where only a GF length of 0.25% *c* provides a slight improvement in terms of C_L/C_D ratio enhancement.

Secondly, the streamwise velocity distribution around the GF has been addressed with those GF lengths that provided the best aerodynamic performance in terms of C_L/C_D ratio. As expected, two counter-rotating vortices are formed in the near wake behind the flow control device. As the GF length increases the size of the vortices increases, especially the one on the lower region. Moreover, the pressure distribution has been studied at all AoAs, resulting in a clearly visible increment in the cp due to the GF implementation for all the length cases.

The optimal GF length varies at different angles of attack, which means that a fixed GF length would not reach the optimal C_L/C_D ratio at all the AoAs. Therefore, this result suggests that a careful analysis of the GF length is needed to yield an efficient flow control system and to consider the study of GFs as active flow control devices. In that case, the GF length would change along the AoA to achieve the best C_L/C_D ratio depending on the working conditions.

To that end, an ANN has been developed and trained to predict the aerodynamic efficiency of the airfoil in terms of C_L/C_D ratio. This tool allows to obtain an accurate prediction model of the aerodynamic behavior of the airfoil, which can be a suitable method to optimize the GF lengths for

different wind and /or rotor blade airfoil geometry scenarios and its implications in the wind turbine control system.

References

1. Johnson, S.J.; van Dam, C.P.; Berg, D.E. *Active Load Control Techniques for Wind Turbines*; Sandia Report SAND 2008-4809; Sandia National Laboratories: Albuquerque, NM, USA; Livermore, CA, USA, 2008.

2. Taylor, H.D. *The Elimination of Diffuser Separation by Vortex Generators*; R-15064-5; United Aircraft Corporation: East Hartford, CT, USA, 1947.

3. Wood, R.M. A Discussion of Aerodynamic Control Effectors Concepts (ACEs) for Future Unmanned Air Vehicles (UAVs). In Proceedings of the AIAA 1st Technical Conference and Workshop on Unmanned Aerospace Vehicle, Systems, Technologies and Operations, Portsmouth, VA, USA, 20–23 May 2002.

4. Aramendia, I.; Fernandez-Gamiz, U.; Antonio Ramos-Hernanz, J.; Sancho, J.; Manuel Lopez-Guede, J.; Zulueta, E. Flow Control Devices for Wind Turbines. In *Energy Harvesting and Energy Efficiency: Technology, Methods, and Applications*; Springer: Cham, Switzerland, 2017; Volume 37, pp. 629–655. [CrossRef]

5. Fernandez-Gamiz, U.; Velte, C.M.; Rethore, P.; Sorensen, N.N.; Egusquiza, E. Testing of self-similarity and helical symmetry in vortex generator flow simulations. *Wind Energy* **2016**, *19*, 1043–1052. [CrossRef]

6. Fernandez-Gamiz, U.; Errasti, I.; Gutierrez-Amo, R.; Boyano, A.; Barambones, O. Computational Modelling of Rectangular Sub-Boundary Layer Vortex Generators. *Appl. Sci.* **2018**, *8*, 138. [CrossRef]

7. Holst, D.; Bach, A.B.; Nayeri, C.N.; Paschereit, C.O.; Pechlivanoglou, G. Wake Analysis of a Finite Width Gurney Flap. *J. Eng. Gas Turbines Power Trans. ASME* **2016**, *138*, 062602. [CrossRef]

8. Liebeck, R. Design of Subsonic Airfoils for High Lift. *J. Aircr.* **1978**, *15*, 547–561. [CrossRef]

9. Jeffrey, D.; Zhang, X.; Hurst, D. Aerodynamics of Gurney flaps on a single-element high-lift wing. *J. Aircr.* **2000**, *37*, 295–301. [CrossRef]

10. Wang, J.J.; Li, Y.C.; Choi, K. Gurney flap-lift enhancement, mechanisms and applications. *Prog. Aerosp. Sci.* **2008**, *44*, 22–47. [CrossRef]

11. Pastrikakis, V.A.; Steijl, R.; Barakos, G.N. Effect of active Gurney flaps on overall helicopter flight envelope. *Aeronaut. J.* **2016**, *120*, 1230–1261. [CrossRef]

12. Tang, D.; Dowell, E.H. Aerodynamic loading for an airfoil with an oscillating gurney flap. *J. Aircr.* **2007**, *44*, 1245–1257. [CrossRef]

13. Lee, T.; Su, Y.Y. Lift enhancement and flow structure of airfoil with joint trailing-edge flap and Gurney flap. *Exp. Fluids* **2011**, *50*, 1671–1684. [CrossRef]

14. Shukla, V.; Kaviti, A.K. Performance evaluation of profile modifications on straight-bladed vertical axis wind turbine by energy and Spalart Allmaras models. *Energy* **2017**, *126*, 766–795. [CrossRef]

15. Cole, J.A.; Vieira, B.A.O.; Coder, J.G.; Premi, A.; Maughmer, M.D. Experimental Investigation into the Effect of Gurney Flaps on Various Airfoils. *J. Aircr.* **2013**, *50*, 1287–1294. [CrossRef]

16. Fernandez-Gamiz, U.; Zulueta, E.; Boyano, A.; Ansoategui, I.; Uriarte, I. Five Megawatt Wind Turbine Power Output Improvements by Passive Flow Control Devices. *Energies* **2017**, *10*, 742. [CrossRef]

17. Astolfi, D.; Castellani, F.; Terzi, L. Wind Turbine Power Curve Upgrades. *Energies* **2018**, *11*, 1300. [CrossRef]

18. Terzi, L.; Lombardi, A.; Castellani, F.; Astolfi, D. Innovative methods for wind turbine power curve upgrade assessment. In Proceedings of the WindEurope Conference 2018, Hamburg, Germany, 25–28 September 2018.

19. Camocardi, M.E.; Maranon Di Leo, J.; Delnero, J.S.; Lerner, J.L.C. Experimental Study Of A Naca 4412 Airfoil With Movable Gurney Flap. In Proceedings of the 49th AIAA Aerospace Sciences Meeting including the New Horizons Forum and Aerospace Exposition, Orlando, FL, USA, 4–7 January 2011.

20. Han, D.; Dong, C.; Barakos, G.N. Performance improvement of variable speed rotors by Gurney flaps. *Aerosp. Sci. Technol.* **2018**, *81*, 118–127. [CrossRef]

21. Storms, B.L.; Jang, C.S. Lift Enhancement of an Airfoil using a Gurney Flap and Vortex Generators. *J. Aircr.* **1994**, *31*, 542–547. [CrossRef]

22. Mohammadi, M.; Doosttalab, A.; Doosttalab, M. The effect of various gurney flaps shapes on the performace of wind turbine airfoils. In Proceedings of the ASME Early Career Technical Conference, Atlanta, GA, USA, 2–3 November 2012.

23. Gebhardt, C.G.; Preidikman, S.; Massa, J.C. Numerical simulations of the aerodynamic behavior of large horizontal-axis wind turbines. *Int. J. Hydrogen Energy* **2010**, *35*, 6005–6011. [CrossRef]

24. Pastrikakis, V.; Woodgate, M.; Barakos, G. CFD Method for Modelling Gurney Flaps. In *Recent Progress in Flow Control for Practical Flows*; Doerffer, P., Barakos, G., Luczak, M., Eds.; Springer: Berlin, Germany, 2017; pp. 23–49.

25. Woodgate, M.A.; Pastrikakis, V.A.; Barakos, G.N. Rotor Computations with Active Gurney Flaps. *Adv. Fluid-Struct. Interact.* **2016**, *133*, 133–166. [CrossRef]

26. Fernandez-Gamiz, U.; Zulueta, E.; Boyano, A.; Ramos-Hernanz, J.A.; Manuel Lopez-Guede, J. Microtab Design and Implementation on a 5 MW Wind Turbine. *Appl. Sci.* **2017**, *7*, 536. [CrossRef]

27. Fernandez-Gamiz, U.; Gomez-Marmol, M.; Chacon-Rebollo, T. Computational Modeling of Gurney Flaps and Microtabs by POD Method. *Energies* **2018**, *11*, 2091. [CrossRef]

28. Timmer, W.; van Rooij, R. Summary of the Delft University wind turbine dedicated airfoils. *J. Sol. Energy Eng. Trans. ASME* **2003**, *125*, 488–496. [CrossRef]

29. Siemens STAR CCM+ Version 11.06.011. Available online: http://mdx.plm.automation.siemens.com/ (accessed on 10 June 2018).

30. Menter, F.R. 2-Equation Eddy-Viscosity Turbulence Models for Engineering Applications. *AIAA J.* **1994**, *32*, 1598–1605. [CrossRef]

31. Kral, L. Recent experience with different turbulence models applied to the calculation of flow over aircraft components. *Prog. Aerosp. Sci.* **1998**, *34*, 481–541. [CrossRef]

32. Gatski, T.B. *Turbulence Modeling for Aeronautical Flows*; von Karman Institute for Fluid DynamicsVKI Lecture Series: CFD-Based Aircraft Drag Prediction and Reduction; Von Karman Institute for Fluid Dynamics: Sint-Genesius-Rode, Belgium, 2003.

33. Mayda, E.A.; van Dam, C.P.; Nakafuji, D. Computational Investigation of Finite Width Microtabs for Aerodynamic Load Control. In Proceedings of the 43rd AIAA Aerospace Sciences Meeting and Exhibit, Reno, NV, USA, 10–13 January 2005.

34. Sorensen, N.N.; Mendez, B.; Munoz, A.; Sieros, G.; Jost, E.; Lutz, T.; Papadakis, G.; Voutsinas, S.; Barakos, G.N.; Colonia, S.; et al. CFD code comparison for 2D airfoil flows. *J. Phys. Conf. Ser.* **2016**, *753*, 082019. [CrossRef]

35. Vinokur, M. On One-Dimensional Stretching Functions for Finite-Difference Calculations. *J. Comput. Phys.* **1983**, *50*, 215–234. [CrossRef]

36. Lopez-Guede, J.M.; Ramos-Hernanz, J.A.; Zulueta, E.; Fernandez-Gamiz, U.; Oterino, F. Systematic modeling of photovoltaic modules based on artificial neural networks. *Int. J. Hydrogen Energy* **2016**, *41*, 12672–12687. [CrossRef]

37. Lopez-Guede, J.M.; Ramos-Hernanz, J.A.; Zulueta, E.; Fernandez-Gamiz, U.; Azkune, G. Dual model oriented modeling of monocrystalline PV modules based on artificial neuronal networks. *Int. J. Hydrogen Energy* **2017**, *42*, 18103–18120. [CrossRef]

Article

Investigation on Optimization Design of Offshore Wind Turbine Blades based on Particle Swarm Optimization

Yong Ma [1,2,3], Aiming Zhang [1], Lele Yang [1,3,*], Chao Hu [2] and Yue Bai [2]

[1]   School of Marine Engineering and Technology, Sun Yat-sen University, Guangzhou 518000, China;
      mayong3@mail.sysu.edu.cn (Y.M.); zhangaim5@mail2.sysu.edu.cn (A.Z.)
[2]   College of Shipbuilding Engineering, Harbin Engineering University, Harbin 150001, China;
      huchao@hrbeu.edu.cn (C.H.); mayong02@hrbeu.edu.cn (Y.B.)
[3]   Southern Marine Science and Engineering Guangdong Laboratory (Zhuhai), Zhuhai 519000, China
*   Correspondence: yanglele@mail.sysu.edu.cn; Tel.: +86-155-0126-3568

check for
updates

Abstract: Offshore wind power has become an important trend in global renewable energy development. Based on a particle swarm optimization (PSO) algorithm and FAST program, a time-domain coupled calculation model for a floating wind turbine is established, and a combined optimization design method for the wind turbine's blade is developed in this paper. The influence of waves on the power of the floating wind turbine is studied in this paper. The results show that, with the increase of wave height, the power fluctuation of the wind turbine increases and the average power of the wind turbine decreases. With the increase of wave period, the power oscillation amplitude of the wind turbine increases, and the power of the wind turbine at equilibrium position decreases. The optimal design of the offshore floating wind turbine blade under different wind speeds is carried out. The results show that the optimum effect of the blades is more obvious at low and mid-low wind speeds than at rated wind speeds. Considering the actual wind direction distribution in the sea area, the maximum power of the wind turbine can be increased by 3.8% after weighted optimization, and the chord length and the twist angle of the blade are reduced.

Keywords: wind turbine; PSO algorithm; FAST; time-domain coupled model; blade optimization

1. Introduction

Climate change is showing abnormal effects all over the world. Environmental pollution is continuously aggravated, and energy demand is increasingly variable. Developing and utilizing clean and pollution-free renewable energy has become an effective way to alleviate energy shortages, reduce environmental pollution and improve climate conditions [1].

Wind energy is one of the most mature forms of renewable energy, which has promising large-scale development conditions and commercial development prospects. Wind energy includes onshore wind energy and offshore wind energy. In recent years, the development and utilization of onshore wind energy has encountered bottlenecks due to the limitation of land and wind resources. Compared with onshore wind power, offshore wind power has many advantages, such as higher wind speed, more stable wind direction, and smaller turbulence and wind shear. With the rapid development of wind power technology, the leading direction of wind power development in the future will focus on offshore wind power [2].

A large number of studies on fixed wind turbines have been carried out. Apparent models suitable for the wind turbines have been developed to predict the aerodynamic characteristics of the wind turbine [3,4]. In the engineering application, most design software for the wind turbine follows the

dynamic stall model in the helicopter field, and modifies the working environment of the fixed wind turbine [5,6]. It can basically meet the design requirements of the fixed wind turbine. At present, fixed wind turbine technology has become relatively mature and accomplished commercialization in China and several European countries. However, the floating wind turbine can move freely in the ocean environment. It is always in an obvious oscillation dynamic state under the influence of waves. Continuous oscillation not only causes the dynamic response of the wind turbine, but also enhances the unsteady effect of aerodynamic load, which brings great difficulties to the design and evaluation of floating wind turbine. The technology is still in the primary stage of research and development [7].

The offshore floating wind turbine is a very complex system, which mainly consists of the top wind turbine generator set, the tower supporting the wind turbine, the floating platform infrastructure and the mooring positioning system. For the wind turbine generator set alone, blades with excellent aerodynamic performance are the core of wind turbines [8]. Blade design is a complex multi-objective optimization design process, which needs to meet a number of design indicators, such as aerodynamic performance, structural strength and economic characteristics [9]. There are three theoretical research methods: blade element momentum (BEM) method based on momentum conservation; generalized dynamics wake (GDW) based on vortex theory; CFD method by solving N-S equation directly. The BEM method can simply calculate the energy efficiency and the force of horizontal axis impeller. It is effective and fast for estimating the overall load of the impeller. It is suitable for wind turbines with equal blade lengths and no less than a 3 blade tip speed ratio. The BEM method is the most widely used and technologically mature aerodynamic performance prediction method for the wind turbine [10,11]. GDW method includes the dynamic wake effect, tip loss and skewed wake effect, and does not require additional modified model [12]. However, the method assumes that the induced velocity is small relative to the inflow velocity. Thus, it is suitable for the wind turbines with heavy load. When the wind speed is small, the wake appears to be in a turbulent state, and the method becomes unstable [13]. CFD method can simulate yaw, tower shadow, wind shear and other complex conditions. Through CFD calculation, abundant flow field information can be obtained [14,15]. However, due to the large dimension of the wind turbine and the complexity of blade shape, the CFD method requires a lot of computer resources and computing time. Besides, this method is affected by the turbulence model, transition model, discrete format, boundary conditions and other factors [16].

In the application research process of the wind turbine, numerous methods synthetically simulating wind turbine loads have been developed based on the above theoretical research methods. Some scholars have synthetically simulated the preliminary design of floating wind turbines by using the linear frequency domain method commonly used in offshore oil and gas exploitation. For example, Bulder et al. [17] used the linear frequency domain method to simulate a wind turbine with a three-dimensional floating body. The response amplitude operator and standard deviation of the six rigid-body motion modes of the floating platform were calculated and analyzed. Tracy [18] used a similar method to study the optimal design parameters of tension leg and mast-type wind turbine. However, these studies only introduce the aerodynamic and structural characteristics of the wind turbines by adding additional mass, additional damping and an additional recovery matrix, without simulating the real wind turbine. The linear frequency domain method can't simulate the non-linear dynamic characteristics and unsteady effects. Some scholars use other methods to study the floating wind turbine. For example, Henderson et al. [19] used a method called "state domain" to study the effect of platform motion on the fatigue load of the wind turbine. Combining aeroelastic load simulation software with hydrodynamic load simulation software, Withee [20] established the time domain dynamic model for floating wind turbine, and studied a tension leg wind turbine. Because they employed a simple hydrodynamic model, aerodynamic model or structural dynamic model, these studies still have some limitations and couldn't develop a better blade optimization design scheme.

Wind turbine blade design is also a complex multi-objective optimization design process. Strong interactions exist between the disciplines of aerodynamics, dynamics, structures, and economies. A number of previous studies have optimized blades with intelligent calculation methods, including

a neural network algorithm, genetic algorithm and data mining algorithm [21–23]. Particle swarm algorithm is a modern heuristic algorithm, which has great advantages in computing speed and memory consumption, and has fewer parameters to adjust. Liao et al. [24] employed an improved PSO algorithm to optimize wind turbine blades. The comparison results of optimized blades and reference blades indicated that this method was feasible and practical. Combined with the improved PSO algorithm with FAST program, they pursued the minimum blade mass to reduce the cost of the wind turbine. The thickness and the location of the layers in spar caps were selected as the optimization variables [25].
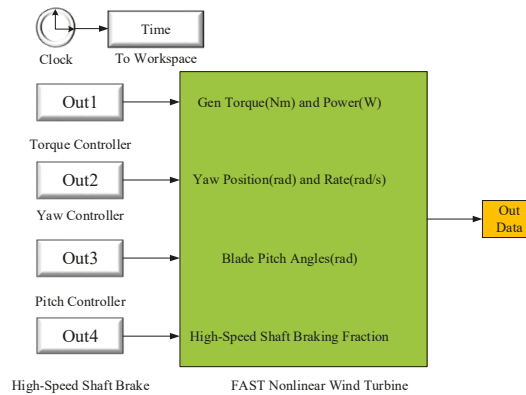
In addition, the wind speed of 12 m/s is mainly used as the design reference for international mainstream wind turbines. But the wind field with high-quality wind resources is limited. The wind field with low wind speed occupies a larger proportion, and these wind fields are generally closer to the power grid [26]. Taking China as an example, only the wind speed of 9.5 m/s in Fujian sea area is relatively close to the average wind speed in Europe, while the average wind speed in other sea areas is generally less than 8m/s, and even the wind speed in many sea areas is less than 7 m/s.

Therefore, this paper combines the PSO algorithm and FAST V8 computational analysis software for the wind turbine to optimize the design of offshore wind turbine blades in sea areas with different wind speeds including low wind speed. The "aero-hydro-control-structure" coupled time-domain calculation model for floating wind turbine is developed. By using this model, the motion state of floating wind turbine under real working conditions is simulated. Aiming at getting the maximum output power of the wind turbine, the optimal design of the wind turbine blade can be searched in many combinations by changing the distribution of twist angle and chord length. In addition, the influence of sea state and wind conditions in the actual sea area on the optimal design of the wind turbine blades is investigated. The study can provide theoretical guidance for the optimal design of an offshore floating wind turbine blade.

2. Blade Optimization Based on PSO Algorithm and FAST Program

FAST is an open source software for simulating dynamic response of horizontal-axis wind turbines, which is developed by the United States Department of Energy's NREL. FAST was originally used as a program to calculate the aerodynamic performance of horizontal axis wind turbines based on BEM theory. Thereafter, the hydrodynamic module, coupling calculation module, noise module, elastic module, ice load module, servo system module and wind environment load module were gradually added, making FAST a floating wind turbine solver with multiple performance modules. Input files should be provided before running the FAST, including the basic operation parameters of the wind turbine, blade geometry parameters, wind spectrum file, tower data file, wave load file, and platform foundation file. When FAST runs, each module reads its corresponding input file, and the data interaction between each module is completed by a dynamic link library. All modules cooperate to achieve time-domain coupled calculation.
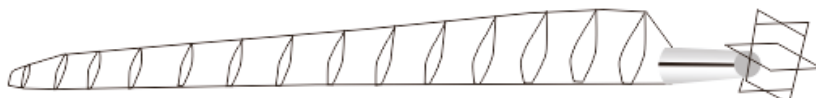
There are two different analysis modes in FAST V8. The first analysis mode is linearization, in which BEM is used to calculate the aerodynamic force; the second analysis mode is simulation, in which the time marching method is used to solve the nonlinear motion equation. This is also the method used in this study. In the simulation process, the aerodynamic response and the structural response of the wind turbine are processed in real time. FAST V8 provides the S-Function (System Function) function interface for the Simulink module library in MATLAB, as shown in Figure 1. The S-Function function is compiled by C++ language, and the optimization algorithm is embedded to carry out the optimization design of the wind turbine blades.

Figure 1. FAST Simulink S-function.

In this study, the NREL 5 MW wind turbine is used as the optimized parent form. The wind turbine is a three-blade horizontal axis wind turbine, which can be used as onshore or offshore wind turbine, and can be installed in deep-sea areas. It has gradually become a research example of large offshore wind turbines. The overall parameters of the wind turbine system are shown in the Table 1. PSO algorithm is used to optimize the design of the wind turbine blades. As shown in Figure 2, each blade of NREL 5 MW wind turbine has 19 control surfaces. After the airfoil of each control surface is selected, each control surface is determined by its twist angle and chord length. Figure 3 shows the blade layout. The control surfaces from the blade root to 4.1 m from the blade root are circular, and the overall shape is cylindrical. Therefore, the lift coefficient is 0, which makes no contribution to the aerodynamic performance of the whole blade. Therefore, only 16 control surfaces in the range of 4.1 m from the blade root to the blade tip need to be considered with a total of 16×2 parameters. Particle swarm space is set as 32 dimensions. For each particle, $y_1 \ldots y_{16}$ in $Y1 = (y_1 \ldots y_{32})$ represents the twist angle of 16 control surfaces of NREL 5 MW wind turbine blade in turn, and $y_{17} \ldots y_{32}$ represents the chord length of 16 control surfaces of a blade of NREL 5 MW wind turbine blade in turn.

Table 1. Overall parameters of NREL 5 MW wind turbine system.

| Name	Parameter
Unit-power	5 MW
Blade layout	Upwind Direction, 3 blades
Control system	Variable speed, variable pitch
Drive system	High-speed multi-stage gearbox
Blade and hub diameter	126 m, 3 m
Hub center height	90 m
Cut-in, rated and cut-out wind speed	3 m/s, 11.4 m/s, 25 m/s
Cut-in and rated blade rotate speed	6.9 rpm, 12.1 rpm
Rated tip speed	80 m/s
Cantilever length, axis inclination angle, pre-deflection angle of the blade	5 m, 5°, 2.5°
Total system mass	8,130,315.388 kg
Total gravity center height (below hydrostatic surface)	77.3829 m

**Figure 2.** Blade structure of NREL 5 MW wind turbine.
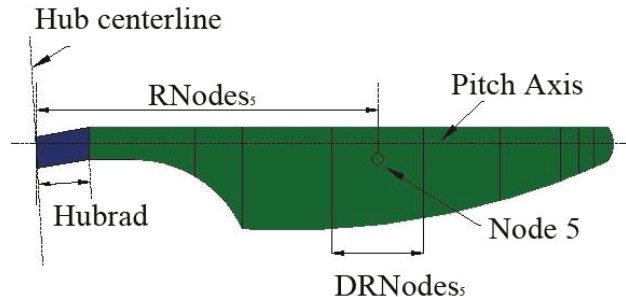
Figure 3. Blade layout.

After *K* iterations, the updating speed of the ith particle in the next iteration is as follows:

$$V_i = (v_1, v_2, \ldots v_d, \ldots v_D) \tag{1}$$

where

$$\begin{aligned} v_{id}^{k+1} = \omega v_{id}^{k+1} + C_1 r_1 \left(Pbest_{id}^k - x_{id}^k \right) \\ + C_2 r_2 \left(Zbest_{id} - x_{id}^k \right) \end{aligned} \tag{2}$$

In the next iteration, the position of the ith particle is:

$$X_i^{k+1} = X_i^{k+1} + V_i^{k+1} \tag{3}$$

where C_1 and C_2 are learning factors and non-negative constants, which can accelerate the convergence rate if appropriate selected; ω is inertia weight; r_1 and r_2 are random numbers distributed between [0,1].

In order to prevent premature convergence, which leads to local optimal solution of the algorithm, an improved PSO algorithm is adopted. After *K* iterations of the ith particle, the velocity update equation is changed to:

$$V_{id}(t+1) = \omega(t)V_{id}(t) + c_1(t)r_1(t)(P_{f_id}(t) - X_{id}(t)) \tag{4}$$

Improved PSO algorithm can enable particles to learn from excellent particles in the crowd and enhance particle search ability. The aerodynamic profile of offshore wind turbine blades is determined by the optimization results of PSO algorithm. Under the combined action of wind and waves, the floating wind turbine power is in a fluctuating state. The wind turbine power at balance position in a period of time is taken as the average power during this period. The optimization objective is to select the wind turbine blade with the maximum power at balance position. The fitness of each particle of the particle swarm is selected as the wind turbine power at balance position generated by FAST. By changing the distribution of twist angle and chord length of the blade and studying the change rule of aerodynamic performance of the wind turbine, the optimal design of the wind turbine blade can be determined.

When the program runs, the whole particle swarm is initialized to generate the initial population. The PSO algorithm needs to set an upper bound (ub) and a lower bound (pb) to prevent the particles from deviating from the solution range in the search process. At the same time, the algorithm can reduce the impact of the optimization results on the blade structure, strength and control system. In this study, the upper and lower bounds of particle swarm are ±10% of the original parameters of NREL 5 MW wind turbine blade. When the twist angle and chord length of any one-dimensional interface of a particle in particle swarm exceed the limit, the program sets the exceeding values as ub and pb. After the program starts to run, FAST is automatically called to calculate the fitness of each particle in the iteration process. When the set number of iterations is reached or the relative

error between the average fitness of particle swarm and the fitness of particle swarm is less than 0.5%, the program automatically terminates.

3. Validation of Particle Swarm Optimization

The improved PSO algorithm employed in this study has been verified and applied in the work of Liao et al. [24]. They compared the optimized results of improved PSO algorithm with those of Glauert method that was a traditional design method for the wind turbine blade. The comparison results showed that the shape parameters of the wind turbine blade obtained by improved PSO algorithm were more reasonable, which could meet the design requirement. The blade designed by improved PSO algorithm also had better performance than the blade designed by the Glauert method. In this study, in order to verify the feasibility of the blade optimization design method combining PSO algorithm with FAST program, the twist angle, chord length and power improvement of the wind turbine blades before and after optimization are analyzed by taking the NREL 5 MW wind turbine as the optimized parent form. During validity verification, the 5 MW wind turbine is considered as an offshore fixed wind turbine, and the foundation is anchored to the sea floor. The optimization of the wind turbine is carried out under steady wind. Therefore, in the main input file of FAST, CompMooring and CompHydro are both equal to 0. The six degrees of freedom of the platform in the ElastoDyn module is set to 0. The particle swarm size is 30. The number of iteration steps is set to 30. The time step is 0.0125 s, and the calculation time is 1000 s.

3.1. Optimization of Fixed Wind Turbine Blade at Rated Wind Speed

Comparing the twist angle and chord length of the optimized particle with that before optimization, as shown in Figures 4 and 5, the chord length of the optimized blade is slightly larger than that of the optimized blade after 10 m from the hub surface, and the twist angle is almost the same before and after optimization. From the graph, it can be seen that the distribution of the twist angle and chord length of the blade will jump after optimization by particle swarm optimization. This is because particle swarm optimization is only a theoretical calculation. In the calculation, the optimal twist angle and chord length of each control surface are considered only in theory, and the continuity of blade structure is not considered in the actual manufacturing process. Therefore, in the following blade optimization process, if there is a large jump in the distribution of twist angle and chord length, polynomial fitting is used to smooth the blade.
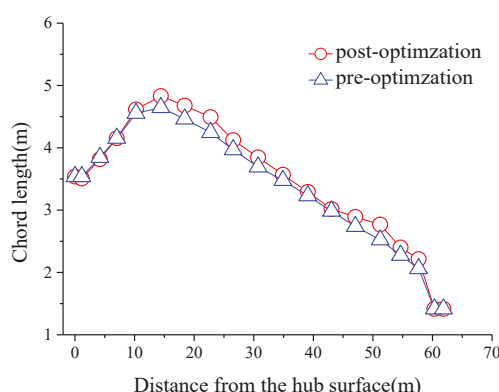

Figure 4. Distribution of the chord length for fixed wind turbine blade at rated wind speed before and after optimization.

The optimized power is 5037.3 kW, which is approximately equal to 5030 KW of the wind turbine before optimization, and the improved power is 0.145%. Under rated wind speed condition,

the optimization effect of the wind turbine blade is not great. This is because the NREL 5 MW wind turbine is designed according to the rated wind speed of 11.4 m/s, and the twist angle and chord length of each control surface have been designed according to the optimal size.
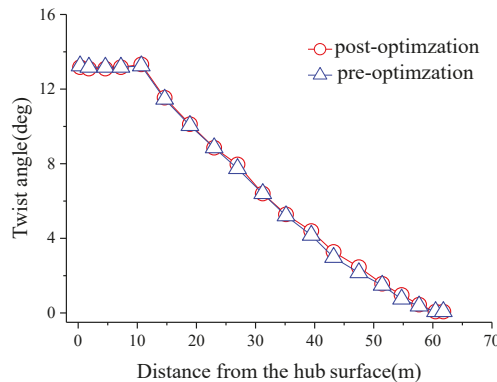

Figure 5. Distribution of the twist angle for fixed wind turbine blade at rated wind speed before and after optimization.

3.2. Optimization of Fixed Wind Turbine Blade at Low Wind Speed

In order to verify the PSO algorithm, the typical operating conditions of China's offshore waters with a wind speed of 6 m/s are selected. The time step is set to 0.0125 s and the time domain calculation period is 300 s. The time domain calculation result of NREL 5 MW wind turbine power is shown in Figure 6.
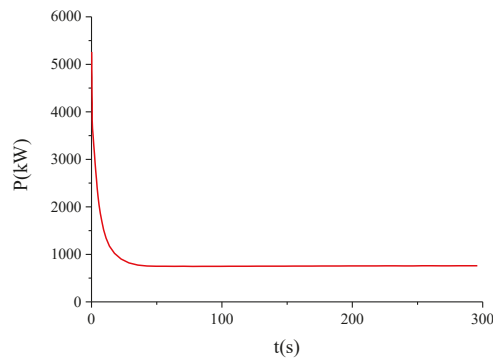

Figure 6. Time-domain calculation of fixed wind turbine power.

Figures 7 and 8 depict the distributions of the chord length and twist angle before and after optimization. After iterative screening of the PSO algorithm designed in this paper, the distribution of the chord length in the range of 10 m to 35 m from the hub surface of the wind turbine is less than that before optimization. The chord length of the control surface at 34.85 m is basically the same as that before optimization. The chord length in the range of 34.85 m from the hub surface to blade tip decreases further. The distribution of the twist angle in the range of 10.25 m to 38.95 m from the hub surface of the wind turbine is less than that before optimization. After 38.95 m, the distribution of twist angle after optimization is close to that before optimization.
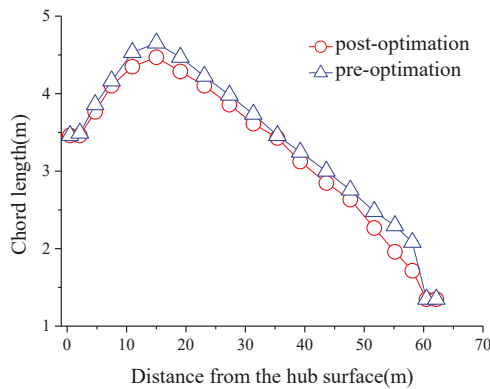
Figure 7. Distribution of the twist angle for fixed wind turbine blade at low wind speed before and after optimization.
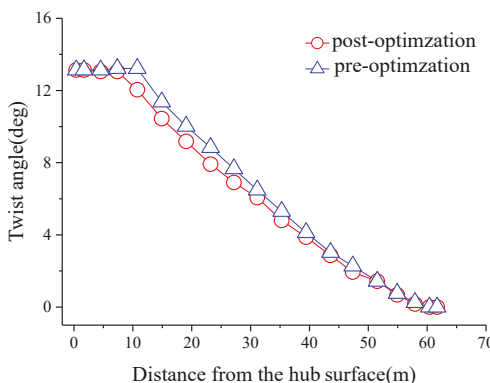

Figure 8. Distribution of the twist angle for fixed wind turbine blade at low wind speed before and after optimization.

The optimized wind turbine power is 760 kW, larger than 750 kW before optimization, and the power is increased by 1.4%. The enhancement effect is obviously larger than that at rated wind speed. In addition, when the wind turbine works, the wind turbine adjusts its position by yaw to adapt to the incoming wind. The phase angle between the impeller and the wind turbine blade changes periodically. Thus, the aerodynamic characteristics of the wind turbine blade need to have roughness. As can be seen in Figure 9, the optimized wind turbine power has been promoted obviously in the range of 5.5 m/s to 6.5 m/s of low wind speed. This indicates that the optimized wind turbine blades meet the roughness requirements of aerodynamic characteristics. Therefore, the blade optimization program based on PSO algorithm and FAST secondary development has an obvious effect on blade optimization at low wind speed. The sensitivity to wind speed is reduced, and the twist angle and chord length are also reduced. The ability of PSO algorithm to solve non-linear and global optimization problems is verified. It also proves the effectiveness of PSO algorithm in aerodynamic optimization of the wind turbine blades.
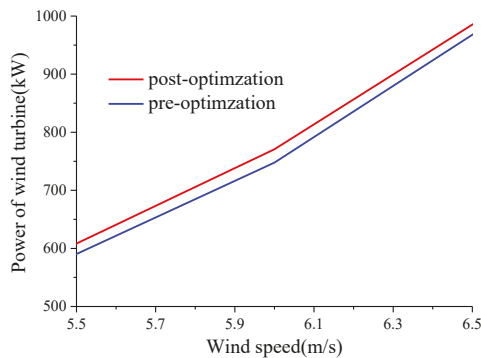
Figure 9. Wind turbine blade power at low wind speed before and after optimization.

4. Optimization of Offshore Wind Turbine Blades

The waves cause the motion of the foundation platform of floating wind turbines, which result in change of relative wind speed of the wind turbine. Accordingly, the aerodynamic performance of the wind turbine also changes, which is the main difference between floating wind turbine and fixed wind turbine. Therefore, for floating wind turbines installed in different sea areas, the influence of sea conditions should be taken into account in the design of the wind turbine blade. It has significant theoretical and practical meaning to develop optimization design method for the wind turbine blade that is suitable for different sea conditions.

In this paper, the optimization design of NREL 5 MW_OC3Hywind wind turbine blade is carried out by using the sea state parameters listed in Table 2. The incident wave is regular wave parallel to the hub axis.

Table 2. Sea state parameters.

Working Conditions	Wind Speed (m/s)	Significant Wave Height (m)	Peak Period (s)	Wave Direction (deg)
rated wind speed	11.4	6	12	0
mid-low wind speed	10	6	12	0
low wind speed	6	3	6	0

4.1. Influence of Regular Wave Height and Period on Wind Turbine Power

In order to study the effects of wave height and period of different regular waves on floating wind turbines, several typical wave heights and periods are selected respectively. The coupling model of 5 MW wind turbine-SPAR platform-mooring system is developed by FAST to calculate for different conditions. The wind turbine powers at wave crest, wave trough and equilibrium position are selected for analysis.

4.1.1. Effect of Wave Height on Wind Turbine Power

Figure 10 shows the change of the wind turbine power with a significant wave height, with the direction and period of the wave remaining unchanged. As the significant wave height increases from 2 m to 6 m, the wave peak power fluctuates greatly. The wave peak power shows a parabolic distribution in the range of 3 m to 4 m for significant wave height, increasing from 5460 kW to 5610 kW. The wave trough power increases slowly at first and then decreases sharply, from 3980 kW to 3770 kW. The wave peak power and wave trough power of the wind turbine fluctuate irregularly with wave height. This is due to that the floating foundation is fixed on the sea floor through anchor chains. When the floating platform is affected by wave force, the wind force is applied above the wind turbine.

The coupling effect of the two forces makes the phase angle between the wind turbine and the incoming wind change due to the platform shaking. The phase angle change is different for different wave height. Thus, the wind turbine power fluctuates irregularly. The power at the equilibrium position decreases rapidly in the range of 2 m to 5 m for significant wave height, from 5010 kW to 4790 kW. In the range of 5 m to 6 m, the power at the equilibrium position is stable at 4790 kW. The overall power fluctuation at the equilibrium position is only 4%, which is very small. This is because the Spar water line surface is very small and the draft depth is large, and thus the change of wave height has little influence on the dynamic response of the floating platform. Fixed onshore 5 MW wind turbine has a power of 5000 kW at 12 m/s wind speed. Floating wind turbine has a lower power at the equilibrium position. In conclusion, with the increase of incident wave height, the power fluctuation of the wind turbine increases, and the average power of the wind turbine decreases.
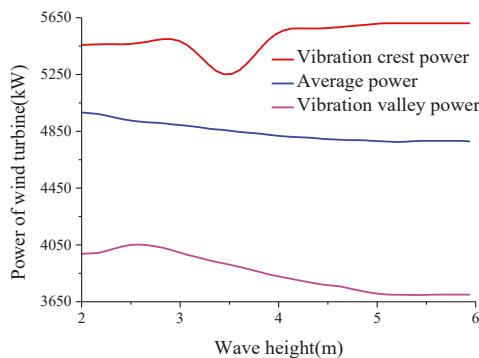

Figure 10. Comparison of the wind turbine power at different wave heights.

4.1.2. Effect of the Wave Period on the Wind Turbine Power

Figure 11 shows the change of the wind turbine power with the wave period, with the direction and significant wave height of the wave remaining unchanged. As the wave period increases from 1 s to 12 s, the wave peak power increases from 5410 kW to 5610 kW. The wave trough power decreases from 4680 kW to 3710 kW. The amplitude of power fluctuation increases gradually. When the incident wave period is 1 s, the wind turbine power at the equilibrium position is 4969 kW, which is the same as the power of 5 MW wind turbine on land at the same wind speed. It means that the influence of waves on the wind turbine power is small. But when the incident wave period is 12 s, the wind turbine power at the equilibrium position is only 4790 kW. The influence of waves on the wind turbine power becomes large. With the increase of the incident wave period, the wind turbine power at the equilibrium position decreases. NREL 5 MW wind turbine is a variable-speed and variable-pitch wind turbine. The control system can make the speed and pitch angle of the wind turbine correspond to the actual working conditions as much as possible. However, the large wave period results in a poor adaptive ability of the wind turbine. Then, the wind turbine cannot adjust its attitude to adapt to the incoming wind in time, resulting in a power reduction. In conclusion, the period of the wave is closely related to the wind turbine power. With the increase of incident wave period, the power oscillation amplitude of the wind turbine increases and wind turbine power at the equilibrium position decreases.
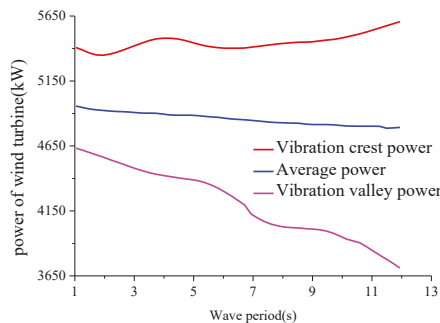
Figure 11. Comparison of the wind turbine power at different wave periods.

4.2. Optimization of the Wind Turbine Blade at Rated Wind Speed

At the rated wind speed, the PSO algorithm is used to optimize the floating wind turbine blades. The fitness output of the optimal particle for each iteration of PSO is shown in Figure 12. The evolution of the population can be observed. In 0-14 iterations, the particle swarm grows rapidly, and Zbest of the optimal particle increases from 4718 kW to 4761 kW. In 14–25 iterations, the growth rate of Zbest slows down, increasing from 4761 kW to 4766 kW. After 25 iterations, the optimal particle of particle swarm does not renew. The PSO algorithm stops automatically after 35 iterations, indicating that the difference between the average fitness and the best fitness of the population is less than 0.5%. The particle swarm as a whole approaches the optimal solution in the search area. Compared with the power before optimization, the power is increased by 1.017% after optimization by the PSO algorithm under this condition.
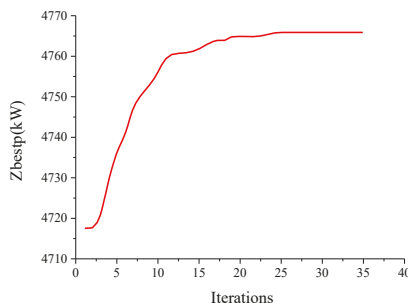

Figure 12. Evolution of particle swarm at rated wind speed.

The distributions of twist angle and chord length after optimization by the PSO algorithm are compared with those before optimization, as shown in Figures 13 and 14. The optimized twist angle is slightly larger than that before optimization in the range of 10.25 m to 47.15 m from hub surface. The optimized twist angle is almost close to that before optimization in the range of 47.15 m from the hub surface to the blade tip. The current optimization design only considers the best twist angle and chord length of each control surfaces by using blade element momentum, without considering the continuous process and actual operation of the wind turbine. Thus, some changes have taken place in the distribution of the chord length. The changes of the distribution of twist angle are more obvious. The chord length is smoothed by a spline curve in MATLAB. The distribution of chord length after smoothing by the spline curve is more reasonable, as shown in Figure 15. The continuity of blade structure is ensured by modification, which facilitates the manufacture of actual blades. The wind turbine power with smooth blades is 4751 kW, slightly less than that before smoothing. Compared with the power before optimization, the wind turbine power after smoothing is increased by 0.7%.
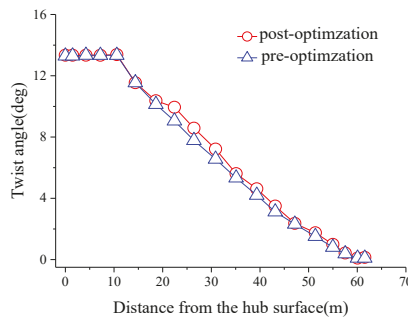
Figure 13. Distribution of the twist angle at rated wind speed before and after optimization.
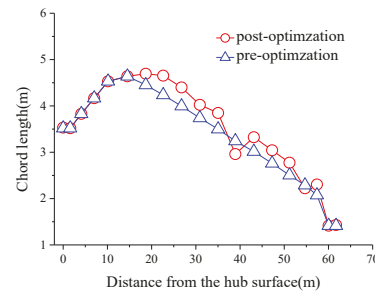
Figure 14. Distribution of the chord length at rated wind speed before and after optimization.
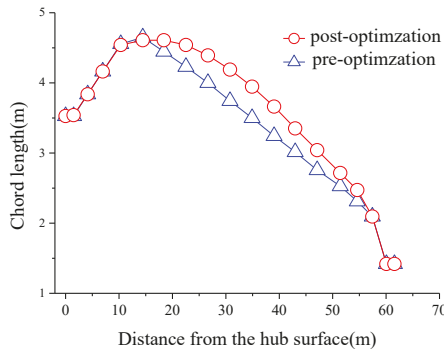
Figure 15. Distribution of the chord length at rated wind speed before and after smoothing.

4.3. Optimization of the Wind Turbine Blade at Mid-Low Wind Speed

At mid-low wind speeds, the fitness output of the optimal particle for each iteration of PSO can be observed in Figure 16. In 0~34 iterations, each iteration produces a better individual (Zbest). After 34 iterations, each iteration does not produce a better individual, but the particle swarm as a whole approaches the optimal solution in the search area. The PSO algorithm stops automatically after 50 iterations, indicating that the difference between the average fitness and the best fitness of the population is less than 0.5%.
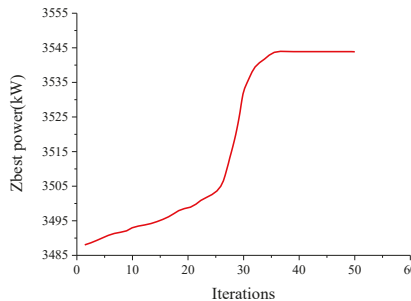
Figure 16. Evolution of particle swarm at mid-low wind speed.

Figures 17 and 18 are the distributions of twist angle and chord length after optimization at mid-low wind speed. The change of the twist angle and chord length in 15 control surfaces of floating wind turbine blades can be observed. In the range of 0 m to 10 m from the hub surface, the first four control surfaces are cylindrical, which are the connecting parts between blades and hub. Thus, there is no change in the twist angle and chord length. In the range of 10 m to 60 m from the hub surface, the distribution of twist angle after optimization is slightly larger than that before optimization, and the chord length is slightly larger than that before optimization. Except for the cylindrical control surface, the chord length in each control surface of the wind turbine after optimization is smaller than that before optimization. Therefore, the area of the wind turbine blade is reduced, and the material of the wind turbine blade is saved, which can save the cost. At mid-low wind speed, the power of the wind turbine at equilibrium position is 3485 kW before optimization. After optimization, the power of the wind turbine at equilibrium position is increased by 1.7%, namely 3544 kW.
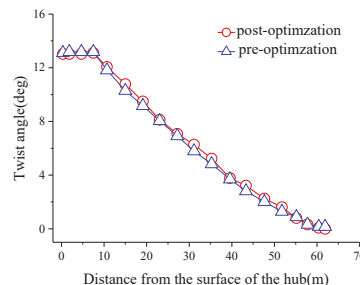

Figure 17. Distribution of the twist angle at mid-low wind speed before and after optimization.
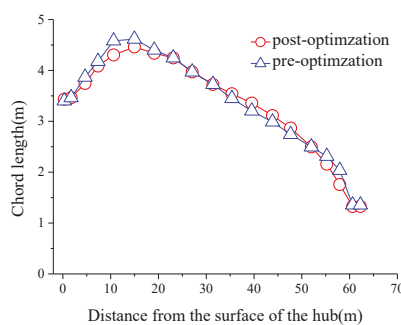
**Figure 18.** Distribution of the chord length at mid-low wind speed before and after optimization.

4.4. Optimization of the Wind Turbine Blade at Low Wind Speed

Population evolution can be observed from Figure 19. In 0~11 iterations, the particle swarm grows rapidly, and the Zbest of population particles increases from 777 kW to 797 kW. After 11 iterations, the optimal particle is no longer updated and no new extremum emerges. When the algorithm runs to 26 iterations, the particle swarm algorithm achieves the termination condition. The particle swarm as a whole approaches the optimal solution in the search area. The power of the wind turbine is increased by 2.5% through the optimization of particle swarm optimization. Figures 20 and 21 are the distributions of twist angle and chord length after optimization. The optimized twist angle and chord length are less than those before optimization in the range of 6.83 m from the hub surface to blade tip. The difference of twist angle and chord length before and after optimization is the greatest in the control surface 6.83 m from the hub surface. Along the direction of blade tip, the twist angle and chord length are gradually close to those before and after optimization. In summary, when the blade is optimized at low wind speed, the power of the wind turbine get promoted, while the manufacturing difficulty and cost of the blades are reduced.
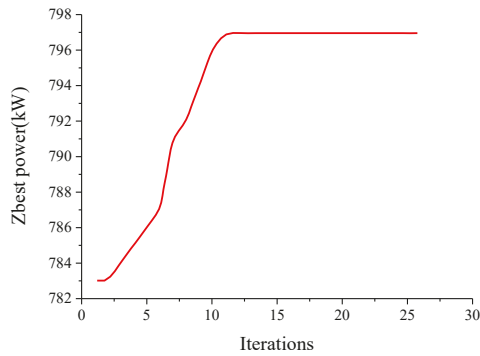
**Figure 19.** Evolution of particle swarm at low wind speed.
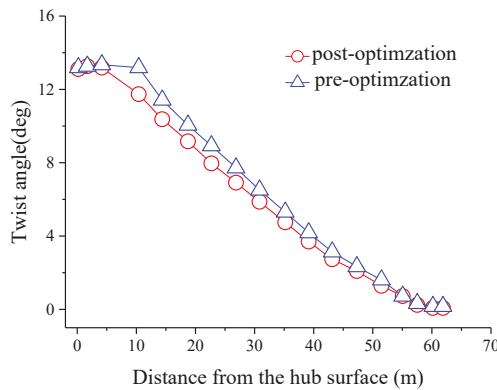
**Figure 20.** Distribution of the twist angle at low wind speed before and after optimization.
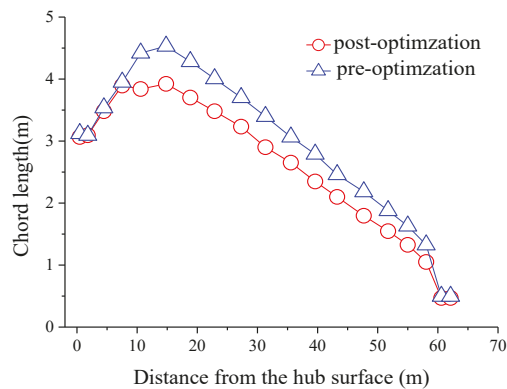
Figure 21. Distribution of the chord length at low wind speed before and after optimization.

4.5. Optimization of the wind turbine Blade under Actual Sea Conditions

The marine meteorological environment of site section should be considered in the offshore wind turbine design. In this paper, the location of the wind turbines is assumed to be in the China's Bohai Bay. According to the statistics of wind wave characteristics in Bohai Bay within one year, the average wind speed is 7 m/s, and the average significant wave height is 1.3 m. The wave period is 3.25 s. The frequency of the wind wave direction is 27% in the north direction, 22% in the northwest direction, and 8.3% in the northeast to northwest direction.

In the optimization process, the generated power of the wind turbines in eight wind wave directions (N, NW, W, SW, S, SE, E, NE) is calculated by FAST software. The particle fitness of the particle population is determined by the weighted average of the wind wave direction frequency. The expression is as follows:

$$\begin{aligned} \textit{Fitness} = \quad & (P(\text{N}) \times 0.27) + (P(\text{NW}) \times 0.23) \\ & + (P(\text{W}) \times 0.083 + (P(\text{SW}) \times 0.083) \\ & + (P(\text{S}) \times 0.083) + (P(\text{SE}) \times 0.083) \\ & + (P(\text{E}) \times 0.083) + (P(\text{NE}) \times 0.083) \end{aligned} \tag{5}$$

The wave spectrum is chosen as Jonswap spectrum. Under the rated wind speed, the floating wind turbine blade is optimized by PSO algorithm. As shown in Figure 22, particle swarm grows rapidly in 0~13 iterations, and the Zbest of particle swarm increases from 1180 kW to 1225 kW. After 13 iterations, the optimal particle of particle swarm does not renew. When it reaches 24 iterations, particle swarm stops automatically, indicating that the difference between the average fitness and optimal fitness of the population is less than 0.5%. The algorithm achieves the termination condition, and the particle swarm as a whole approaches the optimal solution in the search area. Under this condition, the power of the wind turbine is increased by 3.8% through the optimization of particle swarm optimization.

As shown in Figures 23 and 24, the optimized torsion angle is slightly less than that before optimization in the range of 10.25 m to 47.15 m from the hub surface. The optimized torsion angle is almost close to that before optimization in the range of 47.15 m to 60 m from the hub surface. The chord length in each control surface of optimized blade is less than that before optimization. The overall optimization effect is obvious.
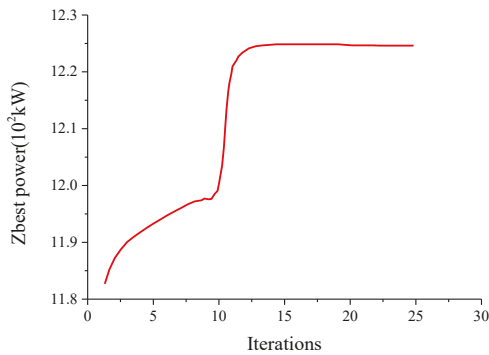
Figure 22. Evolution of the particle swarm under actual sea conditions.
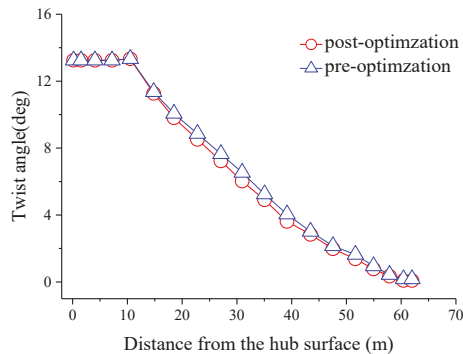
Figure 23. Distribution of the twist angle under actual sea conditions before and after optimization.
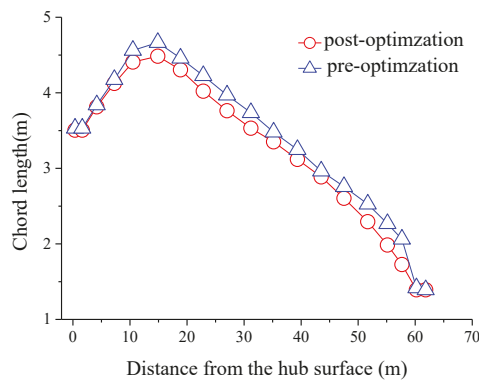
Figure 24. Distribution of the chord length under actual sea conditions before and after optimization.

5. Conclusions

Based on PSO algorithm and Fast program, a combined optimization design method for a wind turbine blade is developed in this paper. The optimization results of the NREL 5 MW fixed wind turbine show that this optimization method can not only improve the power of the wind turbine, but also reduce the manufacturing cost of the wind turbine blade. The feasibility of PSO is verified. The influence of wave on the power of floating wind turbine is studied in this paper. The results

show that, with the increase of wave height, the power fluctuation of the wind turbine increases and the average power of the wind turbine decreases. With the increase of the wave period, the power oscillation amplitude of the wind turbine increases, and the power of the wind turbine at equilibrium position decreases. The optimal design of the offshore floating wind turbine blade under different wind speeds is carried out. The results show that the power of the optimized wind turbine blade increases less under rated wind speeds, and the optimization effect of the blade is more obvious at mid-low and low wind speeds. The Bohai Strait is chosen as the operation site of the wind turbine, and the wind wave direction is weighted. After optimization, the maximum power of the wind turbine can be increased by 3.8% after weighted optimization, and the chord length and the twist angle of the blade are reduced. The results of this study can provide theoretical guidance for the optimal design of a offshore floating wind turbine blade.

Author Contributions: Conceptualization, L.Y. and Y.M.; Methodology, L.Y.; Software, L.Y. and A.Z.; Validation, L.Y. and Y.M.; Investigation, L.Y.; Resources, Y.M.; Data Curation, C.H.; Writing-Original Draft Preparation, L.Y.; Writing-Review & Editing, A.Z. and Y.B.; Visualization, A.Z.; Supervision, C.H.; Project Administration, Y.M.; Funding Acquisition, Y.M.

Conflicts of Interest: The authors declare no conflict of interest.

References

1. Oh, K.-Y.; Nam, W.; Ryu, M.S.; Kim, J.Y.; Epureanu, B.I. A review of foundations of offshore wind energy convertors: Current status and future perspectives. *Renew. Sustain. Energy Rev.* **2018**, *88*, 16–36. [CrossRef]
2. Fontana, C.M.; Hallowell, S.T.; Arwade, S.R.; DeGroot, D.J.; Melissa, E.L.; Charles, P.A.; Brian, D.; Andrew, T.M.; Senol, O. Multiline anchor force dynamics in floating offshore wind turbines. *Wind Energy* **2018**, *21*, 1177–1190. [CrossRef]
3. Madsen, H.A.; Rasmussen, F. A near wake model for trailing vorticity compared with the blade element momentum theory. *Wind Energy* **2010**, *7*, 325–341. [CrossRef]
4. Leishman, J.G. Challenges in modelling the unsteady aerodynamics of wind turbines. *Wind Energy* **2002**, *5*, 85–132. [CrossRef]
5. Butterfield, C.P.; Simms, D.; Scott, G.; Hansen, A.C. Dynamic stall on wind turbine blades. In Proceeding of the Wind power '91Conerence and Exposition, Palm Springs, CA, USA, 24–27 September 1991; pp. 393–401.
6. Pierce, K.G. Wind Turbine Load Prediction Using the Beddoes-Leishman Model for Unsteady Aerodynamics and Dynamic Stall. Master's Thesis, University of Utah, Salt Lake, UT, USA, 1996.
7. Liang, L.; Yuanchuan, L.; Zhiming, Y.; Gao, Y. Wind field effect on the power generation and aerodynamic performance of offshore floating wind turbines. *Energy* **2018**, *157*, 379–390.
8. Li, X.; Yang, K.; Liao, C.; Bai, J.; Zhang, L.; Xu, J. Overall design optimization of dedicated outboard airfoils for horizontal axis wind turbine blades. *Wind Energy* **2018**, *21*, 320–337. [CrossRef]
9. Chehouri, A.; Younes, R.; Ilinca, A.; Perron, J. Review of performance optimization techniques applied to wind turbines. *Appl. Energy.* **2015**, *142*, 361–388. [CrossRef]
10. Pratumnophart, P.; Leung, P.S. Validation of various windmill brake state models used by blade element momentum calculation. *Renew. Energy.* **2011**, *36*, 3222–3227. [CrossRef]
11. Bai, C.J.; Wang, W.C.; Chen, P.W.; Chong, W.T. System integration of the horizontal-axis wind turbine: The design of turbine blades with an axial-flux permanent magnet generator. *Energies* **2014**, *7*, 7773–7793. [CrossRef]
12. Gaonkar, G.H.; Peters, D. Review of dynamic inflow modeling for rotorcraft flight dynamics. *Vertica* **1988**, *12*, 213–242. [CrossRef]

13. Laino, D.; Hansen, A.C. Current efforts toward improved aerodynamic modeling using the AeroDyn subroutines ASME wind energy symposium. In Proceeding of the Aerospace Sciences Meeting and Exhibit, Reno, NV, USA, 5–8 January 2004; pp. 329–338.

14. Shahizare, B.; Nazri Bin Nik Ghazali, N.; Chong, W.; Saeed Tabatabaeikia, S.; Izadyar, N. Investigation of the optimal omni-direction-guide-vane design for vertical axis wind turbines based on unsteady flow CFD simulation. *Energies* **2016**, *9*, 146. [CrossRef]

15. Gebhardt, C.G.; Preidikman, S.; Massa, J.C. Numerical simulations of the aerodynamic behavior of large horizontal-axis wind turbines. *Int. J. Hydrogen Energy* **2010**, *35*, 6005–6011. [CrossRef]

16. Benjanirat, S. Computational studies of the horizontal axis wind turbines in high wind speed condition using advanced turbulence models. Ph.D. Thesis, Georgia Institute of Technology, Atlanta, GA, USA, 2006.

17. Bulder, B.H.; van Hees, M.T.; Henderson, A.; Huijsmans, R.H.M.; Pierik, J.T.G.; Snijders, E.J.B.; Wijnants, G.H.; Wolf, M.J. *Study to Feasibility of and Boundary Conditions for Floating Offshore Wind Turbines*; Technische Universiteit Delft: Delft, Netherlands, 2002.

18. Tracy, C.C.H. Parametric Design of Floating Wind Turbines. Ph.D. Thesis, Massachusetts Institute of Technology, Boston, MA, USA, 2007.

19. Henderson, A.R.; Patel, M.H. On the modelling of a floating offshore wind turbine. *Wind Energy* **2003**, *6*, 53–86. [CrossRef]

20. Withee, J.E. Fully coupled dynamic analysis of a floating wind turbine system. Ph.D. Thesis, Massachusetts Institute of Technology, Cambridge, MA, USA, 2004.

21. Han, B.; Zhou, L.; Zhang, Z. LIDAR-assisted radial basis function neural network optimization for wind turbines. *IEEJ Trans. Electr. Electr.* **2018**, *13*, 195–200. [CrossRef]

22. Lee, J.; Hajela, P. Parallel genetic algorithm implementation in multidisciplinary rotor blade design. *J. Aircr.* **1996**, *33*, 962–969. [CrossRef]

23. Kusiak, A.; Zheng, H. Optimization of wind turbine energy and power factor with an evolutionary computation algorithm. *Energy* **2010**, *35*, 1324–1332. [CrossRef]

24. Liao, C.C.; Xi, G.; Xu, J.Z. An improved PSO algorithm for solution of constraint optimization problem and its application. *J. Eng. Thermophys.-Rus.* **2009**, *24*, 256–260. (In Chinese)

25. Liao, C.C.; Zhao, X.L.; Xu, J.Z. Blade layers optimization of wind turbines using FAST and improved PSO Algorithm. *Renew. Energy* **2012**, *42*, 227–233. [CrossRef]

26. Yang, H.; Chen, J.; Pang, X. Wind turbine optimization for minimum cost of Energy in low wind speed areas considering blade length and hub height. *Appl. Sci.* **2018**, *8*, 1202. [CrossRef]

Wind Turbine Control Using Nonlinear Economic Model Predictive Control over All Operating Regions

Xiaobing Kong [1], Lele Ma [1], Xiangjie Liu [1,*], Mohamed Abdelkarim Abdelbaky [1,2] and Qian Wu [1]

[1] The State Key Laboratory of Alternate Electrical Power System with Renewable Energy Sources,
    North China Electric Power University, Beijing 102206, China; kongxiaobing@ncepu.edu.cn (X.K.);
    1172127008@ncepu.edu.cn (L.M.); m_abdelbaky@ncepu.edu.cn (M.A.A.); wuqian@ncepu.edu.cn (Q.W.)
[2] Electrical Power and Machines Engineering Department, Faculty of Engineering, Cairo University,
    Giza 12613, Egypt
*   Correspondence: liuxj@ncepu.edu.cn

Abstract: With the gradual increase in the installed capacity of wind turbines, more and more attention has been paid to the economy of wind power. Economic model-predictive control (EMPC) has been developed as an effective advanced control strategy, which can improve the dynamic economy performance of the system. However, the variable-speed wind turbine (VSWT) system widely used is generally nonlinear and highly coupled nonaffine systems, containing multiple economic terms. Therefore, a nonlinear EMPC strategy considering power maximization and mechanical load minimization is proposed based on the comprehensive VSWT model, including the dynamics of the tower and the gearbox in this paper. Three groups of simulations verify the effectiveness and reliability/practicability of the proposed nonlinear EMPC strategy.

1. Introduction

As a consequence of energy shortages around the world, environmental protection requirements, and the higher cost of traditional power, renewable energy sources are receiving a great deal of attention worldwide nowadays. Wind energy becomes the dominant renewable energy source due to its plentifulness, cleanness, and economic advantages. By the ending of 2018, the cumulative installed capacity of wind is estimated to be more than 221 GW in China, with an increase of 19 GW and 25.9 GW in 2017 and 2018 respectively, accounting for 31.9% and 32.8% of global overall wind power capacity [1]. Therefore, enhancing the efficiency and economy of wind energy conversion systems has become an important issue to handle the growing need for energy.

Numerous control schemes have been applied in variable-speed wind turbine (VSWT) controller designs to enhance efficiency. Generally, PID controllers are widely used in the pitch control of wind turbine systems, which only focuses on decreasing the blades' mechanical loads within region three, as shown in Figure 1 [2]. A feedback gain-scheduled PI controller was designed to maximize the captured power and mitigate the mechanical loads, where the fixed-phase and gain-margins are obtained through a frequency response analysis [3]. In [4], a gain-scheduled L1 adaptive optimal controller is proposed for the VSWT control system, where the nonconvex optimization problem is solved by using a genetic algorithm based on a single linearized model of the wind-turbine (WT) system at different operating points. To obtain the rated generator power and reduce the mechanical load, a nonlinear-PI controller with an extended state-observer was developed in order to control the blade pitch angle [5]. Although these PI controllers have led to the effective steady-state performance

of VSWTs, the distortion of the transient performance according to variations in the wind speed is still a drawback. Additionally, PI/PID controllers offer good performance, but they still are not optimal [6].
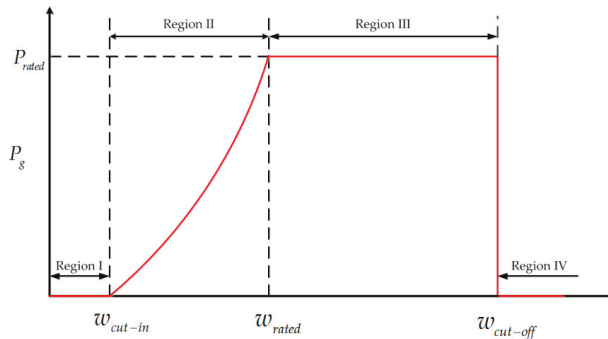

Figure 1. VSWT operation regions.

However, owing to multiple constraints, multiple variables, the highly coupled nonaffine basis of the VSWT systems, and the stochastic shape of wind speed input, high-performance wind turbine control (WTC) has become a challenging problem [7]. Various nonlinear control schemes have been applied to the WTC problem. In [8], an artificial neural network technique is proposed for the pitch control in region three, where the VSWT dynamics are modeled using a back-propagation learning algorithm. In [9], a fuzzy logic pitch controller is proposed for WTC, considering the generator power and speed as control inputs. In [10], a multiple feedback pitch controller is proposed for the nacelle fore-aft speed and generator power regulation. This controller is designed by employing a trade-off between pitch angle fluctuations and output power fluctuations. In [11], an adaptive neural pitch controller is proposed for the WTC problem. An online, two-layer neural network model is proposed for estimating the unknown wind turbine aerodynamics. Recently in [12], a T-S fuzzy modeling method with nonlinear consequents is proposed for the VSWT control problem. However, the wind turbine actuator constraints are not considered in the controller designs presented in these approaches, which may cause a wind-up phenomenon and significant performance deterioration if the actuator inputs reach saturation limits.

Among all the control strategies, model predictive control (MPC) is emerging as a powerful candidate for WTC thanks to its capacity to handle all the system constraints directly, such as physical limitations and operational constraints [13]. Classical MPC schemes have been used for WTC to ensure that the maximum power is captured in region two, and the rated power is tracked in region three. In [14,15], a linear MPC strategy is proposed based on a single linear state-space model to deal with the actuator constraints. Although these approaches have good performance concerning certain operating points and system constraints handling, no special attention has been paid to either the strong nonlinearity of the system or the mechanical load mitigation to enhance the economy of the VSWT system.

Some MPC techniques have been utilized by taking the wind turbine nonlinearity into account. In [16–18], a multivariable MPC is proposed for VSWT pitch control in region three, using Takagi-Sugeno (T-S) fuzzy models. In [19], a nonlinear MPC (NMPC) strategy is investigated for VSWT control for both regions two and three by tuning the penalty parameters. In [20,21], multiple model predictive controllers are proposed based on multiple linearized time-invariant state-space models, guaranteeing the actuator limits in all operation regions. However, it is obvious that the controller switching results in more difficulties. The authors take the load of WT into account as one of completing penalties based on a simplified nonlinear WT model. The shortcoming of these control schemes is the difficulty of adequately tuning the tracking weights; furthermore, economic factors are not considered in the design of the controller.

To enhance the dynamic economy, the economic MPC (EMPC) was developed for the VSWT system. Generally, the EMPC uses a measure of the system performance directly as an economic cost function [22]. However, the economic cost function may not be a positive definite with regard to any tracking trajectory in order to guarantee the stability of the operating points. In [23], the closed-loop stability of the system is guaranteed via terminal constraints depending on the strong duality assumption. In addition, in [24], a Lyapunov-based EMPC is constituted using two separate operation modes to make the closed-loop system ultimately bounded within a small region. In the context of the WTC problem, the EMPC objective function directly considers VSWT energy generation maximization against the actuator fatigue minimization, as opposed to tracking some reference states and inputs. The proposed NEMPC in this paper has a unique weight in the objective function, while the weights must be chosen carefully for every input and state in the classical NMPC strategy [19]. In addition, in [25,26], an EMPC strategy has been designed for wind turbine control systems for all regions. In [26], the wind speed is produced based on the Van der Hoven spectrum [27], in which the wind speed is considered as a slowly-changing average wind speed superposed by a rapidly-changing turbulence wind speed. However, these EMPC approaches pay no special attention to the mitigation of mechanical loads on the tower in the economic objective function. Additionally, different treatment of the random wind speed can be considered, consisting of summing the mean wind speed, which follows a two-parameter Weibull distribution, and the turbulent wind speed, which follows a zero-mean Gaussian, white noise distribution [28].

In this study, a nonlinear EMPC (NEMPC) strategy is proposed for all the operating regions of the VSWT system. A nonlinear VSWT model, which considers the tower and gearbox dynamics, is established. The NEMPC optimization problem considers all the actuator constraints (pitch angle, and torque constraints with their rate of change constraints) and the hard constraints (rotor speed, generator speed, and electrical power). The economic cost function seeks the maximum VSWT generated power against the competing penalties regardless of wind input, in order to achieve the best economic operation, as well as the fatigue load mitigation of key mechanical structures, including both drive-shaft torsion and tower fore-aft motion. This control strategy can provide potential improvements in the closed-loop performance, and satisfy the economy in contrast with classical WTC strategies. Finally, in the simulations, random wind speed is considered by summing the mean wind speed and the turbulent wind speed, which follow a two-parameter Weibull distribution and a zero-mean Gaussian white noise distribution, respectively.

The paper is organized as follows. The nonlinear modeling of the VSWT system is established in Section 2. The proposed NEMPC strategy is derived in Section 3. In Section 4, the simulation results for a 5-MW VSWT system are demonstrated, with comparisons between the classical NMPC strategy and the proposed NEMPC strategy. Also, in this section, a typical wind turbine benchmark simulator FAST is used to test the validity and practicability of the proposed NEMPC strategy. Lastly, Section 5 provides conclusions.

2. Wind Turbine Modeling

Wind-energy conversion systems consist of a windmill, a gearbox, and a generator, as demonstrated in Figure 2. In this section, nonlinear VSWT modeling is investigated. To establish this nonlinear model, the aerodynamics, tower, drive train, and the generator should be considered. In the following subsections, these subsystems are discussed separately. Finally, a nonlinear state-space model is established.
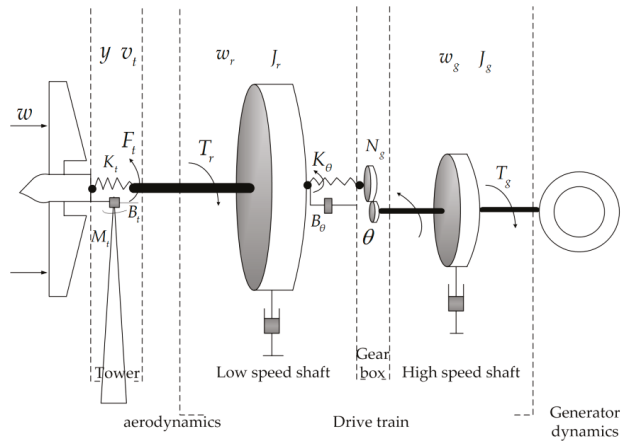
Figure 2. The mechanical structure of the VSWT generation system.

2.1. Rotor Aerodynamics

The airflow on VSWT blades causes aerodynamic torque, which represents one of the causes of VSWT nonlinearities. The aerodynamic torque T_r can be stated as below [29]:

$$T_r = \frac{1}{2}\rho\pi R^2 \frac{v_r^3}{w_r} C_p(\lambda(v_r, w_r), \beta) \tag{1}$$

The aerodynamic power that the VSWT extracts is expressed by [29]:

$$P^A = \frac{1}{2}\rho\pi R^2 v_r^3 C_p(\lambda(v_r, w_r), \beta) \tag{2}$$

where ρ is the air density, v_r represents the effective wind speed on the turbine rotor [30], R is the rotor radius of VSWT, w_r is the VSWT rotor angular speed, $C_p(\lambda(v_r, w_r), \beta)$ is the aerodynamic power coefficient, and β is the blade pitch angle. The tip speed ratio λ is defined as [30]:

$$\lambda(w_r, v_r) = \frac{Rw_r}{v_r} \tag{3}$$

The following approximate expression of the aerodynamic power coefficient derived from [18] is widely used:

$$C_p(\lambda, \beta) = c_1(\frac{c_2}{\Lambda} - c_3\beta - c_4) \times e^{-\frac{c_5}{\Lambda}} + c_6\lambda \tag{4}$$

where $1/\Lambda = 1/(\lambda + 0.08\beta) - 0.035/(1 + \beta^3)$, and the coefficients $c_i (i = 1, 2, \cdots, 6)$ depend on the blade shape and its aerodynamic performance [18,29]. In this paper, NREL 5-MW VSWT system is discussed; the six chosen coefficient values are [18]: $c_1 = 0.5176$, $c_2 = 116$, $c_3 = 0.4$, $c_4 = 5$, $c_5 = 21$, $c_6 = 0.0068$. This nonlinear function $C_P(\lambda, \beta)$ is indicated in Figure 3.
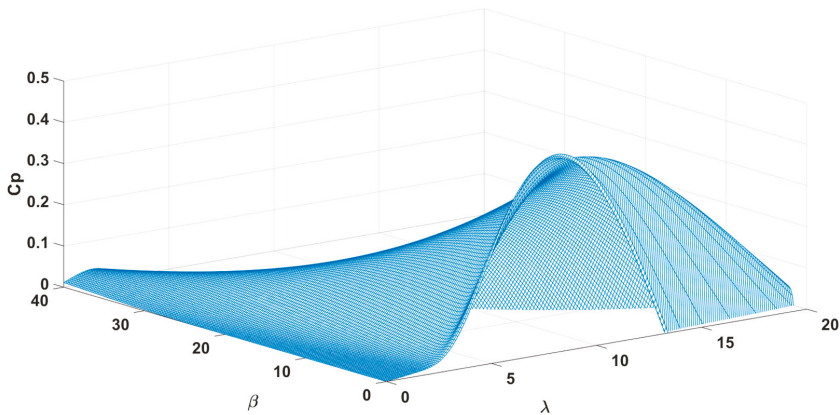
Figure 3. The aerodynamic power coefficient for 5-MW VSWT.

2.2. Tower Dynamics

The blade vibration results in the tower deflection. Thus, the thrust force on a tower top over the nacelle, which causes undesired nodding for the tower and fatigue loads on the VSWT, must be considered [31]:

$$F_t = \frac{1}{2}\rho\pi R^2 v_r{}^2 C_t(\lambda(v_r, w_r), \beta) \tag{5}$$

where $C_t(\lambda(v_r, w_r), \beta)$ is the thrust coefficient, which is the nonlinear function in terms of blade pitch angle β and tip speed ratio λ. By adopting a polynomial fitting algorithm based on the data-driven from a typical wind turbine benchmark simulator, the thrust coefficient can be derived as:

$$\begin{aligned} C_t(\lambda, \beta) = \quad & 0.08698 - 0.003371\beta - 0.053272\lambda + 0.06499\lambda^2 - 0.003096\beta\lambda^2 - 0.009575\lambda^3 \\ & + 0.0002103\beta\lambda^3 + 0.0005667\lambda^4 - 5.24 \times 10^{-6}\beta\lambda^4 - 1.199 \times 10^{-5}\lambda^5 \end{aligned} \tag{6}$$

where $C_t(\lambda, \beta)$ represents a nonlinear function, as indicated in Figure 4.
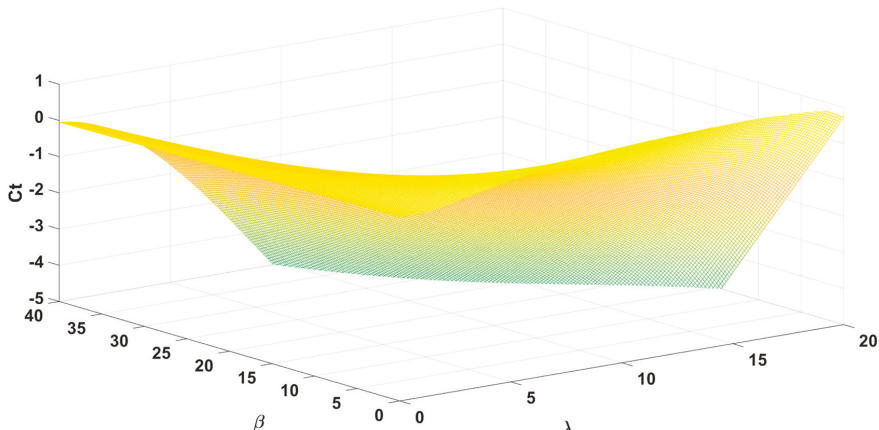
Figure 4. The thrust coefficient for 5-MW VSWT.

Thrust force towards the tower top over the nacelle causes tower fore-aft motion. The dynamics of tower fore-aft motion can be stated as a simplified second-order differential equation:

$$M_t \ddot{y} + B_t \dot{y} + K_t y = F_t \tag{7}$$

where M_t represents the mass model, B_t and K_t are the structural damping and structural stiffness coefficients of the tower model respectively, y represents the tower top displacement, and $\dot{y}$ is the tower deflection rate.

Tower fore-aft motion causes a nonnegligible effect on effective wind speed. The tower deflection rate is defined as $v_t = \dot{y}$. Thus, the effective (relative) wind speed v_r on the turbine rotor can be expressed with the normal wind speed w and the tower deflection as follows [30]:

$$v_r = w - v_t \tag{8}$$

The above formula shows that the actual wind speed acting on the blade is a relative wind speed, which is the difference between the natural wind speed w and the displacement speed of the tower v_t. It can be imagined that when the tower moves forward and backward in the horizontal direction with the wind speed, the wind speed acting on the blade is not exactly equal to the wind speed directly given by the natural environment. This formula makes the wind speed acting on the blade more accurate.

In Figure 2, w represents the nature wind speed towards the blade, which cannot be replaced by the relative (effective) wind speed v_r because the relative (effective) wind speed is just a virtual physical variable which is defined for the aerodynamic torque and power, not a real physical variable. Therefore, the relative (effective) wind speed v_r cannot appear before the blade, replacing wind speed w in Figure 2.

2.3. Drive Train

The wind mechanical energy is transformed through a drive train to the electrical generator. The drive train is rigidly coupled in the rotor side with a flexible connection in the generator side, as demonstrated in Figure 2. The shaft torsion represents the torque of the drive train flexible shaft, which is a vital factor affecting economic performance. Oscillations in the shaft torsion cause damage to the turbine components. The shaft torsion is replaced by the absolute angular position of the generator and rotor; its derivative is [17]:

$$\dot{\theta} = w_r - \frac{w_g}{N_g} \tag{9}$$

where θ is the shaft torsional angle, w_g is the generator angular speed, and N_g is the gearbox ratio.

Assuming that the low-speed shaft is one spring and one damper, the two-mass model is used to describe the drive train from a low- to a high-speed shaft through a gearbox as follows [17,26]:

$$J_r \dot{w}_r = T_r - K_\theta \theta - B_\theta \dot{\theta} \tag{10}$$

$$J_g \dot{w}_g = -T_g + \frac{K_\theta}{N_g} \theta + \frac{B_\theta}{N_g} \dot{\theta} \tag{11}$$

where J_r is the inertia of the VSWT rotor and the low-speed shaft, J_g is the inertia of the generator, K_θ and B_θ represent the stiffness and damping of the drive train, T_g is the generator torque.

2.4. Generator

The electrical generator power P^E can be derived as [17]:

$$P^E = \eta_g w_g T_g \tag{12}$$

where η_g represents the generator and power efficiency. Ignoring the losses, the derivation between P^A (the mechanical power) and P^E stems notably from the energy tentatively stored as the rotor kinetic energy [25].

2.5. The Nonlinear State-Space Model of VSWT

Based on Equations (1)–(12), the nonlinear dynamics of the VSWT system can be transformed into the following nonlinear state-space form:

$$\begin{aligned}\dot{x} &= f_c(x, u, w)\\ y &= g_c(x, u, w)\end{aligned} \tag{13}$$

where $g_c(x, u, w) = \begin{bmatrix} w_g \\ \eta_g w_g T_g \end{bmatrix}$, $f_c(x, u, w) = \begin{bmatrix} -\frac{B_\theta}{J_g N_g^2}w_g + \frac{B_\theta}{J_g N_g}w_r + \frac{K_\theta}{J_g N_g}\theta - \frac{1}{J_g}T_g \\ \frac{B_\theta}{J_r N_g}w_g - \frac{B_\theta}{J_r}w_r - \frac{K_\theta}{J_r}\theta + \frac{\pi}{2J_r}\rho_a R_r^2 \frac{(w-v_t)^3}{w_r}C_p(\lambda, \beta) \\ -\frac{w_g}{N_g} + w_r \\ v_t \\ -\frac{K_t}{M_t}y - \frac{B_t}{M_t}v_t + \frac{\pi}{2M_t}\rho_a R_r^2(w-v_t)^2 C_t(\lambda, \beta) \end{bmatrix}$.

Define the state variables, input variables, and output variables as: $x = \begin{bmatrix} w_g & w_r & \theta & y & v_t \end{bmatrix}^T$, $u = \begin{bmatrix} T_g & \beta \end{bmatrix}^T$, $y_o = \begin{bmatrix} w_g & P^E \end{bmatrix}^T$. Then, the discrete wind turbine system model (13) can be obtained by forth stage Runge–Kutta (RK4) method with the sampling time T,

$$\begin{aligned}x(k+1) &= f(x(k), u(k), w(k)) = x(k) + \frac{T}{6}(k_1 + 2k_2 + 2k_3 + k_4)\\ y(k) &= g(x(k), u(k), w(k))\end{aligned} \tag{14}$$

where $k_1 = f_c(x(k), u(k))$, $k_2 = f_c(x(k) + \frac{T}{2}k_1, u(k))$, $k_3 = f_c(x(k) + \frac{T}{2}k_2, u(k))$, $k_4 = f_c(x(k) + Tk_3, u(k))$, $g(x(k), u(k), w(k)) = g_c(x, u, w)$.

3. NEMPC Strategy for VSWT Control

EMPC for WTC seeks the optimal operation between the maximization of the generated power and the minimization of the cost related to care and maintenance. In a real wind farm, the oscillatory transient of tower deflection and shaft torsion can create microcracks in the materials, which can lead to component failure and increase maintenance costs. Therefore, not only generated power, pitch-angle and generator-torque, but also shaft torsion angle and tower displacement are considered in the economic cost function for the reduction of fatigue loads in this paper.

3.1. Economic Cost Function

In this paper, economic indexes are defined as follows. Firstly, the generator power must be considered in the economic index l_{e1} to capture the maximum power [19]:

$$l_{e1}(x, u) = -\lambda_1 P^E \tag{15}$$

Secondly, the shaft torsional angle and tower displacement must be considered in the economic index l_{e2} to reduce the fatigue of the tower structure caused by the tower deflection [19] and the gearbox load caused by the drive-shaft torsion [26]:

$$l_{e2}(x, u) = \lambda_2 \theta^2 + \lambda_3 v_t^2 \tag{16}$$

Finally, the pitch-angle and generator-torque must be considered in the economic indexes l_{e3} and l_{e4}, respectively, to smoothen the control performance and reduce the fluctuations of the output electric power [19]:

$$l_{e3}(x, u) = \lambda_4 \Delta\beta^2 + \lambda_5\beta^2 \tag{17}$$

$$l_{e4}(x, u) = \lambda_6 \Delta T_g^2 \tag{18}$$

where λ_1, λ_2, λ_3, λ_4, λ_5, and λ_6 are weighted coefficients.

In designing the NEMPC for the VSWT system, the economic cost function can be obtained as:

$$l_e(x, u) = l_{e1} + l_{e2} + l_{e3} + l_{e4} \tag{19}$$

which aims to decrease the load and fatigue on the wind power system and smooth the generator torque input and the output power while capturing the maximal power.

3.2. The Operational and Physical Constraints

Due to the electrical limitations of the actuator electronics and the safety requirements of the control process, a set of physical constraints must be fulfilled during operation in VSWT. Thus, the following set of constraints must be taken into consideration along the predictive/control horizon:

$$w_{g\min} \leq w_g \leq w_{g\max} \quad w_{r\min} \leq w_r \leq w_{r\max} \quad \theta \geq \theta_{\min} \tag{20}$$

$$0 \leq T_g \leq T_{g\max} \quad -\Delta T_{g\max} \leq \Delta T_g \leq \Delta T_{g\max} \tag{21}$$

$$\beta_{\min} \leq \beta \leq \beta_{\max} \quad -\Delta\beta_{\max} \leq \Delta\beta \leq \Delta\beta_{\max} \tag{22}$$

$$0 \leq P^E \leq P^E_{\max} \tag{23}$$

where the maximum rotor speed $w_{r\max}$, generator speed $w_{g\max}$, and torque $T_{g\max}$ are set slightly higher than their rated values $w_{r\ rated}$, $w_{g\ rated}$, and $T_{g\ rated}$. The definition and values of related parameters are listed in Table A2 in Appendix A [19,32].

3.3. The Optimization Problem for the Proposed NEMPC Strategy

Based on the above nonlinear model and cost function in Sections 3.1 and 3.2, the optimization problem for the proposed NEMPC strategy can be summed up as follows:

$$\min J = \sum_{i=1}^{N_P} l_e(x(k+i-1|k), u(k+i-1|k))$$
$$s.t.$$
$$x(k+i|k) = f(x(k+i-1|k), u(k+i-1|k), w(k+i-1)), i = 1, \cdots, N_P, x(k|k) = x(k) \tag{24}$$
$$y(k+i-1|k) = g(x(k+i-1|k), u(k+i-1|k), w(k+i-1))$$
$$\Delta u(k+i|k) = u(k+i|k) - u(k+i-1|k)$$
$$equation(20) - equation(23)$$

Define $\mathbf{X} = \begin{bmatrix} x(k+1|k)^T & x(k+2|k)^T & \cdots & x(k+N_P|k)^T \end{bmatrix}^T$, $\mathbf{U} = \begin{bmatrix} u(k|k)^T & u(k+1|k)^T & \cdots & u(k+N_P-1|k)^T \end{bmatrix}^T$, $\mathbf{\Delta U} = \begin{bmatrix} \Delta u(k|k)^T & \Delta u(k+1|k)^T & \cdots & \Delta u(k+N_P-1|k)^T \end{bmatrix}^T$, $\mathbf{P}^E = \begin{bmatrix} P^E(k|k) & \cdots & P^E(k+N_P-1|k) \end{bmatrix}^T$, where N_P is the predictive/control horizon.

Define $\Phi = \begin{bmatrix} \mathbf{X} & \mathbf{U} & \mathbf{\Delta U} & \mathbf{P}^E \end{bmatrix}^T$ as the new optimal variables set. Then, the optimization problem (24) can be rewritten as:

$$\min J$$
$$s.t.$$
$$Aeq\Phi = bu(k-1),$$
$$Ceq_i(\Phi) = \begin{bmatrix} x(k+i|k) - f(x(k+i-1|k), u(k+i-1|k), w(k+i-1)) \\ \hat{P}^E(k+i-1|k) - g(x(k+i-1|k), u(k+i-1|k), w(k+i-1)) \end{bmatrix}_{i=1,\cdots,N_P,\hat{x}(k|k)=x(k)} = 0 \tag{25}$$
$$\Phi_{\min} \leq \Phi \leq \Phi_{\max}$$

$$Aeq = \begin{bmatrix} 0 & I & -S & 0 \end{bmatrix}_{2N_P \times 10N_P}, b = \begin{bmatrix} I & I & \cdots & I \end{bmatrix}_{2N_P \times 2N_P}^{T}$$

where

$$S = \begin{bmatrix} I & 0 & \cdots & 0 \\ I & I & & 0 \\ \vdots & \vdots & \ddots & \\ I & I & \cdots & I \end{bmatrix},$$

$$\Phi_{\min} = \begin{bmatrix} X_{\min} & U_{\min} & \Delta U_{\min} & \hat{P}^E_{\min} \end{bmatrix}, \Phi_{\max} = \begin{bmatrix} X_{\max} & U_{\max} & \Delta U_{\max} & \hat{P}^E_{\max} \end{bmatrix}$$

$$X_{\min} = \begin{bmatrix} x_{\min} \\ x_{\min} \\ \vdots \\ x_{\min} \end{bmatrix}, X_{\max} = \begin{bmatrix} x_{\max} \\ x_{\max} \\ \vdots \\ x_{\max} \end{bmatrix}, U_{\min} = \begin{bmatrix} u_{\min} \\ u_{\min} \\ \vdots \\ u_{\min} \end{bmatrix}, U_{\max} = \begin{bmatrix} u_{\max} \\ u_{\max} \\ \vdots \\ u_{\max} \end{bmatrix},$$

$$\Delta U_{\min} = \begin{bmatrix} \Delta u_{\min} \\ \Delta u_{\min} \\ \vdots \\ \Delta u_{\min} \end{bmatrix}, \Delta U_{\max} = \begin{bmatrix} \Delta u_{\max} \\ \Delta u_{\max} \\ \vdots \\ \Delta u_{\max} \end{bmatrix}, \hat{P}^E_{\min} = \begin{bmatrix} 0 \\ 0 \\ \vdots \\ 0 \end{bmatrix}, \hat{P}^E_{\max} = \begin{bmatrix} P^E_{\max} \\ P^E_{\max} \\ \vdots \\ P^E_{\max} \end{bmatrix},$$

$$x_{\min} = \begin{bmatrix} w_{g\,\min} & w_{r\,\min} & \theta_{\min} & y_{\min} & v_{t\,\min} \end{bmatrix}^T, u_{\min} = \begin{bmatrix} T_{g\,\min} & \beta_{\min} \end{bmatrix}^T, \Delta u_{\min} = \begin{bmatrix} \Delta T_{g\,\min} & \Delta \beta_{\min} \end{bmatrix}^T.$$

$$x_{\max} = \begin{bmatrix} w_{g\,\max} & w_{r\,\max} & \theta_{\max} & y_{\max} & v_{t\,\max} \end{bmatrix}^T, u_{\max} = \begin{bmatrix} T_{g\,\max} & \beta_{\max} \end{bmatrix}^T, \Delta u_{\max} = \begin{bmatrix} \Delta T_{g\,\max} & \Delta \beta_{\max} \end{bmatrix}^T.$$

The optimization problem (25) can be solved by using the interior point method, which is realized by using IPOT solver in MATLAB [33]. Then, the optimal solution of the control inputs (pitch angle and the generator torque) at the current time can be extracted and implemented.

4. Simulations Results

Three simulations are performed based on a typical 5-MW NREL VSWT system to validate the proposed NEMPC strategy. The corresponding parameters of the 5-MW NREL VSWT system are listed in Table A1 in the Appendix A [32]. The corresponding constraints are shown in Table A2 [19,32]. In the simulations, the weights in the cost function (15)–(18) contain: $\lambda_1 = 20, \lambda_2 = 100, \lambda_3 = 5 * 10^8, \lambda_4 = 1, \lambda_5 = 0, \lambda_6 = 0.001$. The maximum generator speed, rotor speed, and generator torque are all arbitrarily set at 5% above their rated values, i.e., $w_{g\max} = 1.05 w_{g\,rated}$, $w_{r\max} = 1.05 w_{r\,rated}$, $T_{g\max} = 1.05 T_{g\,rated}$. For the purpose of simplicity, the maximum electric power is chosen as $P^E_{\max} = P^E_{rated}$.

For comparison purposes, the classical NMPC strategy based on [19] is also constituted, which has the same model (13) and constraints (20)–(23) as the proposed NEMPC strategy in this paper. However, the tracking objective function (not economic cost function) is used in the classical NMPC, which can be described as:

$$l_{mpc}(x,u) = \sum_{i=1}^{N_P} \left[Q_\Omega \big(w_r(k+i-1|k) - w_{r\,ref}(w) \big)^2 + Q_\beta (\beta(k+i-1|k) - \beta_{ref}(w))^2 \right] \tag{26}$$

where $Q_\Omega = 3.4 \times 10^7$, $Q_\beta = 4.6 \times 10^8$ for the wind speed region II, $Q_\Omega = 3.4 \times 10^5$, $Q_\beta = 4.6 \times 10^5$ for wind speed region III, $\beta_{ref}(w)$ is the pitch angle reference and $w_{r\,ref}(w)$ is the rotor speed reference, which can be derived as:

$$w_{r\,ref}(w) = \begin{cases} w_r^*(w) & if & w_r^*(w) \in [w_{r\,cut-in}, w_{r\,rated}] \\ w_{r\,cut-in} & if & w_r^*(w) < w_{r\,cut-in} \\ w_{r\,rated} & if & w_r^*(w) > w_{r\,rated} \end{cases}, \beta_{ref}(w) = \begin{cases} \beta^*(w) & if & w \le w_{rated} \\ \beta_{AR}(w) & if & w > w_{rated} \end{cases} \tag{27}$$

β^* and λ^* in Equation (27) are the optimal pitch angle and tip ratio in wind speed region II as demonstrated in Figure 1, can be derived via maximizing the power coefficient C_P:

$$\beta^*, \lambda^* = \max_{\beta, \lambda} C_P(\beta, \lambda) \tag{28}$$

Then, the optimal rotor speed w_r^* can be obtained:

$$w_r^*(w) = \frac{\lambda^* w}{R} \tag{29}$$

$\beta_{AR}(w)$ in Equation (27) can be solved from: $\frac{1}{2}\rho A C_P \left(\beta_{AR}(w), \frac{R w_{r\,rated}}{w}\right) w^3 = P_{rated}$.

The predictive/control horizon is set as $N_P = 14$ for both classical NMPC and the proposed NEMPC in the following three groups of simulations.

4.1. Gradient Normal Wind

As indicated in Figure 5, a gradient normal wind varying between 7.5 m/s and 15 m/s is used in the simulation. The initial condition is set as $x_0 = \begin{bmatrix} 93.54 & 0.96 & 1.85 \times 10^{-3} & 0.21 & 0 \end{bmatrix}^T$, *and* $t_0 = 0$. All the input variables, state variables, and output variables adopting both the proposed NEMPC and the classical NMPC strategies are shown as Figure 6a–h. During the time period from 0 s to 50 s, all the dynamic trajectories are almost the same when using the proposed NEMPC and the classical NMPC strategies, because the chosen initial state is just the optimal solution for both controllers under the initial 7.5 m/s normal wind speed.
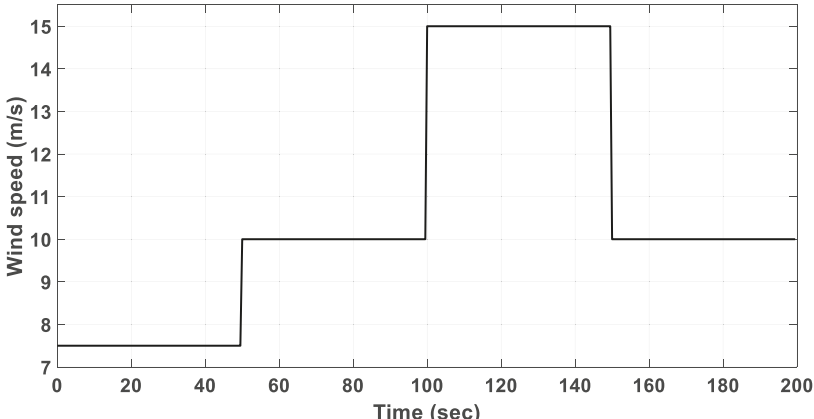
Figure 5. Gradient wind speed.

At time instant 50 s, the normal wind speed steps from 7.5 m/s to 10 m/s, which is below the rated wind speed. Obviously, the VSWT system remains working in region II by using the classical NMPC strategy, which aims to follow the maximum power point and keeps the pitch angle zero. The proposed NEMPC strategy aims to attain a trade-off between the power maximization and turbine fatigue minimization by minimizing the economic cost function (19). Therefore, the pitch-angle is not always kept at zero, while the vibrations of the shaft torsion angle, the tower displacement, and the generation torque are much slighter when using the proposed NEMPC strategy, as shown in Figure 6c–f. No constraints are violated due to the constraints in Equations (20)–(23), which are imposed in both the classical NMPC strategy and the proposed NEMPC strategy, as seen in Figure 6.

At time instant 100 s, the normal wind speed steps from 10 m/s to 15 m/s, which is above the rated wind speed. Therefore, the working region of the VSWT system changes from region II to region

III. The aim of the classical NMPC changes from the maximization power capturing to rated power capturing. The generator speed, rotor speed, generator torque, and generator power are changed to the rated values. Simultaneously, the pitch angle is enabled. As shown in Figure 6c–f, the vibration of the shaft torsional angle, the pitch angle, and especially the tower displacement, is much smaller when using the proposed NEMPC strategy than when using the classical NMPC strategy, due to θ, v_t and β being considered in the economic cost function (19).
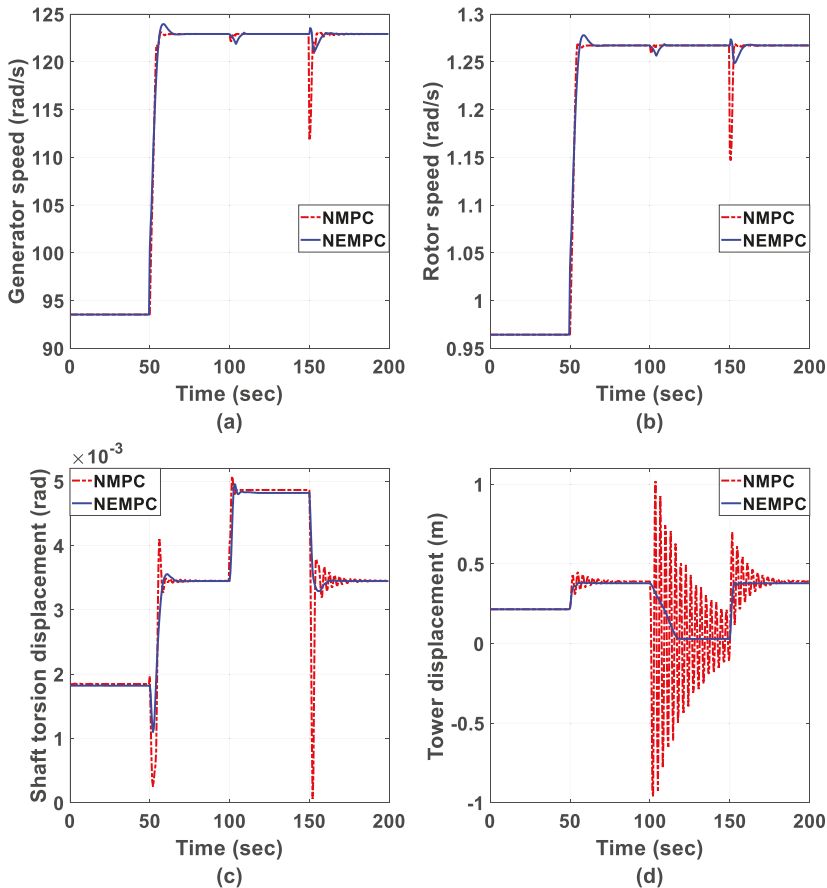
Figure 6. *Cont.*
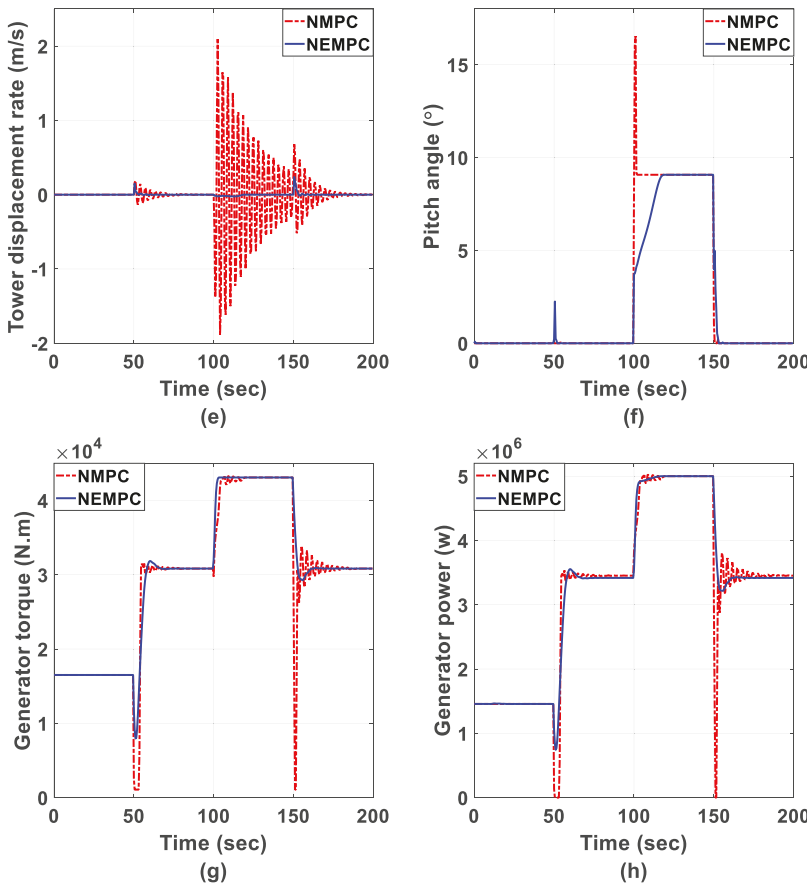
Figure 6. (**a**) Generator speed; (**b**) Rotor speed; (**c**) Shaft torsional angle; (**d**) Tower displacement; (**e**) Tower displacement rate; (**f**) Pitch angle; (**g**) Generator torque; (**h**) Generator power.

At time instant 150 s, the normal wind speed decreases from 15 m/s to 10 m/s. Thus, the wind turbine works back to region II. The pitch angle is disabled, the generator speed, rotor speed, and generator torque are performed to follow the maximum power point by using the classical NMPC strategy. From 6b–h, it is obvious that the vibration of each state variable is much more severe when using the classical NMPC strategy compared with the proposed NEMPC strategy. This is because the shaft load and the tower fatigue are not considered in the tracking objective function (26) for the classical NMPC strategy, while they are emphasized in the economic cost function (19) for the proposed NEMPC strategy. Vibrations in the shaft torsional angle, the tower displacement, and the tower displacement rate are harmful to wind turbine systems. Thus, the proposed NEMPC strategy is much better than the classical NMPC strategy in this respect.

From a more intuitive point of view, numerical comparisons have been made to illustrate the difference between these two controllers. Define the root mean square (RMS) values of mechanical loads as follows:

$$RMS_{shaft} = \sqrt{\frac{1}{Nsim} \sum_{k=1}^{Nsim} \theta^2(k)} \tag{30}$$

$$RMS_{tower} = \sqrt{\frac{1}{Nsim} \sum_{k=1}^{Nsim} v_t^2(k)} \tag{31}$$

where $Nsim$ is the length of the simulation, RMS_{shaft} is the RMS value of gearbox load on the shaft, RMS_{tower} is the RMS value of fatigue on the tower.

As shown in Table 1, the average values of generator power $AVG(P_g)$, the RMS values of the gearbox load on shaft RMS_{shaft}, and the RMS values of fatigue on tower RMS_{tower} by adopting both the proposed NEMPC strategy and the classical NMPC strategy at different normal wind speed are listed for comparison purposes.

Table 1. Data analysis based on the results in Figure 6.

	7.5 m/s	10 m/s	15 m/s	10 m/s
$AVG(P_g^{NEMPC})$ (MW)	1.4575	3.1873	4.9493	3.4317
$AVG(P_g^{NMPC})$ (MW)	1.4570	3.1714	4.9343	3.3323
RMS_{shaft}^{NEMPC} ($\times 10^{-3}$ rad)	1.820	3.288	4.784	3.416
RMS_{shaft}^{NMPC} ($\times 10^{-3}$ rad)	1.846	3.300	4.851	3.476
RMS_{tower}^{NEMPC} ($\times 10^{-2}$ m/s)	0	1.643	1.10	3.31
RMS_{tower}^{NMPC} ($\times 10^{-2}$ m/s)	0	4.483	76.58	16.44

From Table 1, it is obvious that the proposed NEMPC strategy enhances the average generator power over the classical NMPC strategy by 0.03%, 0.5%, 0.3%, and 2.98%, when the normal wind speeds are 7.5 m/s, 10 m/s, 15 m/s, and 10 m/s, respectively. During different normal wind speed periods, the proposed NEMPC strategy reduces the gearbox load on the shaft over the classical NMPC strategy by 1.41%, 0.36%, 1.38%, and 1.73%, respectively. Furthermore, it is obvious that the proposed NEMPC strategy reduces the tower fatigue a lot compared to the classical NMPC strategy from the RMS values of the fatigue on the tower, which proves that the fatigue on the tower can't be ignored with regards to economic factors.

4.2. Stepwise Normal Wind

In general, 11.4 m/s represents the rated wind-speed, which is used to divide the wind speed into region II and III. Due to the different control objectives in regions II and III, a switching controller is widely used in the actual control of VSWT, which is a great challenge in controller design. To achieve the various operational requirements, the objective function of the classical NMPC strategy switches frequently according to wind speed operating regions. Thus, the rated wind speed 11.4 m/s is actually a very important speed in practical controller designs for VSWT systems.

The proposed NEMPC strategy in this paper adopts a unique economic cost function (19) which does not change according to the normal wind speed between the cut-in and cut-off wind speeds. Suppose the stepwise wind speed is initially set to 10.6 m/s, then steps to 12 m/s with an increment of 0.2 m within 25 s (from region II to region III), as shown in Figure 7a. As indicated in Figure 7b, it's obvious that the pitch angle has a quick and small overshoot, before quickly returning to zero before t = 125 s. After 125 s, the fluctuations of the pitch angle accumulate around a certain optimal value when the proposed NEMPC strategy is used. At 125 s, the wind speed changes from 11.4 m/s to 11.6 m/s. This means that the special wind speed is around 11.4 m/s due to the economic objective function (19), above which the stable pitch angle no longer remains at zero. Thus, these simulation results prove that a wind speed of around 11.4 m/s was set to divide the region II and III, which is reasonable for considering the economic operation of the VSWT system.
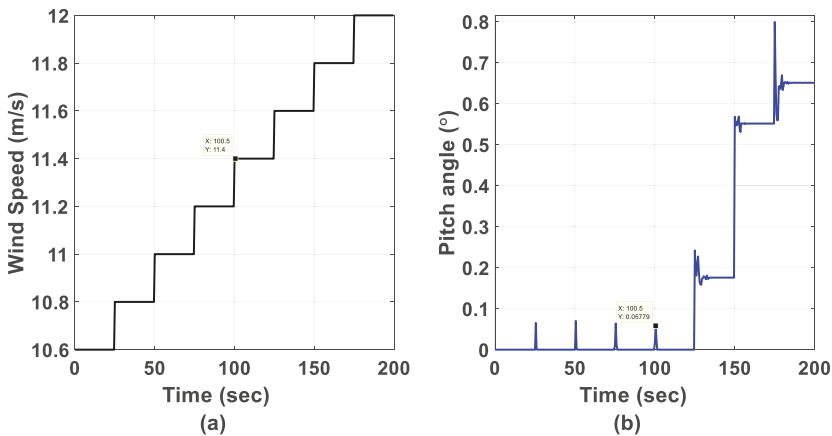
Figure 7. (**a**) Stepwise wind speed; (**b**) Pitch angle.

4.3. Randomly Varying Wind Speed Based on the FAST Simulator

The NREL FAST is an inclusive aeroelastic simulator of two- and three-bladed horizontal-axis WTs [34]. To validate the practicality and validity of the proposed NEMPC strategy, the simulation is then tested on NREL FAST. In this group of simulations, a FAST subroutine was written into the MATLAB S-function, as indicated in Figures 8 and 9.
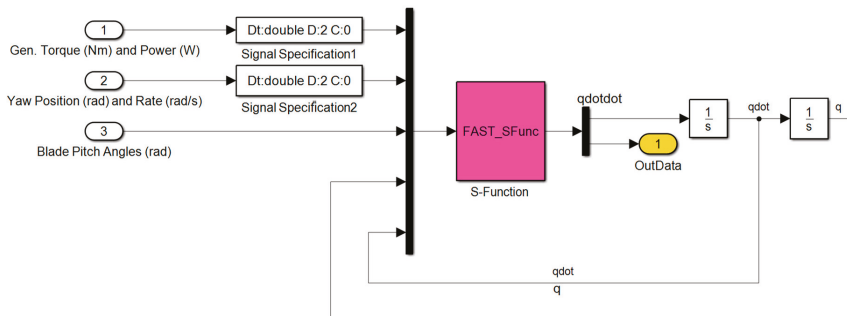
Figure 8. The FAST S-Function Block.
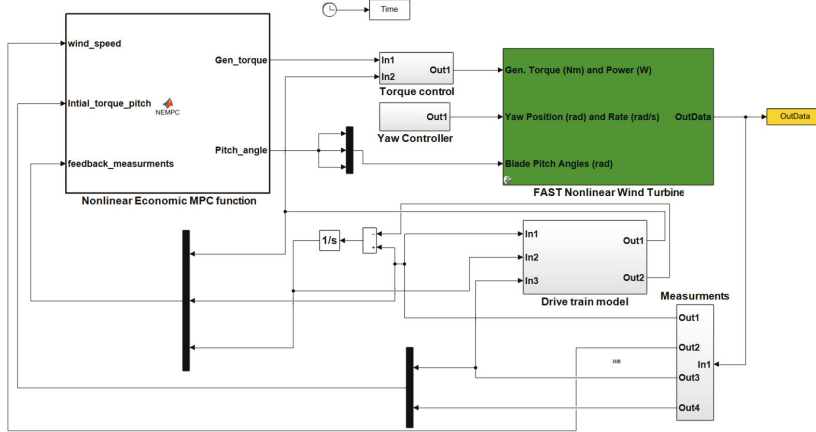
Figure 9. Simulation structure.

The normal wind speed w is always modeled as the combination of a slowly-changing mean wind-speed w_m and a rapidly-changing turbulent wind-speed w_d:

$$w = w_m + w_d \tag{32}$$

where we suppose that w_m follows the two-parameter Weibull distribution through a scale parameter $s1 = 10$ and shape parameter $s2 = 14$, and w_d follows zero-mean Gaussian white noise distribution with standard variation $\sigma = 1.899$ [28].

Then, a group of 600 s random normal wind speed data generated by the FAST simulator as indicated in Figure 10 is adopted in Case 3. The initial condition is set as $x_0 = \begin{bmatrix} 99.77 & 1.03 & 2.1 \times 10^{-3} & 0.25 & 0 \end{bmatrix}^T$, $t_0 = 0$. Figure 11a–h indicate the performances of the generator speed, rotor speed, shaft torsion angle, tower displacement, tower displacement rate, pitch angle, generator torque, and generator power via the proposed NEMPC strategy.
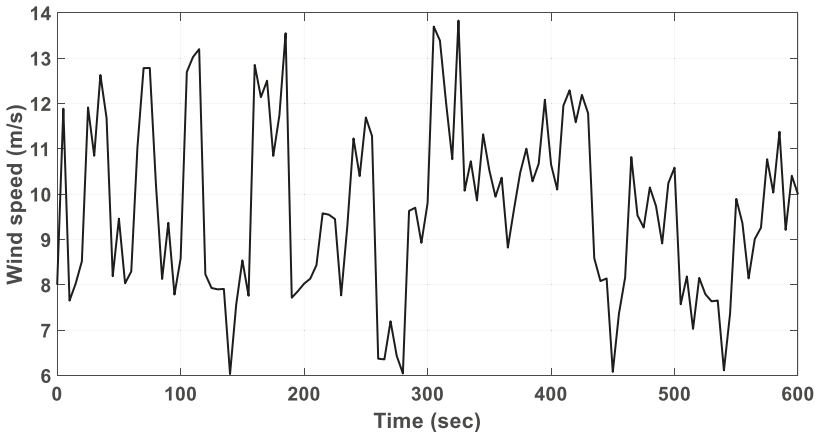
Figure 10. Wind speed.

From a more intuitive viewpoint, it can be observed that the performances of the proposed NEMPC strategy outperform the classical NMPC strategy. More specifically, the classical NMPC strategy shows

more noticeable fluctuations in the performance of generator power, shaft torsion displacement, tower displacement, generator torque, and pitch angle when the wind speed has a sudden increase around its rated wind speed, i.e., 11.4 m/s, compared with the proposed NEMPC scheme.

Meanwhile, the classical NMPC strategy shows more successive fluctuations in the performance of generator power, shaft torsion displacement, tower displacement, generator torque, and pitch angle when the normal wind speed has a sudden drop around the rated wind speed, compared with the proposed NEMPC strategy.

As shown in Figure 11d–e, the tower displacement and the tower displacement by using the classical NMPC strategy fluctuates more severely according to the wind speed variation compared with the proposed NEMPC strategy, due to the economic index l_{e2} related with the tower displacement considered in the economic cost function (19) for the proposed NEMPC. It is similar in the performances of the generator power, shaft torsion displacement, generator torque, and pitch angle, as shown in Figure 10. It can be concluded that the proposed NEMPC strategy decreases the operating costs while maintaining energy utilization, compared with the classical NMPC strategy. This is especially obvious when the wind speed varies around the rated wind speed. From Table 2, it is obvious that the proposed NEMPC strategy enhances the average generator power over the classical NMPC strategy by 0.67%, 1.05%, 0.28%, and 1.75%, when the average wind speeds are 9.7 m/s, 9.4 m/s, 10.8 m/s, and 9 m/s, respectively.
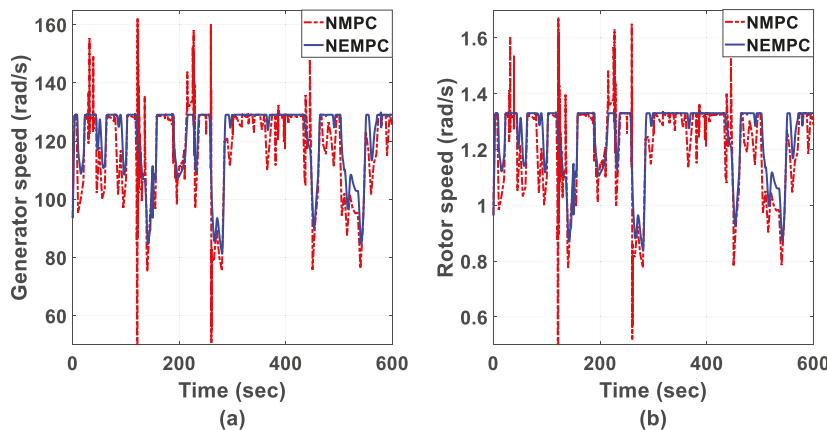
Figure 11. *Cont.*
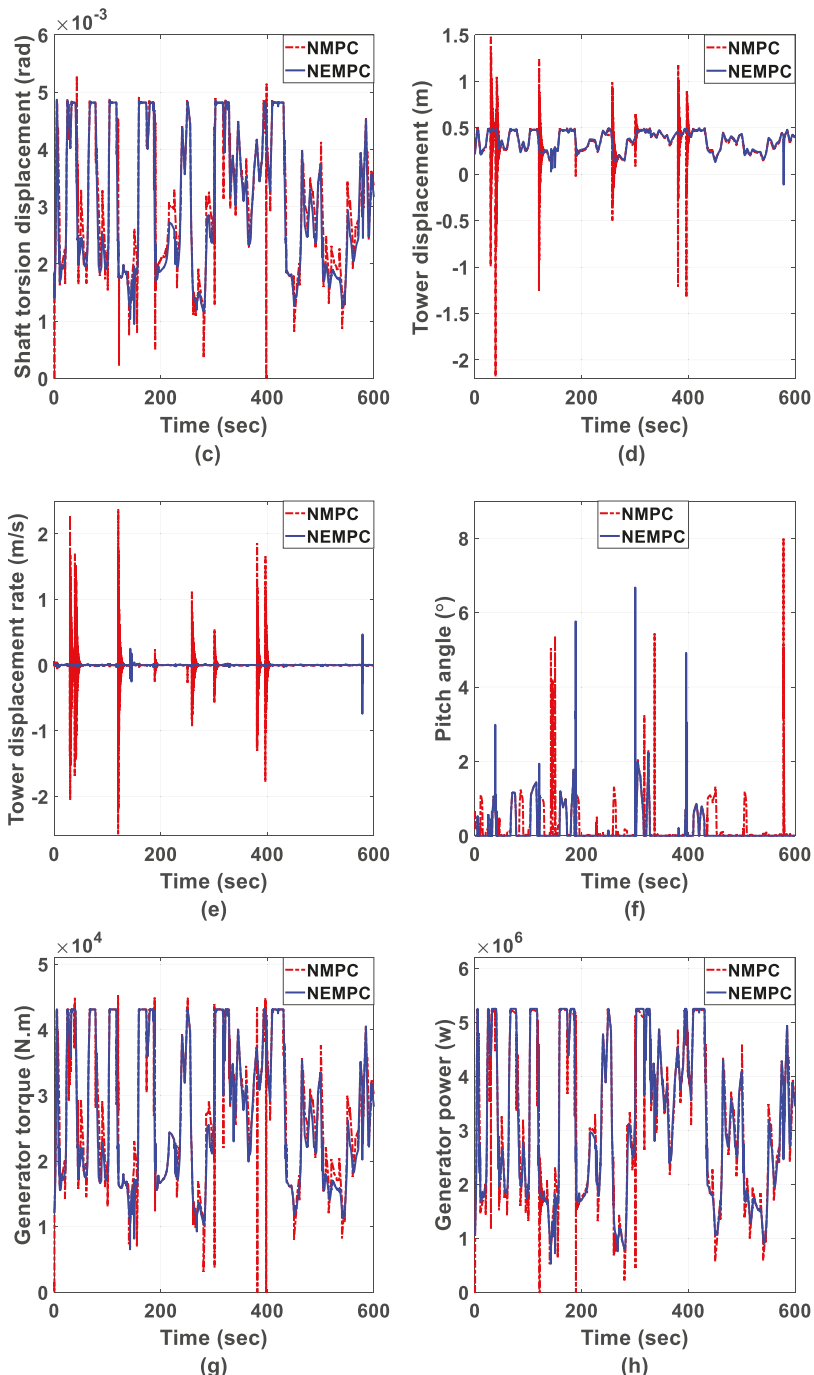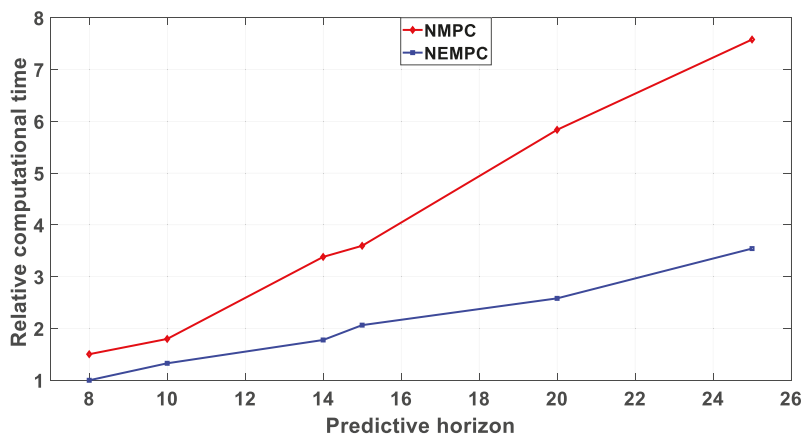
**Figure 11.** (**a**) Generator speed; (**b**) Rotor speed; (**c**) Shaft torsional angle; (**d**) Tower displacement; (**e**) Tower displacement rate; (**f**) Pitch angle; (**g**) Generator torque; (**h**) Generator power.

Table 2. Data analysis based on the results in Figure 11.

	9.7 m/s	9.4 m/s	10.8 m/s	9 m/s
$AVG(P_g^{NEMPC})$ (MW)	3.1162	2.9598	4.1231	2.5662
$AVG(P_g^{NMPC})$ (MW)	3.095	2.9291	4.1116	2.5221
$RMS_{shaft}^{NEMPC}(\times 10^{-3}$ rad)	3.234	3.092	3.913	2.581
RMS_{shaft}^{NMPC} ($\times 10^{-3}$ rad)	3.365	3.215	3.939	2.761
RMS_{tower}^{NEMPC} ($\times 10^{-2}$ m/s)	36.38	35.80	42.59	33.40
RMS_{tower}^{NMPC} ($\times 10^{-2}$ m/s)	39.44	35.83	43.22	32.86

During different average wind speed periods, the proposed NEMPC strategy reduces the gearbox load on the shaft over the classical NMPC strategy by 4.05%, 3.96%, 0.68%, and 6.96%, respectively. Furthermore, it is obvious that the proposed NEMPC strategy reduces the tower fatigue a lot compared to the classical NMPC strategy from the RMS values of the fatigue on the tower. Therefore, this group of simulation-based FAST verifies the economy of the proposed NEMPC strategy.

It is well known that the computational burden of nonlinear MPC strategies increases exponentially according to the incensement of the predictive horizon. Various predictive horizons have been considered to investigate the computational burden by using classical NMPC and the proposed NEMPC strategies. The relative computational times of these two controllers are indicated in Figure 12. From Figure 12, it is obvious that the computational time of the proposed NEMPC is much smaller than the classical NMPC with the same predictive horizon. Simultaneously, the computational time of the classical NMPC increases more rapidly according to the incensement of the predictive horizon, compared with the proposed NEMPC strategy.

Figure 12. Relative computational times for various predictive horizons.

5. Conclusions

In this paper, the tower displacement and shaft torsional angle are taken into consideration in the development of a nonlinear model for a 5-MW VSWT system. Based on this comprehensive model, a NEMPC strategy for the VSWT system is proposed to increase the dynamic economy, i.e., through power generation maximization and fatigue load minimization during operation. Three groups of simulations for comparisons with the classical NMPC strategy demonstrate the effectiveness of the proposed NEMPC strategy. The simulation under random wind speeds based on the FAST simulator verified the reliability practicability of the proposed NEMPC strategy.

The contributions of this study compared with other current studies can be outlined as follows: Firstly, the tower dynamics are focused on in the modeling process for the VSWT with flexible connections on the shaft, and the tower displacement is considered as a part of the economic objective function, which can reduce tower fatigue. Secondly, all the related operational constraints and physical constraints in the VSWT system with flexible connections on the shaft are considered in the proposed NEMPC strategy in detail. Finally, simulations based on the FAST simulator, which is a realistic WT simulator for testing the system's validity and practicability, were performed to show the practical implementation of the proposed controller using a turbulence wind speed profile. A future research topic is the design of a robust EMPC strategy taking into account the uncertainty of wind speed.

Author Contributions: Conceptualization, X.K. and M.A.A.; methodology, X.K.; software, M.A.A. and Q.W.; validation, X.K., M.A.A., and Q.W.; formal analysis, X.K.; investigation M.A.A. and Q.W.; resources, L.M. and X.L.; data curation, X.K.; writing—original draft preparation, M.A.A. and Q.W.; writing—review and editing, X.K., L.M. and X.L.; visualization, X.K.; supervision, L.M. and X.L.; project administration, L.M. and X.L.; funding acquisition, X.K. All authors have read and agreed to the published version of the manuscript.

Appendix A

Table A1. The parameters in the 5-MW VSWT system.

Parameter	Symbol	Value
Number of blades	-	3
Rotor radius	-	63 m
Hub height	-	84.3 m
Hub inertia on the low-speed shaft	J_H	115,926 kg·m^2
Blade inertia on the low-speed shaft	J_B	11,776,047 kg·m^2
Generator inertia on high-speed shaft	J_g	534.116 kg·m^2
Equivalent drive shaft torsion spring	K_θ	867,637,000 N·m/rad
Equivalent drive shaft torsion damping	B_θ	6,215,000 N·m/(rad/s)
Gearbox ratio	N_g	97
tower fore-aft inertia	M_t	430,000 kg
tower damping	B_t	17,600 N·s/m
tower stiffness	K_t	1,770,000 N/m
Air density	ρ_a	1.2231 kg/m^3
Rotor radius	R_r	63 m
Generator efficiency	η_g	94.4%

Table A2. The values of the bounds in the 5-MW VSWT system.

Parameter	Symbol	Value
Rated generator speed, Min. generator speed	$\omega_{g\ rated}, \omega_{g\ min}$	122.9096, 70.1622
Rated rotor speed, Min. rotor speed	$\omega_{r\ rated}, \omega_{r\ cut-in}$	1.2671, 0.7226
Min. shaft torsion angle	θ_{min}	0
Rated torque, Min. torque	$T_{g\ rated}, T_{g\ min}$	43,093.55, 0
Max. torque rate, Min. pitch, Max. pitch	$\Delta T_{gmax}, \beta_{min}, \beta_{max}$	15,000, 0, 90
Max. pitch rate, Rated electrical power	$\Delta\beta_{min}, P^E_{rated}$	8, 5,000,000

References

1. Data, E.S.T. What is the proportion of China's global renewable energy power generation installed data in 2018? *Polaris Power Network: Polaris Power Network News*, 12 April 2019. Available online: http://news.bjx.com.cn/html/20190412/974382.shtml (accessed on 2 May 2019).

2.   Bossanyi, E.A. Wind Turbine Control for Load Reduction. *Wind Energy* **2003**, *6*, 229–244. [CrossRef]

3.   Nam, Y. Control System Design. In *Wind Turbines*; IntechOpen: Rijeka, Croatia, 2011.

4.   Jafarnejadsani, H.; Pieper, J. Gain-Scheduled ℓ_1-Optimal Control of Variable-Speed-Variable-Pitch Wind Turbines. *IEEE Trans. Control Syst. Technol.* **2015**, *23*, 372–379. [CrossRef]

5.   Ren, Y.; Li, L.; Brindley, J.; Jiang, L. Nonlinear PI control for variable pitch wind turbine. *Control Eng. Pract.* **2016**, *50* (Suppl. C), 84–94. [CrossRef]

6.   El-Shafei, M.A.K.; El-Hawwary, M.I.; Emara, H.M. Implementation of fractional-order PID controller in an industrial distributed control system. In Proceedings of the 2017 14th International Multi-Conference on Systems, Signals & Devices (SSD), Marrakech, Morocco, 28–31 March 2017; pp. 713–718.

7.   Kusiak, A.; Zhang, Z.; Verma, A. Prediction, operations, and condition monitoring in wind energy. *Energy* **2013**, *60*, 1–12. [CrossRef]

8.   Yilmaz, A.S.; Özer, Z. Pitch angle control in wind turbines above the rated wind speed by multi-layer perceptron and radial basis function neural networks. *Expert Syst. Appl.* **2009**, *36*, 9767–9775. [CrossRef]

9.   Van, T.L.; Nguyen, T.H.; Lee, D.C. Advanced Pitch Angle Control Based on Fuzzy Logic for Variable-Speed Wind Turbine Systems. *IEEE Trans. Energy Convers.* **2015**, *30*, 578–587. [CrossRef]

10. Wakui, T.; Yoshimura, M.; Yokoyama, R. Multiple-feedback control of power output and platform pitching motion for a floating offshore wind turbine-generator system. *Energy* **2017**, *141*, 563–578. [CrossRef]

11. Jiao, X.; Meng, W.; Yang, Q.; Fu, L.; Chen, Q. Adaptive Continuous Neural Pitch Angle Control for Variable-Speed Wind Turbines. *Asian J. Control* **2019**, *21*. [CrossRef]

12. Moodi, H.; Bustan, D. Wind turbine control using T-S systems with nonlinear consequent parts. *Energy* **2019**, *172*, 922–931. [CrossRef]

13. Lio, W.H.; Rossiter, J.; Jones, B.L. A review on applications of model predictive control to wind turbines. In Proceedings of the 2014 UKACC International Conference on Control (CONTROL), Loughborough, UK, 9–11 July 2014; pp. 673–678.

14. Henriksen, L.C. *Model Predictive Control of Wind Turbines*; DTU Informatics: Lyngby, Denmark, 2010.

15. Henriksen, L.C.; Hansen, M.H.; Poulsen, N.K. Wind turbine control with constraint handling: A model predictive control approach. *IET Control Theory Appl.* **2012**, *6*, 1722–1734. [CrossRef]

16. Bououden, S.; Chadli, M.; Filali, S.; El Hajjaji, A. Fuzzy model based multivariable predictive control of a variable speed wind turbine: LMI approach. *Renew. Energy* **2012**, *37*, 434–439. [CrossRef]

17. Abdelbaky, M.A.; Liu, X.; Jiang, D. Design and implementation of partial offline fuzzy model-predictive pitch controller for large-scale wind-turbines. *Renew. Energy* **2020**, *145*, 981–996. [CrossRef]

18. Abdelbaky, M.A.; Liu, X.; Kong, X. Wind Turbines Pitch Controller using Constrained Fuzzy-Receding Horizon Control. In Proceedings of the 2019 Chinese Control And Decision Conference (CCDC), Nanchang, China, 3–5 June 2019; pp. 236–241.

19. Gros, S.; Vukov, M.; Diehl, M. A real-time MHE and NMPC scheme for wind turbine control. In Proceedings of the 52nd IEEE Conference on Decision and Control, Florence, Italy, 10–13 December 2013; pp. 1007–1012.

20. Soliman, M.; Malik, O.P.; Westwick, D.T. Multiple model multiple-input multiple-output predictive control for variable speed variable pitch wind energy conversion systems. *IET Renew. Power Gener.* **2011**, *5*, 124–136. [CrossRef]

21. Song, D.; Yang, J.; Dong, M.; Joo, Y.H. Model predictive control with finite control set for variable-speed wind turbines. *Energy* **2017**, *126*, 564–572. [CrossRef]

22. Rawlings, J.B.; Mayne, D.Q. *Model Predictive Control: Theory and Design*; Nob Hill Publishing: Madison, WI, USA, 2009.

23. Diehl, M.; Amrit, R.; Rawlings, J.B. A Lyapunov Function for Economic Optimizing Model Predictive Control. *IEEE Trans. Autom. Control* **2011**, *56*, 703–707. [CrossRef]

24. Heidarinejad, M.; Liu, J.; Christofides, P.D. Economic model predictive control of nonlinear process systems using Lyapunov techniques. *AIChE J.* **2012**, *58*, 855–870. [CrossRef]

25. Gros, S.; Schild, A. Real-time economic nonlinear model predictive control for wind turbine control. *Int. J. Control* **2017**, *90*, 2799–2812. [CrossRef]

26. Cui, J.; Liu, S.; Liu, J.; Liu, X. A Comparative Study of MPC and Economic MPC of Wind Energy Conversion Systems. *Energies* **2018**, *11*, 3127. [CrossRef]

27. Munteanu, I.; Bratcu, A.I.; Cutululis, N.-A.; Ceanga, E. *Optimal Control of Wind Energy Systems: Towards a Global Approach*; Springer Science & Business Media: New York, NY, USA, 2008.

28. Usta, I.; Arik, I.; Yenilmez, I.; Kantar, Y.M. A new estimation approach based on moments for estimating Weibull parameters in wind power applications. *Energy Convers. Manag.* **2018**, *164*, 570–578. [CrossRef]
29. Bianchi, F.; De Battista, H.; Mantz, R.J. *Wind Turbine Control Systems: Principles, Modelling and Gain Scheduling Design*; Springer: London, UK, 2007; p. 208.
30. Imran, R.; Hussain, D.; Chowdhry, B. Parameterized Disturbance Observer Based Controller to Reduce Cyclic Loads of Wind Turbine. *Energies* **2018**, *11*, 1296. [CrossRef]
31. Hur, S.-H. Modelling and control of a wind turbine and farm. *Energy* **2018**, *156*, 360–370. [CrossRef]
32. Jonkman, J.; Butterfield, S.; Musial, W.; Scott, G. *Definition of a 5-MW Reference Wind Turbine for Offshore System Development*; National Renewable Energy Laboratory (NREL): Golden, CO, USA, 2009.
33. Wächter, A.; Biegler, L.T. On the implementation of an interior-point filter line-search algorithm for large-scale nonlinear programming. *Math. Program.* **2006**, *106*, 25–57. [CrossRef]
34. Jonkman, J.M.; Buhl, M.L., Jr. *FAST User's Guide-Updated August 2005*; National Renewable Energy Laboratory (NREL): Golden, CO, USA, 2005.

Study of Floating Wind Turbine with Modified Tension Leg Platform Placed in Regular Waves

Juhun Song and Hee-Chang Lim *

School of Mechanical Engineering, Pusan National University, 2, Busandaehak-ro 63beon-gil, Geumjeong-gu, Busan 46241, Korea; ralph366@nate.com
*   Correspondence: hclim@pusan.ac.kr; Tel.: +82-515-102-302; Fax: +82-515-125-236

Abstract: In this study, the typical ocean environment was simulated with the aim to investigate the dynamic response under various environmental conditions of a Tension Leg Platform (TLP) type floating offshore wind turbine system. By applying Froude scaling, a scale model with a scale of 1:200 was designed and model experiments were carried out in a lab-scale wave flume that generated regular periodic waves by means of a piston-type wave generator while a wave absorber dissipated wave energy on the other side of the channel. The model was designed and manufactured based on the standard prototype of the National Renewable Energy Laboratory (NREL) 5 MW offshore wind turbine. In the first half of the study, the motion and structural responses for operational wave conditions of the North Sea near Scotland were considered to investigate the performance of a traditional TLP floating wind turbine compared with that of a newly designed TLP with added mooring lines. The new mooring lines were attached with the objective of increasing the horizontal stiffness of the system and thereby reducing the dominant motion of the TLP platform (i.e., the surge motion). The results of surge translational motions were obtained both in the frequency domain, using the response amplitude operator (RAO), and in the time domain, using the omega arithmetic method for the relative velocity. The results obtained show that our suggested concept improves the stability of the platform and reduces the overall motion of the system in all degrees-of-freedom. Moreover, the modified design was verified to enable operation in extreme wave conditions based on real data for a 100-year return period of the Northern Sea of California. The loads applied by the waves on the structure were also measured experimentally using modified Morison equation—the formula most frequently used to estimate wave-induced forces on offshore floating structures. The corresponding results obtained show that the wave loads applied on the new design TLP had less amplitude than the initial model and confirmed the significant contribution of the mooring lines in improving the performance of the system.

Keywords: floating offshore wind turbine; modified Morison equation; omega arithmetic method; tension leg platform; hydrodynamic motion response

1. Introduction

Offshore wind turbines generate more electricity than their onshore counterparts owing to higher wind speeds occasioned by the low surface roughness of the ocean. Due to increased interest in the design of offshore wind farms, the foundation of traditional fixed-bottom offshore wind turbines has been changing to the prolific floating type, which may be more feasible and less expensive for deep water. The diversity in the specifications of each floating platform type and the fact that wind turbines encounter a variety of wind, current, and wave loading at sea have resulted in active research into the dynamic response of offshore floating wind turbine support systems under various conditions with a view to ensuring security and reliability.

Jonkman et al. [1] provided the characteristics and specifications of the National Renewable Energy Laboratory (NREL) 5 MW offshore wind turbine, which is now considered the baseline wind turbine. This model has been mounted on various types of floating platforms and studies conducted on each structure. Wayman and Scalavonous [2] conducted comparative static and dynamic analyses of a Tension Leg Platform (TLP) FOWT and a shallow drafted barge FOWT to explore the effects of water depth, wind speed, and combined wind–wave conditions on system performance. In their study, they evaluated the response amplitude operator (RAO) standard deviation of the system in order to define the natural frequency at each degree of freedom. Lee [3] investigated the dynamic response of a spar buoy wind turbine by defining the nacelle acceleration, dynamic tensions on catenaries, and maximum tension acting on the anchors based on an extreme sea state condition for a 100-year return period. Lee showed that as water depth decreases the dynamic performance of the system becomes more challenging. Naqvi [4] performed experiments using a 1:100 scale TLP and spar buoy derived from the NREL prototype to study the motion and tension in the cables in response to regular waves and operational wind speed.

Hong et al. [5] utilized a 1:100 spar buoy to analyze the effects of center of gravity, mooring line tension, and fairlead location on the translational and rotational deviations of the system in response to regular waves. Most of the previous studies in this area were concentrated on analyzing the behavior of the platform under various environmental conditions. However, several studies were conducted in which either the best features of the platforms were combined or a new design was developed in order to increase the performance of the structure and minimize the drawbacks of each platform in a manner that enhanced the structural stability of the system to satisfactorily withstand all the environmental loads. Withee [6] studied the coupled dynamic analysis of a floating wind turbine system that combined the best features of both the TLP and the spar buoy with the objective of dampening the pitch and roll and reducing the loads on the structure. In the study, all modes of motion and the tether forces were investigated experimentally and numerically for a range of operational as well as severe wave and wind conditions. Murray et al. [7] proposed a 1:92 model of an extended TLP for deployment at a water depth of 1500 m and investigated its corresponding extreme responses, tether tensions, and platform deviations.

Karimirad and Moan [8] subsequently analyzed a spar-type offshore wind turbine with two distinct mooring systems under operating and survival conditions and focused on their stochastic dynamic motion and structural responses. The first concept was a catenary-moored spar wind turbine that used a taut system instead of the catenary mooring lines normally used for the spar buoy, while the second design was a spar with a tension leg mooring. The latter design consisted of a spar platform mounted in a single pre-tensioned mooring line. Experiments were carried out on the effect of hydrodynamic damping and the extreme structural responses under intense environmental conditions to examine the wind–wave-induced and wave-induced responses on the two mooring model concepts. Nianxin et al. [9] carried out experiments on a 1:60 TLP model to investigate the performance of the floating wind turbine in a coupled wind–wave environment. The model was derived from another prototype of TLP and additional catenaries were attached to it. The platform motion in surge, sway, and heave, as well as the tether forces, were investigated. Martinez et al. [10] studied the feasibility of a semi-floating spar buoy wind turbine attached to mooring lines strongly anchored to the bed with a spherical joint, with the objective of reducing the oscillations of the system and thereby reducing the fatigue and maximum loads compared to the spar buoy turbine. Regarding the data modeling of sea height, there have been a series of measurements taken at the Northern Sea near Scotland (see Hadjihosseini et al. [11–13]). In addition, the approach to analyze the evolution of stochastic properties associated to the operation of wind turbines has been made, particularly in what concerns loads on the wind turbine (see Lind et al. [14,15]). Regarding the aeroelastic behavior, such as the case when the turbine is in power production the dynamic response, the behavior of wind turbine is completely different due to a significant increase of aerodynamic damping (see Marino et al. [16,17]). Regarding the improvements of Morison equation for steep waves and for diffraction regimes, there

have been some reference works (see Nielsen et al. [18]; Paulsen et al. [19]; Bredmose et al. [20]; Patel and Witz [21]).

In this study, the design of the traditional TLP floating platform derived from the NREL prototype and a conceptual TLP design with additional mooring lines were experimentally investigated. The additional mooring lines reinforce the horizontal stiffness of the system and thereby diminish the dominant motion, which is obviously the surge motion, to enable safe performance in deep water. In the study, a series of experiments were conducted using a 1:200 scale model to determine the impact of waves on the performance of the model. The range of operational and extreme waves used in the experiments was based on real data for a 100-year return period of the Northern Sea of California to ensure the feasibility of installing the new system in the chosen site. Another objective of this study was determination of the wave loads on the platform; this was achieved experimentally using the Morison equation.

Previous studies predominantly focused on measurement of the wave loads acting on a fixed-bottom offshore wind turbine. Peeringa [22] showed that an acceptable prediction of the wave loads for non-breaking waves is achievable by using the Morison equation and the stream function wave model. However, the hydrodynamic forces are underestimated by the applied methods in the case of breaking and post-breaking waves. Journee and Massie [23] and Sarpkay and Isaacson [24] proposed various methods to define the drag and inertia coefficients for better estimation of the solution to the Morison equation. Burrows et al. [25] also defined several techniques, such as least square, cross-spectral, and the methods of moments, to identify these coefficients, and subsequently measured the wave loads using the Morison equation to prove the accuracy of predicting random forces using the equation. The measured data were later shown to sufficiently match the predicted values, which confirmed the suitability of the equation for measuring wave loads. Henderson [26] subsequently enumerated several methods to determine wave load models and structural dynamics models depending not only on the turbine selected but also the support structure. The studies conducted revealed that the selection of a relevant approach for defining the resulting loads plays a fundamental role in the cost of the structure and its ability to resist environmental loads. Dean and Dalrymple [27] presented several methods to define appropriate wave kinematics theoretically or experimentally.

Considering the results of the above studies, in this study, the Morison equation was applied to measure the wave loading on the offshore wind turbine's TLP platform to verify its accuracy in predicting the wave loading on an offshore floating structure. The remainder of this paper is organized as follows: Section 2 describes the experimental setup used to perform the experiments on the scale model. An enumeration of the main properties of the model along with the laws that permit scaling it down and a sketch of the new design are also given, and the difficulties and errors dealt with while performing the experiments outlined. Section 3 provides a theoretical outline of all the governing equations used in our study in order to facilitate a thorough understanding of the physics underlying the phenomena under investigation. Section 4 analyzes, discusses, and interprets the data collected in the experiments. The data are associated with both the dynamic performance of the two concepts in response to regular and extreme waves and also the wave loading on the structure. Finally, Section 5 concludes by summarizing all the results obtained and outlines plans for further work.

2. Design of the Laboratory Experiment

Considering the dimensional restrictions imposed by the wave flume, the scale of the model was set at $\lambda_m/\lambda_p = 1{:}200$. The subscript "m" denotes the scale of the model and "p" the scale of the prototype (see Figure 1). Froude scaling was applied in order to establish scaling factors between the model and the full-scale prototype (Jonkman et al. [1]). The latter was derived from the NREL 5 MW wind turbine. In the flume experiment, the piston-type wave maker was used to generate a propagating wave more effectively because the horizontal water particle velocities of the wave and paddle are nearly constant over the water column. In the flume, a passive wave absorbers comprised

a hard filling material was installed in the channel. Based on the wave theory and reflectance, two wave gauges (KENEK, Wave height Meter CH-606) were used to take proper samples for a period, approximately 30 s (see more details in the papers of Lim [28] and Zhu and Lim [29]). To make reliable result, the experiment considered the effect of evanescent waves in the wave flume, which could contaminate test areas leading unexpected data. To avoid this effect, the model was placed around three times away from the wave maker. However, due to the size limitation of the wave flume, the influence of evanescent waves was not severe, but still remained (see Lim [28] and Zhu and Lim [29]).
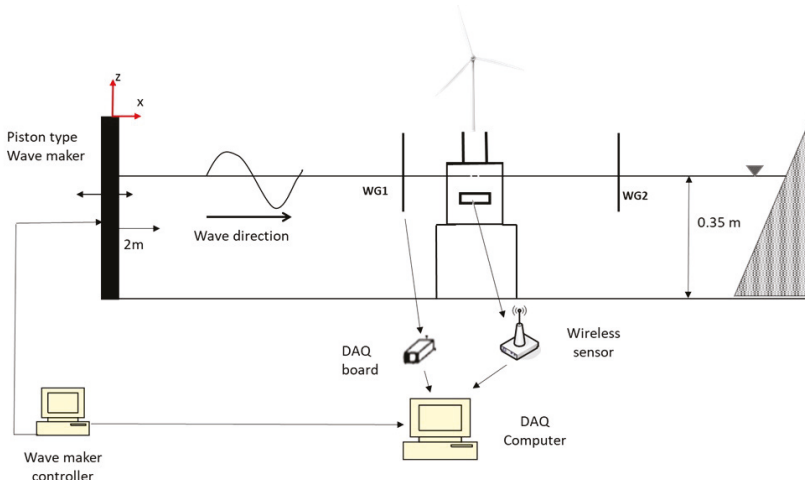

Figure 1. Measurement setup sketch.

The model was made from acrylic plastic; the design parameters for all the various dimensions, which were scaled according to Froude law, are listed in Table 1. The shape was identical to that of the prototype and the model surface was smooth in order to prevent deterioration of the surface over time and model deformations. However, scaling all the parameters precisely was difficult to achieve because of the large scale chosen for our study and the fact that we were primarily interested in the hydrodynamic motion of the platform. For these reasons, the aerodynamic properties of the wind turbine were not scaled, which means that the blades, rotor, and nacelle were not taken into consideration and only the height of the tower along with the overall mass of both the tower and the rotor nacelle assembly were matched with the real wind turbine parameters for the 5 MW wind turbine specifications (see Jonkman et al. [1]). In addition, for the TLP model, as proven previously, the larger is the length scale, the more dominant will be the scale effects, and the more complicated it will be to obtain identical ratios between the model and its prototype. Thus, the model was scaled more to the perfect weight than the perfect length in such a manner as not to impair the scaling of the moment of inertia of the system, which is a parameter that is directly proportional to both the length and the weight.

The modified concept developed in this study was actualized by connecting additional mooring catenaries to the system (see Figure 2). The catenaries were directly attached to the platform in the bottom surface in order to increase the horizontal stiffness and give more stability to the system. As shown in Figure 2, the rigid body, comprising the wind turbine and the floating support, undergoes oscillatory translational and rotational motions as a result of wind and wave loadings. Surge and sway (ξ_1 and ξ_2) describe horizontal motions along the x and y axes, respectively. The horizontal axes of the system were aligned with the four spokes to which the floater tethers were connected. Heave (ξ_3) represents the vertical motion of the floater. The oscillatory angular motions are referred to as the roll,

pitch, and yaw. The surge, sway, and yaw describe the three rigid-body motions. The tether lengths were assumed to remain constant during rigid-body motion.

Table 1. Main design parameters of the Tension-Leg Platform (TLP) model.

TLP Properties	Full Scale	Scale Ratio	Model
$\lambda = \frac{\text{fullscale}}{\text{model}} = 200$			
Diameter	22 m	λ	11 cm
Cylinder height	21.5 m	λ	10.75 cm
Concrete ballast height	4.5 m	λ	2.25 cm
Installed draft	20.01 m	λ	10 cm
Deck clearance	1.49 m	λ	1.5 cm
Steel thickness	0.01 m	$\sqrt{\lambda}$	0.2 cm
Concrete mass	4.345×10^6 kg	λ^3	455 g
Turbine mass	0.698×10^6 kg	λ^3	110 g
Buoyant mass	7.797×10^6 kg	λ^3	780 g
Total mass	5.249×10^6 kg	λ^3	715 g
Center of gravity	-9.4 m	λ	-4.5 cm
Center of buoyancy	-10.01 m	λ	-5 cm
Surge resonant period	15 s	$\sqrt{\lambda}$	1.1 s
Pitch resonant period	0.5 s	$\sqrt{\lambda}$	0.2 s
No. of tethers	4	-	4

Figure 3 illustrates the configuration of the modified TLP with the added inclined lines. Four small holes were drilled in the bottom surface of the cylinder and filled with glue. The steel wire ropes, containing a soft spring at each line, were then introduced into the holes and glue applied to make it harden. The combination of spring and steel wire resulted in a non-homogeneous model for modeling the axial stiffness and neglecting the bending stiffness (Bartrop [30]).
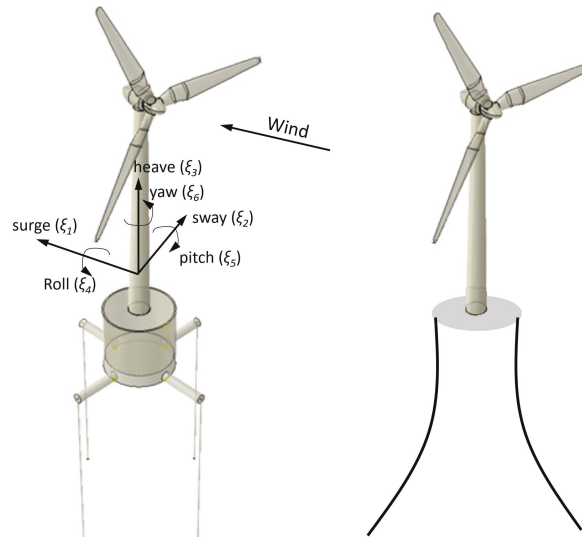

Figure 2. Sketch of TLP system (**left**); and catenary mooring system (**right**).
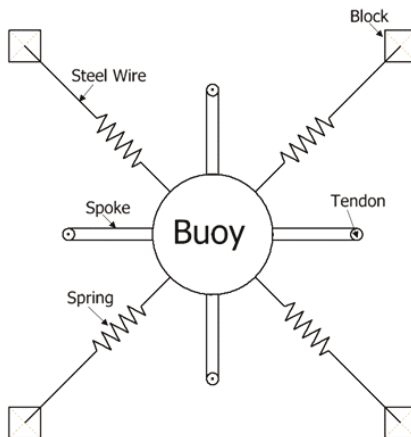
Figure 3. Modified tension leg configuration.

The scale model tests were then carried out in the wave flume of our laboratory. (see Table 2) On one side, the wave tank was fitted with a piston-type wave maker that generated regular monochromatic waves with different heights and periods. On the downstream section of the flume, a wave absorber was installed to dissipate wave energy and to avoid reflected waves inside the tank.

Table 2. Spoke and mooring lines design parameters.

Parameter	Full Scale	Model
Spoke	Length = 14 m Diameter = 3 m	Length = 17 cm Diameter = 1.5 cm
Tension leg	Length = 46 m Diameter = 0.48 m Fairlead location = 24 m Pretension = 2.3×10^4 N	Length = 23 cm Diameter = 0.2 m Fairlead location = 12 cm Pretension = 2.3015 N
New tethers	Length = 60 m Diameter = 0.48 m - -	Length = 30 cm Diameter = 0.2 mm Spring stiffness = 1.471 N/mm Maximum load = 23.2 N

The response of the TLP model to the wave loading was then studied through a sensor via a wireless data acquisition system, which eliminated the need for cables that would otherwise affect the platform motions and hence the experimental results. The sensor used in the experiments was placed inside the cylinder of the model's platform; it facilitated the measurement of six degrees-of-freedom deviations simultaneously. The waves generated by the wave maker were recorded using the wave gauge placed upstream of the model, and the depth of water in the flume was kept constant. The order of the test wave amplitudes was varied from 0 to 40 mm with a test wave period from 0.4 to 2 s. The experimental data were recorded and controlled using National Instruments LabVIEW software.

3. Theoretical Approach

3.1. Equation of Motion

An offshore wind turbine mounted on a TLP undergoes six degrees-of-freedom motion forming three rigid body translational motions and three rotational motions. When it is excited by waves, the assumption based on the linear hydrodynamic analysis and a linear damping allows the motion

equations for surge, heave, pitch, and yaw to be solved in the frequency domain. Sway and roll are identical to surge and pitch, thus are not treated here. It was also assumed that no waves are generated by the floater, since the wavelengths of the ambient waves were assumed to be much greater than the floater diameter. The wave–floater interaction problem can therefore be solved in a simplified manner. The governing equation describing the balancing of the exciting forces for the surge behavior is derived from Newton's second law (see Withee [6]), and is stated as follows:

$$\begin{bmatrix} M_{11} + A_{11} & A_{15} \\ M_{51} & M_{55} + A_{55} \end{bmatrix} \begin{bmatrix} \ddot{\zeta}_1 \\ \ddot{\zeta}_5 \end{bmatrix} + \begin{bmatrix} B_{11} & B_{15} \\ B_{51} & B_{55} \end{bmatrix} \begin{bmatrix} \dot{\zeta}_1 \\ \dot{\zeta}_5 \end{bmatrix} + \begin{bmatrix} C_{11} & C_{15} \\ C_{51} & C_{55} \end{bmatrix} \begin{bmatrix} \dot{\zeta}_1 \\ \dot{\zeta}_5 \end{bmatrix} = \begin{bmatrix} F_1(t) \\ F_5(t) \end{bmatrix} \quad (1)$$

and the uncoupled heave and yaw equations of motion are:

$$(M_{33} + A_{33})\,\ddot{\zeta}_3 + (B_{33})\,\dot{\zeta}_3 + C_{33}\zeta_3 = F_3(t)$$
$$(M_{66} + A_{66})\,\ddot{\zeta}_6 + (B_{66})\,\dot{\zeta}_6 + C_{66}\zeta_6 = F_6(t) \quad (2)$$

where M_{jk} are the components of the mass matrix of the system; B_{jk} and A_{jk} are the frequency-dependent damping and added mass coefficients, respectively; F_j are the external exciting forces due to waves; and C_{jk} are the hydrostatic restoring coefficients.

The term $\ddot{\zeta}$ represents the dimensional acceleration of the system in each mode of motion at each frequency, $\dot{\zeta}$ is the system's velocity in each mode, and ζ is the system's displacement. The solution to these coefficients is fundamental for solving the equation of motion; a solution procedure was described in detail by Withee [6], with the assumption that the restoring is achieved by a stiff mooring tether that limits any significant motion in pitch and drives the restoring in pitch toward infinity (Wayman and Sclavonous [2]). The eigenvalues of this equation give the natural frequencies for the modes of motion in this study.

In order for the system to be analyzed using linear frequency domain analysis, all of the linear quantities must be analyzed relative to the wave elevation:

$$\eta(t) = Re(Ae^{-ik(x\cos\beta + y\sin\beta)}e^{i\omega t}) \quad (3)$$

where A is the wave amplitude. The linear wave excitation forces f_i acting on the platform are defined relative to the local coordinate system (x, y, z) and by virtue of linearity adopt the complex representation:

$$f_i = Re(A \cdot X_i e^{i\omega t}), \quad i = 1, ..., 6 \quad (4)$$

where X_i is the complex amplitude of the exciting force or moment in the i-direction. The platform motions ζ_i in the six degrees of freedom also adopt the complex representation:

$$\zeta_i = Re(A \cdot \Xi_i e^{i\omega t}), \quad i = 1, ..., 6 \quad (5)$$

where Ξ_i is the complex response amplitude for the platform in the j-direction (i.e., RAO).

The water particle components are essential in defining the wave-induced forces on floating structures. Therefore, the Airy wave theory, often called the linear wave theory, was used to predict the horizontal water velocity and acceleration where the cylinder is located (Dean and Dalrymple [27]).

3.2. Modified Morison Equation

In deep water, the waves are assumed to have a low steepness (small wave height compared to wavelength). This enabled us to use the Airy linear wave theory. This latter assumption and the assumption that the waves are unidirectional are considered basic assumptions for the use of the Morison equation for calculating the wave loading on offshore structures.

A simple equation was developed by Morison for calculating the wave loads on floating submerged structures in water. The equation is stated as follows:

$$dF = \frac{\rho \pi D^2}{4}\dot{U} + \frac{\rho \pi D^2}{4}C_a(\dot{U} - \dot{V}) + \frac{\rho D}{2}C_D \left| U - V \right| (U - V) \tag{6}$$

where dF is total wave force; U and $\dot{U}$ are fluid velocity and acceleration, respectively; V and $\dot{V}$ are the relative velocity and acceleration of the floating structure; C_a and C_D are the added-mass and drag coefficient; ρ is density; and D is the cylinder diameter. The first two terms on the right side of the equation represent the inertia forces, while the last term determines the drag forces on the platform. The inertia forces comprise the Froude–Krylov force and the hydrodynamic mass force.

4. Results and Analysis

The scale floating wind turbine model was experimentally tested against a series of regular waves generated by the wave maker to obtain the dynamic response of the system in the six degrees of freedom. Regular wave parameters were chosen based on historical wave data for the North Sea near Scotland, where it was assumed that the offshore TLP wind turbine will operate.

4.1. Surge Dynamic Analysis of the TLP in Response to Regular Wave

All the physical structures including the floaters displayed natural frequencies in their motion. It is well known that a structure tends to oscillate at this frequency when stimulated by external forces. Under resonance conditions, a small force applied at this frequency produces a large oscillatory response. Thus, a dynamic force applied to a physical object causes it to vibrate. It is therefore important to know, on the one hand, the natural frequencies within a system and, on the other hand, the frequencies at which excitation is likely to occur to ensure that they do not coincide. It is generally not possible to control excitation frequencies of excitation, but the natural frequency of a system—which depends on physical characteristics such as mass and stiffness—can be altered.

When the TLP model is subjected to regular waves, the mooring lines may help to reduce the rotational motion around the three axes, even though they were mainly designed to reduce the surge acceleration and displacement. Incoming regular waves were assumed to be uniform and incident on the platform in the surge direction and a wave with an amplitude of approximately 12 mm and a wave period of T = 0.8 s was chosen for this experiment. Figure 4 shows the temporal variation of surge acceleration for the initial TLP and modified TLP concepts, while the corresponding surge amplitude spectrum comparison of the initial and modified concepts after applying Fast Fourier Transform (FFT) to the signal's temporal variation is given in Figure 5.
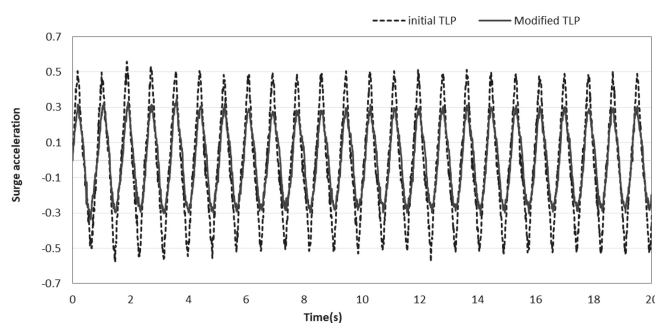

Figure 4. Time domain surge acceleration comparison for new and initial TLP concept.

As shown in Figures 4 and 5, the amplitude of the surge acceleration decreased as a result of addition of the mooring lines. This indicates that the new configuration contributes significantly to enable effective damping of the surge motion compared to the vertical tendons only, and hence improves the performance of the platform under wave attack. In addition, the spectra display well-defined peaks because of the periodic harmonic motion displayed in the time domain, even though the spectrum of the initial model appears to be noisier than that of the modified TLP for the same wave frequency. There are a couple of reasons to explain the improvement. One would be larger amplitude motion in the initial model, and the other an additional mooring line in modified TLP configuration; nevertheless, the peaks remain well defined in both cases. These findings confirm that the modified concept helps to stabilize the system's motion, which is essential to improving the performance of the wind turbine, because reducing the motion positively affects power production and turbine structural loading. In other words, platform motion causes larger inertial loads on the entire structure, which potentially leads to reduced efficiency and increased fatigue loading. Furthermore, the tether pretension also plays a fundamental role in the stability of the system. This also explains why the modified TLP with its higher initial pretension is more stable than the initial four-legged TLP. The new tethers were inclined, instead of being straight, in order that they not exceed the operational range of the tether's pretension.
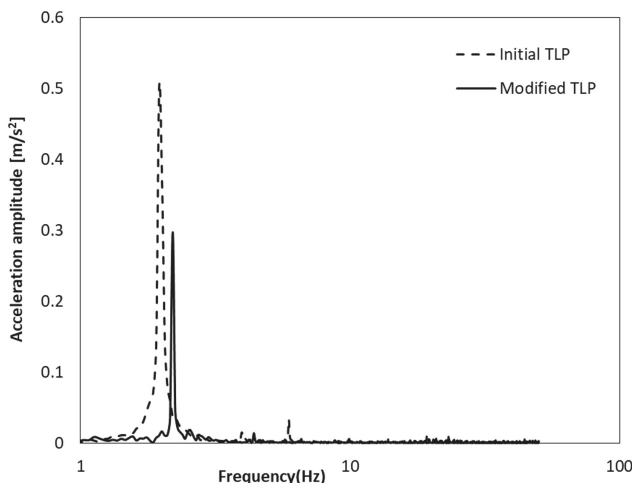

Figure 5. Surge spectrum for initial and modified TLP concept.

4.2. RAO Analysis for Regular Wave Tests

In this study, the water depth was kept constant at 35 cm in the wave flume, and a series of regular wave tests was carried out on both the initial model and the new design. This was done to validate previous results and to study the natural period and natural frequency of the new model compared to the initial one using the RAO method. The RAO is defined as the non-dimensional ratio of the surge to the surface elevation, which is used to analyze the dynamic motion of floating structures.

Figure 6 shows the RAOs for the NREL TLP, the modified TLP, and a numerical simulation of the same prototype (i.e., modified TLP) developed by Nematbakhsh [31]. For the translational accelerations (surge, sway, and heave), the RAO is determined by

$$RAO_{acc}(w) = \left| \frac{\sqrt{S_R(f)}}{\sqrt{S_I(f) * (2\pi f)^2}} \right| \tag{7}$$

where $S_R(f)$ represents the dimensional response of the structure in each mode of motion in the frequency domain and $S_I(f)$ is the wave power spectral density. As shown in the figure, both the initial TLP and the new design have the same trend with a slight decrease in the surge RAO response. However, the natural frequency, defined graphically as the frequency at which the peak occurs, was slightly shifted to a higher frequency for the new design but remained smaller than 0.4 rad/s. In addition, it was considered as the operational natural wave condition for FOWT, which is defined by ITTC spectrum for different sea states and provides a significant wave height of 5.0 m and a modal period of 12.4 s (see Kim and Hong [32]). On top of this condition, the water flume was only operated by a wave generator so that it was purely affected by the wave loading because wind tunnel was not turned on. On the other hand, the reference data of numerical simulation were also based on the nonlinear hydrodynamic forces on the platform, while wind speed was assumed constant. Therefore, the natural frequency can be inferred from the surge RAO response of the test model itself exerted by the wave loading. Consequently, both concepts can operate safely in the chosen site. Furthermore, to validate the results, the experimental surge RAO data were compared to the numerical representation. This latter was performed for a range of wave periods, from 0.6 to 1.2 s. The results obtained show that, for the same range of wave frequencies, a good similarity was found between the numerical and experimental data as the RAO motion increases while moving close to the natural frequency. It was expected that the peak in the numerical model would occur within the same range of wave frequency since the natural frequency in surge was defined to be 15 s.
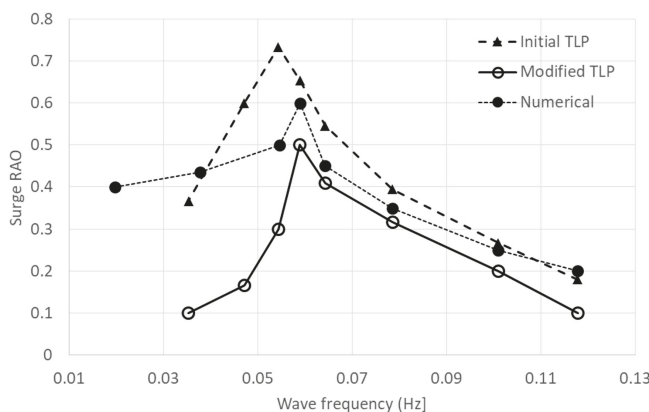

Figure 6. The surge RAO comparison for the two concepts.

4.3. Water Depth Effect

Considering that offshore wind turbines are suited to operate in rated power case as well as in deep water, the effect of water depth was investigated and experiments conducted to ensure the capability of the modified concept TLP to operate in deep water. Figure 7 compares the surge RAO's response in two different water depths for the TLP with the additional cables.

As shown in Figure 7, the RAO shows that the motion of the platform decreases with increasing water depth, which confirms that the TLP is a suitable structure for deep water. On the other hand, the natural frequency of the system was shifted to lower frequency in the case of the TLP with additional mooring cables in greater water depth. This was achieved as a result of the increase in the length of the tendons and the added mooring lines when operating in deeper water. The increase in the length of the tethers and the added mooring lines influenced the amplitude motion as well as the natural frequency, and they enabled an acceptable restoration in the surge of the system reducing the natural frequency. The same results were obtained by Wayman and Sclavonous [2], who investigated

the water depth effect for an NREL TLP. Those results and the results of this actual study are in good agreement as both studies indicate that the water depth not only contributes to reduce the motion but also lowers the natural frequency. Thus, it is possible to tune the tether stiffness of a system to match a certain experimental natural frequency by means of restoring.
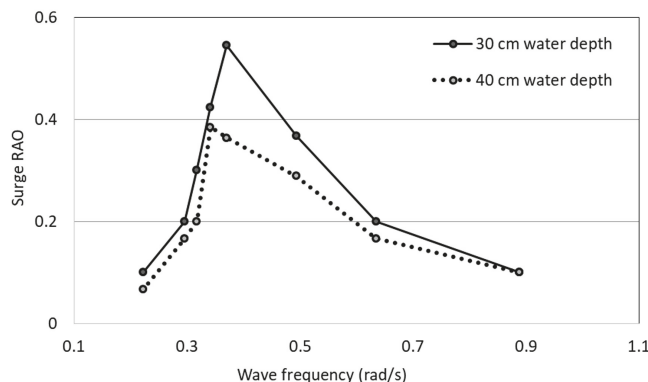

Figure 7. The water depth effect on the motion of the modified TLP with cables.

4.4. Wave Loading Using Morison Equation for Regular Waves

The wave loads were calculated using the Morison equation. The experimental values obtained for the initial TLP were then compared to those for the TLP with the additional cables. The experimental conditions were similar for both cases and the same wave height and wave period were applied in the case of a regular wave test.

4.4.1. Omega Arithmetic Method for Relative Velocity

One of the requirements of the Morison equation for predicting wave loading in floating structures is the definition of the relative velocity of the system while being subjected to the action of the incoming waves. The relative velocity was integrated from the acceleration data using the omega arithmetic method, which is considered to be the best method for the integration to convert acceleration into velocity (see Appendix A for omega arithmetic code).

As shown in Figure 8, the relative velocity is represented after being integrated from the acceleration data using the omega arithmetic method outlined above. The method determines the corresponding velocity from an acceleration dataset without going through the formal integration in time. Meanwhile, this method is obviously influenced by the frequency behavior of the signal, as the conversion process was carried out in the frequency domain rather the time domain signal. In other words, the time series were converted to the frequency domain using FFT, integrated by dividing by ω, and then converted back to the time domain using the inverse FFT. Thus, this procedure is the most accurate for the conversion process because neither the time domain integration nor the application of a high pass filter before performing the integration was a good solution for integrating the relative velocity in this case.

Because the acceleration motion response is a harmonic function, the velocity has a sinusoidal variation, but it is not in phase. The phase relationship between acceleration and velocity is such that the velocity is 90° out of phase with acceleration. This is noticeable from the figures; when the structure passed through the equilibrium position, the velocity was at its maximum and the acceleration was zero.
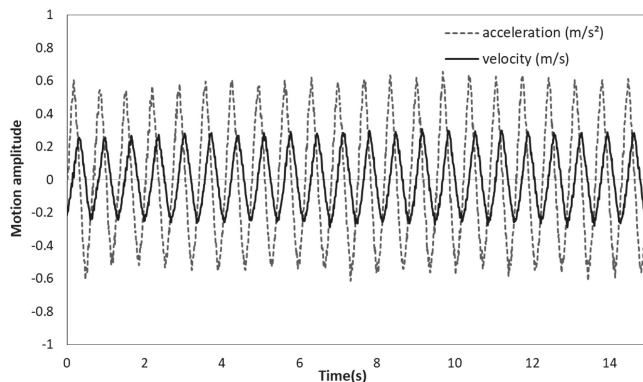
Figure 8. The time domain for surge acceleration and velocity of the initial TLP.

Figure 9 compares the relative velocity of the TLP with tendons only and the modified concept with additional mooring lines attached. It shows that the magnitude of the velocity was smaller in the new model than in the prototype. The results confirm the findings that the mooring lines helped to reduce not only the surge acceleration but also the velocity of the structure when it was subjected to monochromatic regular waves.
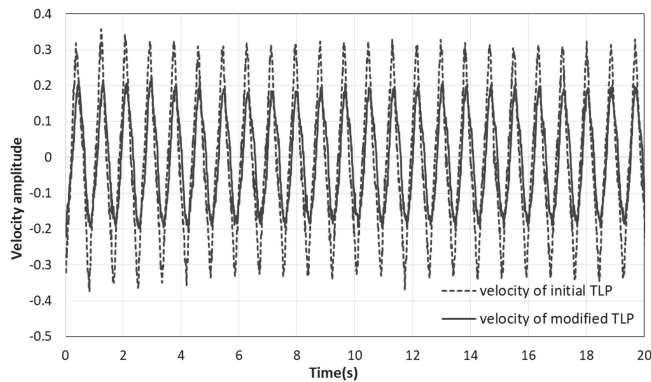

Figure 9. Time domain surge velocity comparison for new and initial TLP concept.

4.4.2. Wave Loading Results

The water particle kinematics in the case of a regular wave can be defined on the basis of the extrapolated Airy wave theory. The Airy theory was used because of its suitability for a wide range of waves at any site, including extreme and fatigue cases. However, it has a drawback in that it does not consider the peaks and troughs of waves. Conversely, the extrapolated Airy theory, known as the wheeler stretching method, makes the original theory more flexible by calculating the kinematics both at the mean water level and at the water elevation surface, which results in a kinematics prediction that is closer to reality.

Numerous methods also exist for defining the inertia and drag coefficients. The results published by the DNV (Det Norske Veritas) are widely accepted (Journee and Massie [23]). The DNV has calculated coefficients for different types of cylinders based on their roughness with respect to the KC

(Keulegan–Carpenter) number because of the primary dependence of the coefficients on the number. The KC number is expressed by the following equation (which is valid for the deep-water studies):

$$KC = UT/D = \pi H/D \tag{8}$$

where U is the water particle velocity, T is the wave period, D is the cylinder diameter, and H is the wave height. Based on the DNV report, the inertia coefficient of a smooth floating cylindrical platform is related to the added mass coefficient by the following relation:

$$C_M = 1 + C_a \tag{9}$$

where $C_a = 1$ in the case of a circular cylinder. This leads to an inertia coefficient with an approximate value of two and a drag coefficient close to one for low KC numbers, as is the case in this study where the inertia forces are dominant and the drag forces are not important. In this study, to get both coefficients, the Morison's method was applied (see Journee and Massie [23]). This method is based on the measured force (N), velocity (m/s) and acceleration (m/s^2) from the flume experiment. Given that the fundamental data were provided, the Morison equation can be decomposed into two parts: inertia and drag terms. Therefore, based on the Morison's method, the drag coefficient can be obtained while making the relative acceleration becomes zero, whereas the inertia coefficients can also be calculated while having relative velocity zero. More details are also well described in the paper (see Wolfram and Naghipour [33]).

From the results for operational range, it is clear that the forces caused by the interaction between the cylinder and the waves on the new design are less than those on the initial model (see Figure 10). This confirms that the new mooring lines not only contribute to a stable system but also results in lower load on the platform. Moreover, the horizontal component of the total force per unit length has a harmonic shape because of the accelerating and decelerating movements in the body motion, which imply a change in the kinetic energy of the fluid within the control volume. Furthermore, the unstable drag and inertia coefficients also have an effect on the forces as they depend primarily on the KC number, which in turn depends on the velocity of the fluid. As a result, the better estimation of the water kinematics enabled the Morison equation to be more accurate in predicting the wave loading on the TLP's cylinder. It is also notable that the loads have a nonzero mean value. This offset may be explained by the excess buoyancy and the pretension on the tether, which requires that the cylinder support some of the load in order to keep the system sufficiently balanced. This is because the pretension of the tethers is related to the buoyancy force and the overall mass of the system times the gravitational acceleration.
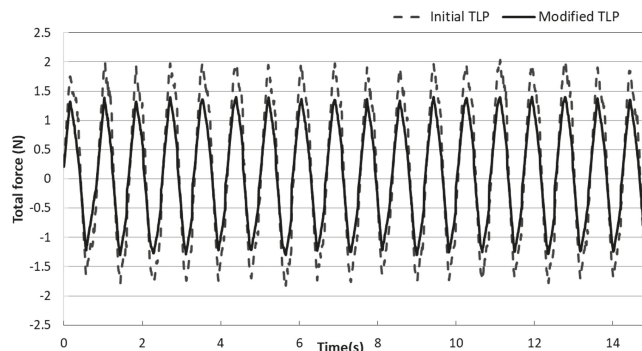

Figure 10. Experimental wave loads comparison in a regular wave.

4.5. Extreme Design Sea Condition Analysis

The ability of the new system with added mooring lines to withstand extreme sea conditions in Northern sea of California was verified. This verification was performed with the objective of ensuring that the new design can operate in a severe sea state, which makes it suitable for both regular and extreme sea states. The extreme sea conditions were issued by the Center for Offshore Safety, USA, and the parameters of the waves were chosen based on their report (Berg [34]). The chosen wave amplitude was 5 cm with a wave period of 1.2 s based on the scale ratio of 1:200 used in this study.

As shown in Figures 11 and 12, the surge acceleration remained the most obvious of the three translational motions with a larger amplitude than regular waves because of the severe sea state. However, the extreme design case caused the platform to have significant motion in the sway direction, which cannot be neglected as in the case of the regular wave, because of the substantial contribution of the mooring lines in effectively damping all the other rigid body and rotational motions. In addition, the ability of the system to respond was demonstrated and it was also shown that severe wave conditions tend to increase the motion amplitude of the modified TLP above the regular and operational range. However, this amplitude remained in the acceptable range where a structure can ensure its operability without affecting the performance of the installed wind turbine.
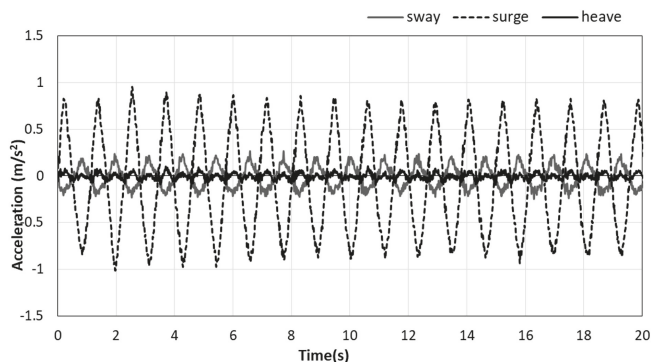

Figure 11. Translational accelerations in extreme design condition for modified TLP.
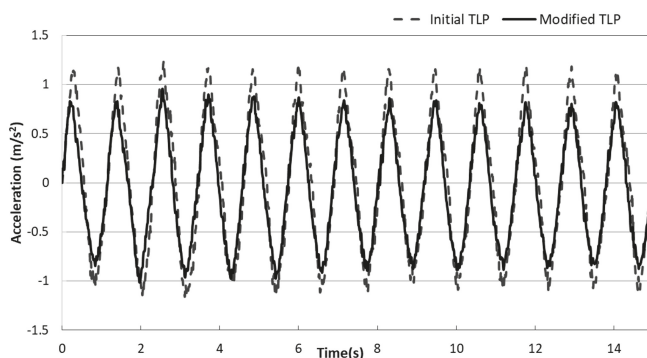

Figure 12. Surge acceleration comparison for both concepts in extreme design case.

As shown in Figure 13, the surge amplitude spectra derived from the time domain using the FFT, which defines a comparison between the surge acceleration in the extreme conditions of the two concepts, confirmed the mooring lines contribution in damping the surge motion even in extreme conditions. However, because the exhibited motion had a larger amplitude, the spectra appeared noisier than in the regular case, but the peaks were still well defined. Another aspect of concern is the loads applied to the structure in the extreme wave event. It was expected that the wave would have a significant impact on the structure in terms of loading, as it was proven that the added mass generated in the case of an extreme wave is higher owing to the high kinetic energy of the fluid around the structure, which causes an increase in both the body's motion and the water kinematics. Therefore, the loading on the system exerted a high tension on the tethers and the new mooring lines; however, this tension should remain within the safe range because an excess on the design value would result in the consequent destruction of the system. This means that the new model withstood the extreme design wave condition for a 100-year return period for the chosen site.
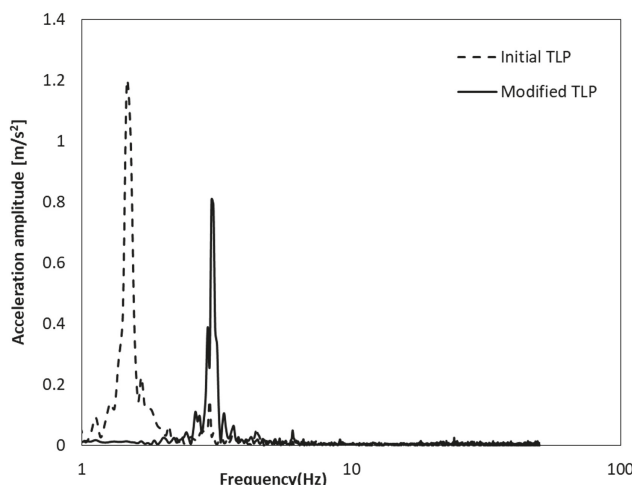

Figure 13. Initial and modified TLP's surge spectrum in extreme case.

The new findings in the behavior of the modified TLP under the onslaught of waves may play a fundamental role in providing better stability and thereby improve the overall performance of the system, especially in critical environmental loads. This is because the mooring lines tend to increase the stiffness, which contributes to the rigidity of the system, and the design life of offshore wind turbines may be enhanced as well.

5. Conclusions

A new tension leg platform conceptual design for offshore wind turbines was proposed with the objective of reducing the dominant surge motion of this kind of platform. The feasibility of the new model to operate under different wave conditions was also investigated. The design was proposed based on the NREL prototype and the wave conditions were chosen according to a report in the USA regarding the Northern Sea of California, where it is assumed that the new system will operate.

For the operational range of regular waves, the following can be stated:

- The modified concept model tends to decrease the velocity and acceleration of the overall system. A new method, known as the omega arithmetic method, which provides accurate and exact conversions, was introduced to integrate the displacement from the acceleration data.

- The RAO surge response proved that the two concepts avoid the natural wave frequency. This means that resonance is avoided, which is one of the main requirements for FOWT in order to operate in a safe environment. Furthermore, the water depth also has the same effect as the mooring lines, as it was proven that the motion amplitudes decrease with increasing water depth, which confirms that the new model is suitable for deep water.
- As regards extreme sea conditions for a return period of 100 years, the experimental results indicate that the motion amplitude will increase without exceeding the range of accelerations where the floating system is known to be able to operate safely. Further, the modified concept was verified to have smaller motion amplitude than the initial concept even in harsh environmental conditions.
- The loads applied on the structure by the waves were also measured using the Morison equation after matching all the conditions required for the use of the equation.
- The results obtained for the new model show that the addition of the mooring lines plays a positive role in reducing the wave loads compared to the initial model in the case of both regular and extreme waves.

These findings on the performance of the model under wave effect should be taken into account when constructing this kind of platform in the future. However, additional studies need to be conducted in order to investigate the coupled dynamic motion under all combined environmental loads combined with the tension on the tethers to enable optimization of the modified TLP system with additional lines. This would further improve the modified concept TLP system and help to effectively minimize the drawbacks to withstanding all environmental loads and increase the performance of offshore wind turbines. On top of these findings, the scaling issue would be one of the important considerations when the test data of scaled model match the full scale model. In particular, most measurements in the flume ertr made only on a small-scale model, which needs further investigation in the future.

Appendix A

Matlab code: omega arithmetic method for converting acceleration into velocity and displacement.

```
Fs=100; dt=1/Fs; et=15; t=0:dt:et;
y=xlsread('surge');
subplot(2,1,1); plot(t,y,'r');

xlabel('time(s)'); Y=fft(y); n=length(y); Amp=abs(Y)/n; NumuniquePts=ceil((n+1)/2);
freq=(0:NumuniquePts-1)*Fs/(n-1); freq2=-1*freq(end:-1:1);
if mod(n,2)==0
freq2(1)=[ ];
end
freq3=[freq,freq2];
freq3';
size(freq3)
```

```
if mod(n,2)==1
freq3(n+1)=[ ];
end
if mod(n,2)==0
freq3(n)=[ ]];
end
subplot(2,1,2); plot(freq,Amp(1:NumuniquePts),'b');
subplot(2,1,1); plot(freq,Amp(1:NumuniquePts),'b');
xlabel('frequency(hz)'); ylabel('amplitude');


B=reshape(Y,1,1501); G=B./(2*pi*freq3*1i);


G(1)=[1];
if mod(n,2)==0
G(n)=[1];
end
inversed=ifft(G);
plot(t,real(inversed),'b')
hold on
plot(t,y,'r')
title('omega arithmetic');
xlabel('time(s)');
ylabel('velocity blue,Accel red');
```

References

1. Jonkman, J.; Butterfield, S.; Musial, W.; Scott, G. *Definition of 5-MW Reference Wind Turbine for Offshore System Development*; Tech. Report NREL/TP-500-38060; NREL: Golden, CO, USA, 2009.
2. Wayman, E.N.; Sclavonous, P.D. Coupled Dynamic Modeling of Floating Wind Turbine Systems. In Proceedings of the Offshore Technology Conference, OTC, Houston, TX, USA, 1–4 May 2006.
3. Lee, S. Dynamic Response Analysis of Spar Buoy Floating Wind Turbine Systems. Master's Thesis, Massachusetts Institute of Technology, Cambridge, MA, USA, 2008.
4. Naqvi, S.K. Scale Model Experiments on Floating Offshore Wind Turbines. Master's Thesis, Worcester Polytechnic Institute, Worcester, MA, USA, 2012.
5. Hong, S.; Lee, I.; Park, S.H.; Lee, C. An Experimental Study of the Effect of Mooring systems on the Dynamics of a SPAR Buoy-type Floating Offshore Wind Turbine. *J. Naval Archit. Ocean Eng.* **2015**, *7*, 559–579. [CrossRef]
6. Withee, J.E. Fully Coupled Dynamic Analysis of a Floating Wind Turbine System. Ph.D. Thesis, Massachusetts Institute of Technology, Cambridge, MA, USA, 2004.
7. Murray, J.; Yang, C.K.; Wooseuk, Y. An Extended Tension Leg Platform Design for Post-Katrina Gulf of Mexico. In Proceedings of the International Offshore and Polar Engineering Conference, ISOPE, Osaka, Japan, 21–26 July 2009.
8. Karimirad, M.; Moan, T. Wave and Wind-Induced Dynamic Response of a Spar-Type Offshore Wind Turbine. *J. Waterw. Port Coast. Ocean Eng.* **2011**, *138*, 9–20. [CrossRef]
9. Ren, N.; Li, Y.; Ou, J. The Wind-Wave Tunnel of a Tension Leg Platform Type Floating Offshore Wind Turbine. *J. Renew. Sustain. Energy* **2012**, *631*, 1–17. [CrossRef]
10. Martinez, M.S.; Natarajan, A.; Henriksen, L.C. *Feasibility Study of a Semi Floating Spar Buoy Wind Turbine Anchored with a Spherical Joint to the Sea Floor*; Technical Report INWIND; EWEA: Frankfurt, Germany, 2013.
11. Hadjihosseini, A.; Peinke, J.; Hoffmann, N.P. Stochastic Analysis of Ocean Wave States with and without Rogue Waves. *New J. Phys.* **2014**, *16*, 053037. [CrossRef]
12. Hadjihosseini, A.; Wächter, M.; Hoffmann, N.P.; Peinke, J. Capturing Rogue Waves by Multi-point Statistics. *New J. Phys.* **2016**, *18*, 013017. [CrossRef]

13. Hadjihosseini, A.; Lind, P.G.; Mori, N.; Hoffman, N.P.; Peinke, J. Rogue waves and entropy consumption. *Front. Phys.* **2017**, *120*, 30008. [CrossRef]

14. Lind, P.G.; Herraez, I.; Wächter, M.; Peinke, J. Fatigue Load Estimation through a Simple Stochastic Model. *Energies* **2014**, *7*, 8279–8293. [CrossRef]

15. Lind, P.G.; Vera-Tudela, L.; Wächter, M.; Kühn, M.; Peinke, J. Normal Behaviour Models for Wind Turbine Vibrations: Comparison of Neural Networks and a Stochastic Approach. *Energies* **2017**, *10*, 1944. [CrossRef]

16. Marino, E.; Lugni, C.; Borri, C. The role of the nonlinear wave kinematics on the global responses of an OWT in parked and operating conditions. *J. Wind Eng. Ind. Aerodyn.* **2013**, *123*, 363–376. [CrossRef]

17. Marino, E.; Giusti, A.; Manuel, L. Offshore wind turbine fatigue loads: The influence of alternative wave modeling for different turbulent and mean winds. *Renew. Energy* **2017**, *102*, 157–169. [CrossRef]

18. Nielsen, A.W.; Schlutter, F.; Sorensen, J.V.T.; Bredmose, H. Wave loads on a monopole in 3D waves. In Proceedings of the ASME 2012 31st International Conference on Ocean, Offshore and Arctic Engineering, Rio de Janeiro, Brazil, 1–6 July 2012.

19. Paulsen, B.T.; Bredmose, H.; Bingham, H.B. An efficient domain decomposition strategy for wave loads on surface piercing circular cylinders. *Coast. Eng.* **2014**, *86*, 57–76. [CrossRef]

20. Bredmose, H.; Slabiak, P.; Sahlberg-Nielsen, L.; Schlutter, F. Dynamic Excitation of Monopiles by Steep and Breaking Waves: Experimental and Numerical Study. In Proceedings of the ASME 2013 32nd International Conference on Ocean, Offshore and Arctic Engineering, Nantes, France, 9–14 June 2013.

21. Patel, M.H.; Witz, J.A. *Compliant Offshore Structures*; Butterworth-Heinemann Ltd.: Oxford, UK, 2013; pp. 80–83.

22. Peeringa, J.M. *Wave Loads on Offshore Wind Turbines*; Tech. Report Duurzame Energie; ECN Publisher: Amsterdam, The Netherlands, 2004.

23. Journee, J.M.J.; Massie, W.W. Wave Forces on Slender Cylinders. In *Offshore Hydromechanics*, 1st ed.; Delft University of Technology: Delft, The Netherlands, 2001; pp. 469–498.

24. Sarpkaya, T.; Isaacson, M. *Mechanics of Wave Forces on Offshore Structures*; van Nostrand Reinhold: New York, NY, USA, 1981.

25. Burrows, R.; Tickell, R.G.; Hames, D.; Najafian, G. Morison Wave Forces Coefficients for Application to Random Seas. *J. Appl. Ocean Res.* **1997**, *19*, 183–199. [CrossRef]

26. Henderson, A.R. *Design Methods for Offshore Wind Turbines at Exposed Sites*; Tudelft: Delft, The Netherlands, 2003.

27. Dean, R.G.; Dalrymple, R.A. *Water Wave Mechanics for Engineers and Scientists*; World Scientific Publishing Co. Pte. Ltd.: Singapore, 1984.

28. Lim, H.C. Optimum Design of a Sloping-wall-type Wave Absorber Placed in a Sinusoidal Propagating Wave. *Ocean Eng.* **2014**, *88*, 588–597. [CrossRef]

29. Zhu, L.; Lim, H.C. Hydrodynamic Characteristics of a Separated Heave Plate Mounted at a Vertical Circular Cylinder. *Ocean Eng.* **2017**, *131*, 213–223. [CrossRef]

30. Barltrop, N.D.P. *Floating Structures: A Guide for Design and Analysis*; Oilfield Publications, Inc.: Surrey, UK, 1998.

31. Nematbakhsh, A. A Nonlinear Computational Model of Floating Wind Turbines. Ph.D. Thesis, Worcester Polytechnic Institute, Worcester, MA, USA, 2013.

32. Kim, H.J.; Hong, S.Y. The Shape Design and Analysis of Floating Offshore Wind Turbine Structures with Damper Structure and Shallow Draft. *J. Ocean Wind Energy* **2014**, *1*, 170–176.

33. Wolfram, J.; Naghipour, M. On the Estimation of Morison Force Coefficients and Their Predictive Accuracy for Very Rough Circular Cylinders. *Appl. Ocean Res.* **1999**, *21*, 311–328. [CrossRef]

34. Berg, J.C. *Extreme Ocean Wave Conditions for Northern California Wave Energy Conversion Device*; Tech. Report SAND2011-9304; Sandia Report: Livermore, CA, USA, 2011.

Wind Turbine Power Curve Upgrades: Part II

Davide Astolfi * and Francesco Castellani

Department of Engineering, University of Perugia, Via G. Duranti 93, 06125 Perugia, Italy;
francesco.castellani@unipg.it

* Correspondence: davide.astolfi@unipg.it; Tel.: +39-075-585-3709

Abstract: Wind turbine power upgrades have recently become a debated topic in wind energy research. Their assessment poses some challenges and calls for devoted techniques: some reasons are the stochastic nature of the wind and the multivariate dependency of wind turbine power. In this work, two test cases were studied. The former is the yaw management optimization on a 2 MW wind turbine; the latter is a comprehensive control upgrade (pitch, yaw, and cut-out) for 850 kW wind turbines. The upgrade impact was estimated by analyzing the difference between the post-upgrade power and a data-driven simulation of the power if the upgrade did not take place. Therefore, a reliable model for the pre-upgrade power of the wind turbines of interest was needed and, in this work, a principal component regression was employed. The yaw control optimization was shown to provide a 1.3% of production improvement and the control re-powering provided 2.5%. Another qualifying point was that, for the 850 kW wind turbine re-powering, the data quality was sufficient for an upgrade estimate based on power curve analysis and a good agreement with the model result was obtained. Summarizing, evidence of the profitability of wind turbine power upgrades was collected and data-driven methods were elaborated for power upgrade assessment and, in general, for wind turbine performance control and monitoring.

Keywords: wind energy; wind turbines; control and optimization

---

1. Introduction

The wind capacity worldwide is impressively growing and furthermore many multi-megawatt wind turbines have been operating for years. The production optimization therefore has two main directions as regards each single wind turbine: On the one side, diminishing the unavailability time through condition-based maintenance strategies. For example, it is estimated that the unavailability time of a modern wind turbine is currently of the order of 3% [1] and can further diminish. On the other side, the technology update of wind turbines in their operational lifetime has been flourishing in the latest years and has been producing non-negligible improvements of wind kinetic energy conversion efficiency: the assessment and the methodologies for studying these wind turbine power upgrades constitute the topic of the present work.

For completeness, it should be said that production optimization can be conceived also at the wind farm level and there is very interesting scientific research devoted to layout optimization [2–6], wind farm control [7–9], and yaw active control for wake interactions management [10–14].

There are basically two types of wind turbine power upgrades that are currently employed in operating wind turbines: aerodynamic and control upgrades, or possibly a combination of the two. Examples of aerodynamic retrofitting of the blades are installation of vortex generator, passive flow control devices, Gurney flaps and so on [15–23]. Control upgrades typically deal with pitch [24,25], rotor revolutions per minute [26], and yaw management. The increase of production can be achieved also by modifying the wind speed cut-out management, as discussed, for example, in [27–29].

It likely happens that wind farm manufacturers and wind farm owners cooperate as regards to the technology improvement of operating wind turbines with forms of profit sharing of wind turbine power upgrades. This fact has considerably stimulated the high-level analysis of operational data in the industry and the collaboration with academia. Actually, there are several critical points about the assessment of wind turbine power upgrades:

- The wind source is stochastic and it does not make sense to compare the cumulative production before and after a power upgrade.
- It is difficult to account for the multiple dependency of wind turbine power on climate and operating conditions.
- It can be difficult to reliably know the wind conditions on site, in general because nacelle anemometers are mounted behind the rotors of the wind turbines and in particular because cup anemometers might not provide adequate measurement precision.

On these grounds, the power curve study might be a reliable tool for assessing power upgrades only when considerably long datasets are available, in order to avoid the effect of seasonal biases due to the variation of climate conditions on site. If, as commonly happens, wind farm practitioners aim at obtaining an estimate after just few months of upgrade operation, more complex and powerful methods are needed. A certain amount of literature has been flourishing about this problem and some interesting methods have recently been proposed. The common ground is the following idea:

- After the upgrade, of course, the power production is known if operation data are available.
- The production improvement is the difference between the measured production post-upgrade and a simulation of how much the wind turbine would have produced, in the same conditions, if the upgrade did not take place.
- The simulation must be achieved with a model based on pre-upgrade.

Chronologically, the first relevant study is [24]: in that work, a modification of the Gaussian kernel regression method is proposed to account for the multivariate dependency of the power of the wind turbine. Two upgrade test cases are studied: one is aerodynamic (vortex generator installation) and is studied through the analysis of operation data and the other regards the control of the pitch and is studied artificially because the pitch behavior is simulated and data are synthesized accordingly. In [30], another critical point of this kind of problems is discussed in depth: the statistical significance and the dataset dimensionality. The proposed solution is the use of time-resolved operation data, rather than Supervisory Control And Data Acquisition (SCADA) data. The former kind of data actually has sampling time of the order of the second, while the latter kind of data has sampling time of some minutes (typically, ten). In [30], it is shown that, using the time-resolved data, it is possible to obtain results that are similar to the ones from the Kernel-plus of [24], but with a much simpler method: it is the so-called power–power or side-by-side and it is based on the study of the power difference between the target (upgraded) wind turbine and a reference wind turbine, before and after the upgrade of the wind turbine of interest. In [25], three test cases of wind turbine power curve upgrades are considered: pitch angle optimization near the cut-in, vortex generators and passive flow control devices installation, cut-out management optimization. The first two test cases are studied by modeling the pre-upgrade power of the wind turbines of interest using an Artificial Neural Network (ANN) model having as input some operation variables of the nearby wind turbines. A control upgrade, dealing with the rotor revolutions per minute optimization in order to reach the most appropriate induction level, is studied in [26]: in that work, the power-power method is generalized by modeling the power of the upgraded wind turbine through a multivariate linear, employing as input variables some operation parameters of the nearby wind turbines. For other issues regarding this topic, see also [31–33].

On these grounds, the objective of the present work was furnishing further contributions to the topic of wind turbine power curve upgrades assessment. For doing this, two test cases were considered:

- The first test case deals with the yaw management optimization on a 2 MW wind turbine. There is a considerable literature about the potentiality of wind turbine efficiency improvement through

the advances in yaw management (see, for example, [34]), but, at this stage, the available studies mainly deal with simulation estimates (for example, recently, in [35], a yaw control strategy based on reinforced learning is designed). To the best of the authors knowledge, the study in this work is the first in the literature that is based on wind turbines in operation.

- The second test case deals with a control upgrade on a 850 kW wind turbine. Since the technology of this kind of device is gradually becoming obsolete, the re-powering on this wind turbine has been more impacting and has dealt with pitch, yaw, and cut-out management optimization. An interesting point about this upgrade is that the measuring chain was improved, through the installation of a sonic anemometer. Furthermore, the wind farm manufacturer arranged a testing period of the upgrade for some months, by alternating half-hour intervals characterized by the operation with the pre- and post-upgrade control logic. Therefore, it was possible to compare the two power curves quite reliably, because the wind speed data have good quality and because the data were collected in the same period and seasonal biases were therefore avoidable. This gives the possibility of verifying the model-based estimate of the production improvement through another, independent, approach.

The two above test cases were studied with particular attention to the methodology. The selected model for the power of the wind turbines of interest was a multivariate linear and it was decided that several operation parameters of the nearby wind turbines could in principle be input variables for the model. This can be considered a generalization of the concept of rotor-equivalent wind speed [36]: the conditions on site can be described, for example, through the blade pitches, the rotor revolutions per minute, and the power output of the wind turbines constituting the wind farm. As discussed in detail throughout the manuscript, remarkable collinearity between the possible covariates of the models was observed and for this reason a principal component regression [37] was employed, differently with respect, for example, to [33], where a stepwise regression algorithm [38] was used for input variables selection for an ordinary least squares regression. This approach is general and does not depend on the test case: therefore, it can be considered a contribution to the methodologies for wind turbine performance control and monitoring.

As regards the selected test cases, the results of this work are that the yaw control optimization on the 2 MW wind turbine provided a production improvement of 1.3% of the AEP; and the 850 kW wind turbine re-powering provided an improvement of 2.5% of the AEP.

The structure of the manuscript is as follows. In Section 2, the test cases and the datasets are described. Section 3 is devoted to the methods: the employed model is discussed in general and implemented in particular for the two selected test cases. In Section 4, the results for the production improvement are collected and discussed. Section 5 is devoted to the conclusions and to some further directions of the present work.

2. The Test Cases and the Datasets

One wind turbine for each test case wind farm underwent the corresponding upgrade (WTG02 in Wind Farm 1 and WTG022 in Wind Farm 2). Actually, the wind farm owner has been adopting the following approach as regards power upgrades: selecting some test wind turbines and, after some months of operation, assessing the impact of the upgrade on the grounds of studies such as the present one. Subsequently, the wind farm owner decides if it is worth extending the upgrade to the other wind turbines in the wind farm.

The employed datasets were obtained from the SCADA collected databases of the wind turbines. Their quality was checked as follows:

- Data were filtered on the request that all wind turbines in the wind farm were productive. This was done using the appropriate operation time counter available in the dataset.
- The quality of the anemometer data was crosschecked overall for each wind turbine through the analysis of the average power curve against the theoretical one and no relevant anomalies were detected.

- The quality of the data for each time step for each wind turbine was crosschecked by comparing the actual power production for the measured nacelle wind speed against the theoretical power curve. If a deviation larger than 30% was detected, the measurement was rejected.

2.1. Test Case 1: Yaw Control Optimization, 2 MW Wind Turbine

The wind farm of interest is composed of six horizontal-axis three-bladed wind turbines having 2 MW of rated power each and the rotor diameter is 92.5 m. The cut-in is 3.5 m/s and the cut-out is 25 m/s. The nominal wind speed is 14.5 m/s.

The layout of the wind farm is reported in Figure 1 and the wind turbine of interest (WTG02) is indicated in red. The wind farm is sited onshore in a gentle terrain in southern Italy. The inter-turbine distances go from the order of 7 rotor diameters (between nearest neighbors) up to the order of 19 rotor diameters.
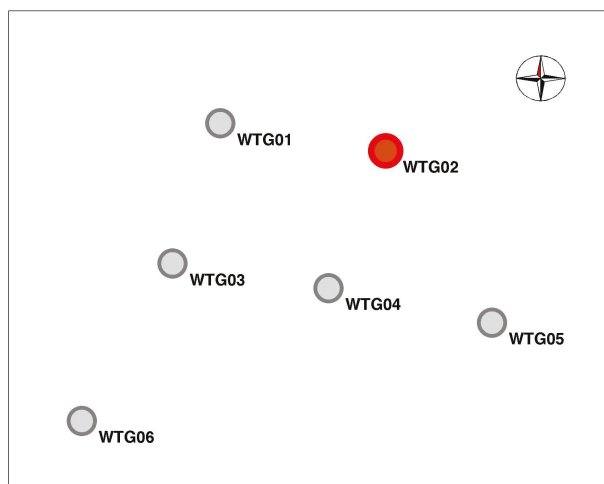

Figure 1. The layout of Wind Farm 1.

The data available were organized in two datasets as follows:

- The first dataset is denoted as D_{bef} and contains the data collected from 1 January 2017 to 20 August 2018. It is a period prior to the yaw control upgrade on turbine WTG02. It is composed of 35,971 data.
- The second dataset is denoted as D_{aft} and contains the data collected from 1 September 2018 to 1 January 2019. It is a period after the control optimization on turbine WTG02. It is composed of 9288 data.

In Figure 2, the normalized autocovariance of the power output of WTG02 is reported as a function of the lag (up to 20) for the D_{bef} dataset. This was done to crosscheck the assumption that each measurement can be considered independent with respect to the others.

The wind direction roses, measured at WTG02, during D_{bef} and D_{aft} are reported in Figure 3 and it arises that the distributions are very similar before and after the upgrade of the WTG02. Therefore, it can be argued that, as far as can be analyzed from the data available, the model formulation and use are not biased by differences in climatology. This is supported also by the fact that the ratio between the average nacelle wind speeds at WTG02 during D_{bef} and D_{aft} is 1.04.
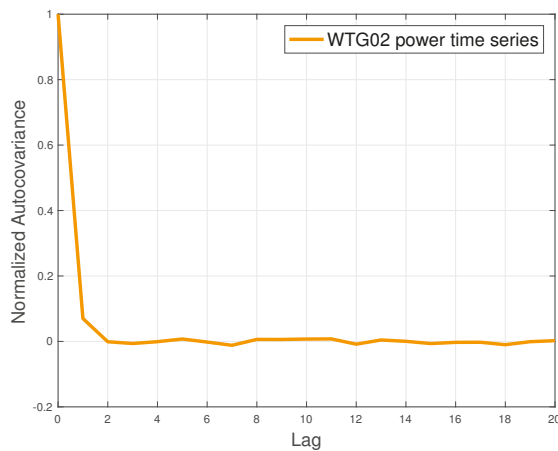
Figure 2. The normalized autocovariance of WTG02 power output (D_bef dataset) with maximum lag of 20.
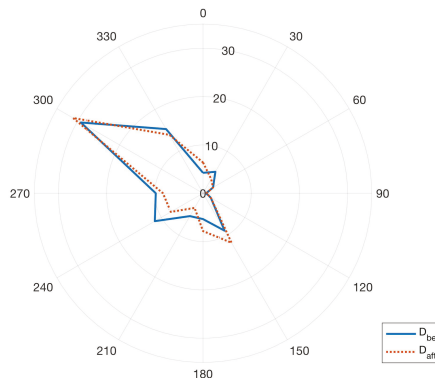

Figure 3. The wind direction rose for Wind Farm 1 during D_{bef} and D_{aft}.

The SCADA collected data have ten minutes of sampling time. The available validated measurements are:

- nacelle wind speed;
- nacelle wind direction;
- nacelle position;
- temperature outside the nacelle;
- active power;
- rotor rotational speed;
- generator rotational speed; and
- reference blade pitch.

The effect of the control upgrade was an improvement of the yaw management, especially for low and moderate wind intensities. This resulted in a decrease of the occurrence of high yaw misalignment. Qualitatively, this was assessed as follows: the yaw misalignment of WTG02 was computed as the difference between the wind direction measured at the nacelle and the position of the nacelle itself. As a pre-requisite, data were filtered on the request that WTG02 was in production. The plot of the yaw misalignment (in degrees) against the power is reported in Figure 4 for the datasets D_{bef} and D_{aft}.
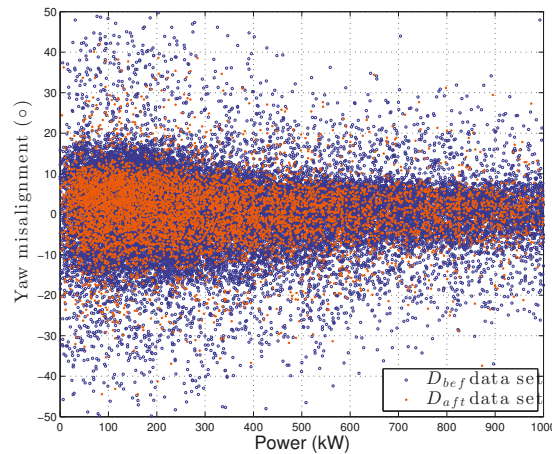
Figure 4. WTG02 yaw angle misalignment as a function of the power, for datasets D_{bef} and D_{aft}.

2.2. Test Case 2: Control Re-Powering, 850 kW Wind Turbine

The wind farm of interest is composed of twenty-three horizontal-axis three-bladed wind turbines having 850 kW of rated power each and the rotor diameter is 58 m. The cut-in is 3 m/s and the cut-out is 20 m/s. The nominal wind speed is 12.5 m/s.

The layout of the wind farm is reported in Figure 5 and the wind turbine of interest (WTG022) is indicated in red. The wind farm is sited onshore in a gentle terrain in northern France. The inter-turbine distances go from the order of four rotor diameters (between nearest neighbors) to the order of 100 rotor diameters. The wind direction rose on-site is quite uniform.
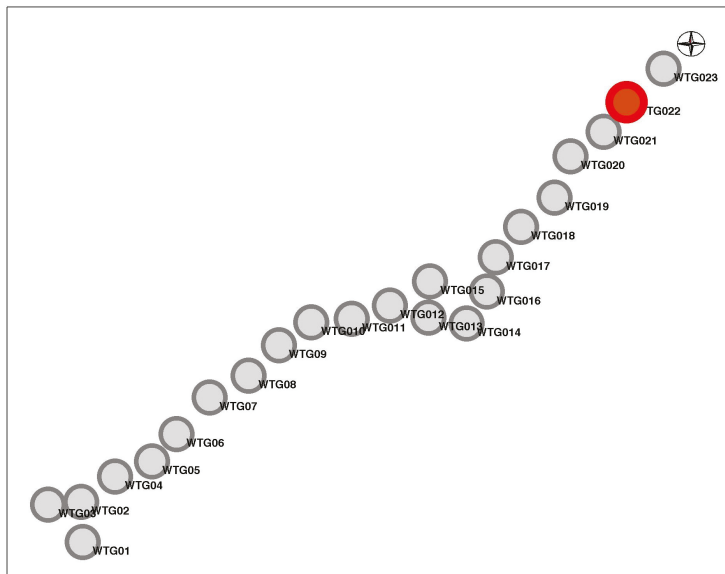

Figure 5. The layout of Wind Farm 2.

The data available were organized into two datasets as follows:

- The first dataset is denoted as D_{bef} and contains the data collected from 1 February 2018 to 20 August 2018. It is a period prior to the control upgrade on turbine WTG022. It is composed of 15,353 data.
- The second dataset is denoted as D_{aft} and contains the data collected from 24 August 2018 to 1 April 2019. It is a period after the control optimization on turbine WTG022. In this period, half-hour intervals of operation according to the pre- and post-upgrade logic were alternated. The former subset is indicated as D_{aft}^{non-up} and is composed of 4245 data. The latter subset is indicated as D_{aft}^{up} and is composed of 4265 data. Only D_{aft}^{up} is employed for the model-based estimate of the upgrade, while both subsets are employed for the power curve study in Section 4.2.

In Figure 6, the normalized autocovariance of the power output of WTG022 is reported as a function of a lag up to 20, for the D_{bef} dataset. This was done to crosscheck the assumption that each measurement can be considered independent with respect to the others.
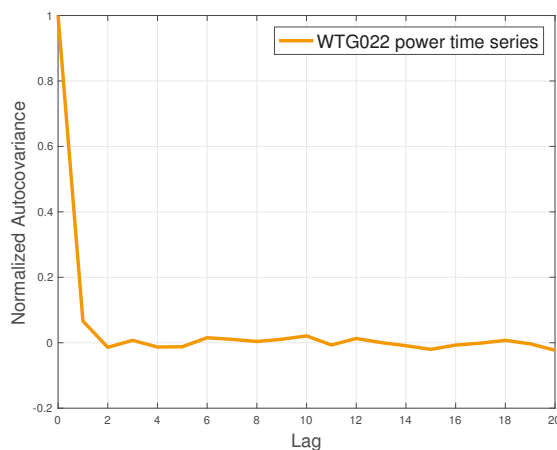

Figure 6. The normalized autocovariance of WTG022 power output (D_{bef} dataset) with maximum lag of 20.

The wind direction roses, measured at WTG022, during D_{bef} and D_{aft} are reported in Figure 7 and it arises that the distributions are similar before and after the upgrade of the WTG022. Therefore, it can be argued that, as far as can be analyzed from the data available, the model formulation and use are not remarkably biased by climatology effects. This is supported also by the fact that the ratio between the average nacelle wind speeds at WTG02 during D_{bef} and D_{aft} is 0.96.

The SCADA collected data have ten minutes of sampling time. The available validated measurements are:

- nacelle wind speed;
- temperature outside the nacelle; and
- active power.

It should be noticed that, after the upgrade intervention, WTG022 has a sonic anemometer at the nacelle. As discussed in detail in Section 4.2, the operation of WTG022 during D_{aft} was as follows: half-hour intervals of operation according to the pre- and post-upgrade control logic were alternated. Therefore, to assess the upgrade using the techniques proposed in Section 3, only the data in D_{aft} characterized by operation according to the upgraded control were selected. Instead, for the power curve study of Section 4.2, all data in D_{aft} were used, after dividing them according to the pre or post upgrade behavior.
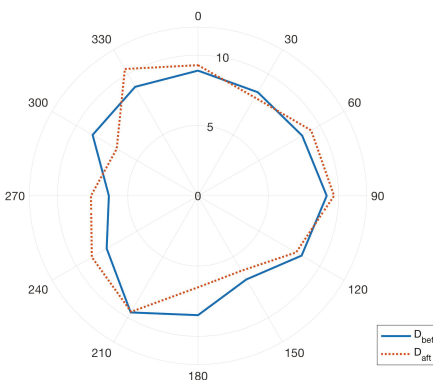
Figure 7. The wind direction rose for Wind Farm 1 during D_{bef} and D_{aft}.

3. The Methods

This section presents the formulating of a reliable model for the pre-upgrade power of the wind turbines of interest (WTG02 in Wind Farm 1 and WTG022 in Wind Farm 2). Section 4 is devoted in detail to the use of these models for the performance improvement estimate. For the moment, it is important to recall that a good model for the power of the wind turbines was needed because it was trained with pre-upgrade data and validated against a pre-upgrade dataset; the upgrade was quantified by simulating through the adopted model how the post-upgrade power would have been if the upgrade did not take place. In other words, the performance improvement was elaborated from how the residuals between measurements and model estimates changed after the upgrade with respect to before.

As anticipated in Section 1, the critical point was selecting the model type and the input variables. The discussion in [33], in relation to the work in [25], indicates that a linear model can be adequate for this objective. In other words, the general sense is that it is possible to approximate reliably the power of a wind turbine as a linear function of operation variables measured at the nearby wind turbines in the farm. This makes sense, not only by a statistical point of view, but also by the point of view of wind energy practice: actually, since a wind turbine acts as a filter to the wind fluctuations, the blade pitch, the rotor revolutions per minute and the active power of a wind turbine can likely be used for accounting for the on-site wind conditions [36].

The possible variables fed as input to the model are those indicated in Section 2.1 for Test Case 1 and those indicated in Section 2.2 for Test Case 2, for all the wind turbines in the wind farms except the upgraded ones. The decision of excluding the variables of the upgraded wind turbines as input variables to the model was motivated by the fact that the wind sensors might change after the upgrade (as in Test Case 2, see Section 2.2), or the upgrade might affect the measuring chain of the wind conditions (as discussed in [25,33]), or in general the relation between the power and the control (pitch, rotor revolutions per minute, etc) might change as a consequence of the upgrade. Therefore, since for the employed method one must assume that the input variables to the model are "probes" of the external conditions whose behavior does not change after the upgrade of the wind turbine of interest, it is straightforward that the variables of the upgraded wind turbine can only be the target (i.e., the output) of the model.

Similar to Astolfi et al. [33], a linear model was considered adequate for the objectives of this work. The critical point is the input variables selection: Tables 1 and 2 indicate that the possible covariates of the model can be highly correlated and this would lead to a non-optimal standard linear regression. On these grounds, Principal Component Regression (PCR) [39] was selected for this study. The use of this method for control and monitoring purposes in wind energy has been growing [40]. The procedure

is as follows. Let $Y_{n,1} = (y_i, \ldots, y_n)^T$ be the vector of measured output and $X_{n,p} = (x_i, \ldots, x_n)^T$ be the matrix of covariates. n is the number of observations and p is the number of covariates. In the following, it is assumed that X is normalized such that each covariate has zero mean.

The standard least squares regression poses that

$$Y = X\beta + \epsilon, \tag{1}$$

where β is the vector of regression coefficients that must be estimated from the data and ϵ is a vector of random errors. The ordinary least squares estimate of β is given by

$$\beta_{ols} = \left(X^T X\right)^{-1} X^T Y \tag{2}$$

The principal component estimate of β is obtained as follows. The principal component transformation of the covariates matrix can easily be expressed in terms of the singular value matrix factorization. Therefore, let

$$X = U\Delta V^T \tag{3}$$

be the singular value decomposition of X. This means that the columns of U and V are orthonormal sets of vectors denoting the left and right singular vectors of X and Δ is a diagonal matrix, whose elements are the singular values of X. This allows decomposing XX^T as:

$$XX^T = V\Lambda V^T, \tag{4}$$

where $\Lambda = diag\left(\lambda_1, \ldots, \lambda_p\right)$ and $\lambda_1 \geq \cdots \geq \lambda_p \geq 0$.

XV_i is the ith principal component and V_i is the ith loading corresponding to the ith principal value λ_i. Therefore, $W = XV$ can be viewed as a new covariates data matrix and the principal component regression basically is an ordinary least squares regression between Y and W. A powerful aspect of the principal component regression is that the decomposition in Equation (4) indicates a sort of regularization scheme: namely, the matrix W can be truncated including a desired number of principal components. This regularization addresses the problem of multicollinearity of covariates, because, when two or more covariates are highly correlated, X tends to lose its full rank and this implies that XX^T has some eigenvalues tending to 0: excluding the principal components associated to the smallest eigenvalues λ_i means regularizing the covariates matrix in order that it has full rank.

Finally, the PCR estimate of β is given as

$$\beta_{PCR} = V\left(W^T W\right)^{-1} W^T Y, \tag{5}$$

where it is assumed that the matrices can be truncated to a desired number of columns, i.e., principal components.

The selection of an adequate number of principal components for the regression is performed through K-fold cross-validation [41]. D_{bef} is divided randomly in two fractions: $(K-1)/K$ of the data are used for training and the remaining $1/K$ are used for validation. K was selected to be 10 for this study. The training data are employed for estimating β through principal component regression (Equation (5)) and the model estimate of the validation data is given by

$$\hat{Y}_{valid} = X_{valid}\beta_{PCR} \tag{6}$$

For each fold selection, the root mean square error is used as a metric for the goodness of the regression: it is given in general by

$$RMSE = \sqrt{\frac{1}{n_{valid}} \sum_{i=1}^{n_{valid}} (\hat{y}_i - y_i)^2}, \tag{7}$$

where n_{valid} is the number of rows of X_{valid}. The *RMSE* values are subsequently averaged on the folds selection and, therefore, for a given number j of principal components included in the regression, one can obtain a unique metric $RMSE_j$ for estimating the quality of the regression. The final selection of the number of principal components to be kept is performed as follows: given $RMSE_j$, the error estimate for the model with j principal components, if $RMSE_j - RMSE_{j+1} < 10\%$, k is selected. It should be noticed that, as discussed in Section 4, the results for both test cases do not depend sensibly on this choice, as long as a certain minimum number of principal components are included in the model.

A test can be formulated for inquiring the statistical significance of the fact the performance of the wind turbine of interest has changed after the upgrade. One can pose that the output can be modeled through a linear model before and after the upgrade and inquire to whether there has been a structural change, i.e. if the linear models before and after the upgrade are different. Suppose therefore that

$$\begin{cases} y_{bef} = X_{bef}\beta_{bef} + \epsilon_{bef} \\ y_{aft} = X_{aft}\beta_{aft} + \epsilon_{aft}, \end{cases} \tag{8}$$

where X is the matrix of explanatory variables, β is the vector of regression coefficients and ϵ are vectors of random errors.

The hypothesis test about the structural change of the regression regards the null hypothesis:

$$H_0 : \beta_{bef} = \beta_{aft}. \tag{9}$$

This is known as the Chow test and is based on the fact that, indicated with *RSS* the residuals sum of squares between measurements and model estimates, the quantity

$$F_{chow} = \frac{RSS_{bef} - RSS_{aft}}{RSS_{aft}} \frac{N - 2K - 2}{K} \tag{10}$$

is distributed as $F(K, N - 2K - 2)$, where K is the number of covariates and N is the number of data points.

Practically, the Chow test is performed as follows. The covariates matrices and the output vectors before and after the upgrade are vertically juxtaposed to form a total covariates matrix X_{TOT} and a total output vector Y_{TOT}. The test is performed with the assumption that the break point where the structural change can happen occurs when the data before the upgrade end and the data after the upgrade start.

3.1. Test Case 1

In Table 2, some sample results are reported for supporting the selection of the principal component regression: the correlation coefficients between the rotor rotational speeds of WTG01 and WTG03–WTG06 are reported. These covariates were selected because the rotor basically acts as a filter, smoothing the fluctuations caused by the turbulence, and it is therefore likely that in a wind farm the rotor speeds of nearby wind turbines are highly collinear.

Table 1. Matrix of model input variables correlation coefficients.

WTG	01	03	04	05	06
01	1	0.82	0.90	0.89	0.79
03	0.82	1	0.86	0.80	0.94
04	0.90	0.86	1	0.91	0.85
05	0.89	0.80	0.91	1	0.80
06	0.79	0.94	0.85	0.80	1

The structure of the model for the test case of interest was selected as follows. The output Y is the power of WTG02; the covariates matrix X was selected to be composed of power, rotor rotational speed, generator rotational speed, blade pitches, nacelle position and ambient temperature at each wind turbine of the wind farm, except WTG02. Therefore, if one considers the filtered D_{bef} dataset, Y is a vector of 25,044 data and X is a matrix having 24,055 rows and 30 columns (six variables for five wind turbines).

The results for the model K-fold cross-validation are reported in Figure 8 and, with the criterion exposed in Section 3, five principal components were selected. It should be noticed that a sensitivity analysis was carried and it was observed that the results do not change substantially by including more than five principal components.
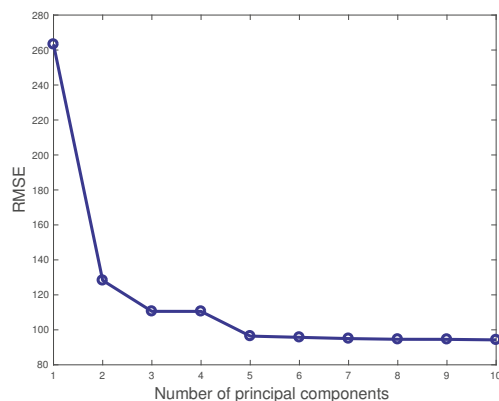

Figure 8. Average *RMSE* as a function of the number of principal components included in the regression.

As regards the Chow Test, the matrix X_{TOT} is composed of 31,392 rows (25,044 before upgrade and 6348 after upgrade) and 30 columns, and the vector Y_{TOT} is composed of 31392 elements. The break point position for the Chow test is 25,044 and the computed p-value is lower than 10^{-32}. This clearly indicates that the linear relation between covariates matrix and the target has a structural change after the upgrade of WTG02.

3.2. Test Case 2

In Table 2, the correlation coefficients between some sample covariates are reported. The powers of WTG018–WTG021 and WTG023 was selected for reporting in Table 2: these covariates was selected for readability of the table and mostly because those wind turbines are the nearest to the target WTG022 and therefore those covariates are likely to be selected for a standard least squares regression. The remarkably high values reported in Table 2 support the selection of the principal component regression as model type.

Table 2. Matrix of model input variables correlation coefficients.

WTG	018	019	020	021	023
018	1	0.94	0.93	0.92	0.87
019	0.94	1	0.93	0.93	0.90
020	0.93	0.93	1	0.95	0.90
021	0.92	0.93	0.95	1	0.93
023	0.97	0.90	0.90	0.93	1

The structure of the model for the test case of interest was selected as follows. The output Y is the power of WTG022. The covariates matrix X is composed of the available validated measurements: nacelle wind speed, power and ambient temperature at each wind turbine of the wind farm, except WTG022. Therefore, if one considers the filtered D_{bef} dataset, Y is a vector of 15,353 data and X is a matrix having 15,353 rows and 66 columns (three variables for 22 wind turbines).

The results for the model K-fold cross-validation are reported in Figure 9 and, through the criterion exposed in Section 3, the number of selected principal components results to be six. It should be noticed that the results do not change significantly by including more than six principal components in the model.
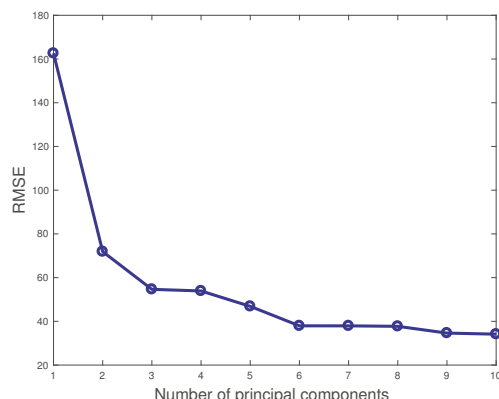

Figure 9. Average *RMSE* as a function of the number of principal components included in the regression.

As regards the Chow Test, the matrix X_{TOT} is composed of 19,618 rows (15,353 before upgrade and 4265 after upgrade) and 66 columns, the vector Y_{TOT} is composed of 19,618 elements. The break point position for the Chow test is 15,353 and the computed p-value is lower than 10^{-32}. This clearly indicates that the linear relation between covariates matrix and the target has a structural change after the upgrade of WTG022.

4. The Results

The procedure for assessing the upgrade Was based on the following idea. After an upgrade installation, through the SCADA collected data, it is possible to know the power production of the upgraded wind turbine. To estimate the impact of the upgrade, one should know how much the wind turbine would have produced if the upgrade did not take place. The most reliable and practical way to obtain this kind of estimate is through a data-driven model, based on the pre-upgrade datasets. A reliable model was achieved (Section 3) and it was used for the upgrade assessment presented below.

The procedure is as follows. The datasets available were organized in this way:

- D_{bef} was randomly divided in two subsets: D0 ($\frac{2}{3}$ of the data) and D1 ($\frac{1}{3}$ of the data). D0 was used for training the model and constructing the weight matrix W and D1, the pre-upgrade dataset, was employed for validating the model.
- D_{aft}, the post-upgrade dataset, was employed for estimating the power upgrade. For notation consistency, it is also referred to equivalently as D2.

Notice that, for Test Case 2, the dataset D_{aft}^{up} was employed as D2.

The residuals between the measurement y and the simulation $\hat{y}$, for the datasets D1 and D2, were studied. The focus was in how the residuals varied after the upgrade. Therefore, consider Equation (11) with $i = 1, 2$.

$$R(x_i) = y(x_i) - \hat{y}(x_i). \tag{11}$$

A Student's *t*-test was performed to inquire if there was any statistically significant change in the turbine output after the upgrade. The t statistic is computed as

$$t = \frac{\bar{R}_2 - \bar{R}_1}{\sigma_R \sqrt{\frac{1}{N_1} + \frac{1}{N_2}}}. \tag{12}$$

In Equation (12), N_1 and N_2 are the numbers of data in, respectively, D1 and D2; $\bar{R}_1$ and $\bar{R}_2$ are the average residuals in datasets D1 and D2 respectively; and σ_R is given in Equation (13):

$$\sigma_R = \sqrt{\frac{(N_1 - 1)\, S_2^2 + (N_2 - 1)\, S_2^2}{N_1 + N_2 - 2}}, \tag{13}$$

where S_1 and S_2 are the standard deviations of the residuals in datasets D1 and D2, respectively.

As regards the upgrade estimate, for $i = 1, 2$, one computes

$$\Delta_i = 100 * \frac{\sum_{x \in Di} (y(x) - \hat{y}(x))}{\sum_{x \in Di} y(x)} \tag{14}$$

and

$$\delta_i = \frac{1}{N_i} \sum_{x \in Di} y(x_i) - \hat{y}(x_i), \tag{15}$$

where N_i is the number of data points in the datasets D1 and D2, respectively. Notice that, if the model is reliable, one should have that $\delta_1 \simeq 0$ and $\Delta_1 \simeq 0$, differently with what should happen as regards δ_2 and Δ_2 if the upgrade is really effective. Finally, the quantity

$$\Delta = \Delta_2 - \Delta_1 \tag{16}$$

can be taken a percentage estimate of the production improvement. In the case the datasets D1 and D2 are characterized by considerably different y distributions, it might be appropriate to take this into account by renormalizing Equation (16): a reasonable correction factor can be the ratio between the y averages in datasets D2 and D1.

The above procedure can be repeated several times to synthesize experiment repetition: at each run of the model, a different D0 (training set) and therefore D1 (pre-upgrade validation dataset) can be selected. Notice that this basically corresponds to repeating the *K*-fold cross-validation. The difference with respect to the procedure described in Section 3 is that in this case the model structure was always the same and it was exactly the one selected on the grounds of the discussion in Section 3. The way the pre-upgrade data were divided was also changed with respect to Section 3. The selection of D0 and D1 actually corresponded to $K = 33.\bar{3}$. This was done because it agrees with most of the rule of thumbs for data partition for this kind of tasks and because, with this selection, the dimensions of D1 and D2 (the post-upgrade dataset) have the same order of magnitude.

Therefore, the Δ estimate varied at each run of the model, because the training data changed and, therefore Δ_1 and Δ_2 changed. In principle, it could be possible to select randomly a subset of D2 as post-upgrade simulation dataset, but in this work this choice was avoided. The reason was that typically D2 is shorter than D0 and D1, because for practical reasons an upgrade is assessed as soon as possible with good reliability. The above bootstrap technique therefore allowed having several estimates of Δ with the same data: the final estimate was always the average and it is presented below with its standard deviation. This corresponds to the procedure of Section 3 with J repetitions: for this part of the study, J was selected based on when the Δ average and standard deviation became fairly stable. It was observed that $J = 30$ is sufficient for this task.

4.1. Test Case 1

Since the effect of the upgrade regards especially the low-moderate wind intensity, data were filtered on the request that the power of WTG02 is less than 1 MW. After this further filter, the number of data was 25,044 for D_{bef} and 6348 for D_{aft}.

The *t*-statistic (Equation (12)) was computed to be of the order of 10^{-10} and this indicates that the probability that the upgrade was ineffective was correspondingly low.

Table 3 reports the results for the average (over the J model runs) Δ_i and δ_i with $i = 1, 2$ (Equations (14) and (15)). From these results, it arises that the upgrade could be detected as an average absolute increase of 13.5 kW in the difference between WTG02 power measurements and model estimates. Notice that the average value of the residuals for datasets D1 was extremely low (0.1 kW) and, correspondingly, the average estimate of Δ_1 (Equation (16)), i.e. the percentage error on the cumulative production, was extremely low as well. This indicates that the model was particularly reliable as regards the simulation of the pre-upgrade behavior of the WTG02.

In Figure 10, the plot of $R(x_1)$ and $R(x_2)$ on a sample model run is reported. The data were averaged in power production intervals, whose amplitude was 5% of the rated. From this plot, the effect of the upgrade can be read as an increase of the difference between the WTG02 power measurements and the WTG02 power model estimates.

Table 3. Average absolute and percentage residuals between measurement and model estimation.

| Residual	δ (kW)	Δ (%)
$R(x_1)$	0.1	0.009
$R(x_2)$	13.5	4.1
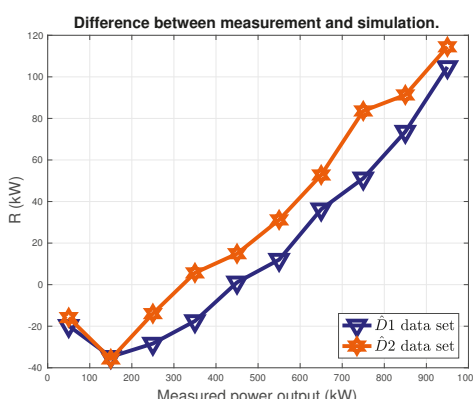
Figure 10. The average difference R between power measurement y and estimation $\hat{y}$ (Equation (11)). Datasets: D1 and D2. Sample run of the model.

From the results in Table 3 and Equation (14), the average production improvement was estimated as $\Delta = 4.3\%$, with a standard deviation of 0.4%: in other words, with the proposed method it was computed that WTG02, during the dataset D2, produced below 1 MW, the 4.1% more than it would have done if the upgrade had not been adopted. A reference long-term power or wind speed distribution can be employed to estimate how much this corresponds in terms of annual energy production and the average result is $\Delta_{AEP} = 1.3 \pm 0.1\%$. This result is consistent with the test case studies in [25]: the order of magnitude of the impact of multi-megawatt wind turbine control optimization can typically be estimated as 1% of the AEP. It is interesting notice that, to the best of the authors knowledge, this is the first estimate in the literature based on operation data of the impact of yaw control optimization.

4.2. Test Case 2

The *t*-statistic (Equation (12)) was computed to be of the order of 10^{-15} and this indicates that the probability that the upgrade was ineffective was correspondingly low.

Table 4 reports the results for the average (over the *J* model runs) Δ_i and δ_i with $i = 1, 2$ (Equations (14) and (15)). It arises that the upgrade could be detected as an average absolute increase of 3.9 kW in the difference between WTG022 power measurements and model estimates. The average value of the residuals for datasets D1 was very low (0.2 kW) and correspondingly, the average estimate of Δ_1 (Equation (16)), i.e. the percentage error on the cumulative production, was extremely low as well. This indicates that the model was reliable as regards the simulation of the pre-upgrade behavior of the WTG022.

Table 4. Average absolute and percentage residuals between measurement and model estimation.

Residual	δ (kW)	Δ (%)
$R(\boldsymbol{x}_1)$	0.2	0.009
$R(\boldsymbol{x}_2)$	3.9	2.5

In Figure 11, the plot of $R(\boldsymbol{x}_1)$ and $R(\boldsymbol{x}_2)$ on a sample model run is reported. The data were averaged in power production intervals, whose amplitude was 10% of the rated. From this plot, the effect of the upgrade can be read as an increase of the difference between the WTG022 power measurements and the WTG022 power model estimates, especially for moderately low wind intensities and approaching rated power.
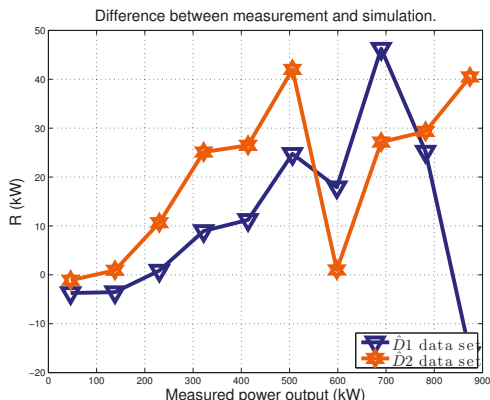

Figure 11. The average difference *R* between power measurement *y* and estimation $\hat{y}$ (Equation (11)). Datasets: D1 and D2. Sample run of the model.

From the results in Table 3 and Equation (14), the average production improvement was estimated as $\Delta = 2.5\%$, with a standard deviation of 0.2%: in other words, with the proposed method it was computed that WTG022, during the dataset D2, produced 2.5% more than it would have done if the upgrade had not been adopted.

Power Curve Analysis

As anticipated in Section 2, the post-upgrade operation during dataset D_{aft} was as follows: half-hour intervals were alternated, during which WTG022 was operating, respectively, according to the pre- and post-upgrade control logic. This was done to assess practically in real time the effect of the upgrade. With these data available and taking into account that, during D_{aft}, a sonic anemometer was collecting data at WTG022 nacelle, it was reasonable to study the power curve.

In Figure 12, the two power curves measured during D_{aft} are reported. Data were averaged in wind speed intervals having 0.5 m/s of amplitude. In Figure 13, the difference between these two curves is plotted. In Figure 13, it can interestingly be observed that the upgraded operation mode indeed lost performance around 10 m/s: the same situation was observed from the residuals presented in Figure 11. Since this study was performed with only few months of data in D_{aft}, it is plausible to expect that this situation was adjusted in the following, to obtain a performance improvement along the whole power curve.
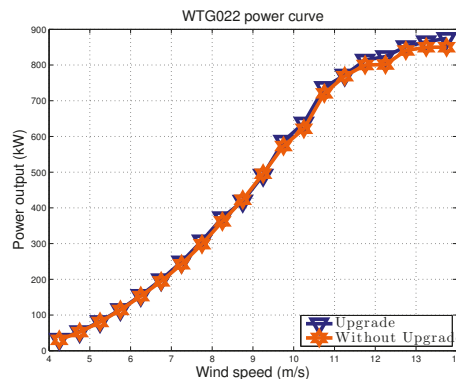

Figure 12. WTG022 power curve during D_{aft}.
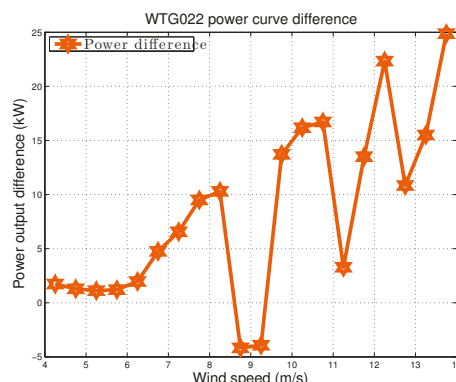

Figure 13. Difference between the WTG022 power curves of Figure 12.

The production improvement was estimated as follows: the power curve, according to the pre-upgrade logic in Figure 12, and the power difference in Figure 13, were weighted against the wind distribution during the whole D_{aft} dataset. The ratio between these two quantities provided an estimate of how much the production would have improved during D_{aft} if the power curve was always the improved one, with respect to the production that would have been obtained if the power curve was always the non-improved one. The improvement computed in this way amounted to 2.3% of the production. Even though it was computed with a different approach, it is interesting to notice that it agreed fairly well with the estimate reported in Section 4.2.

5. Conclusions

In this study, two test cases of wind turbine power curve upgrades were analyzed: the common ground between them is that the upgrade regards the control of the wind turbines. The difference between the two test cases is that one wind turbine (Test Case 1) has a quite recent technology (it is a 2 MW wind turbine) and the control upgrade deals only with one aspect (the management of the yaw); the other wind turbine under investigation (Test Case 2) belongs instead to a less recent technology (the rated power is 850 kW) and the upgrade has consequently involved several aspects of the control (yaw, pitch, and cut-out) and included the update of the anemometer sensors at the nacelle.

Despite being organized as a test case discussion, this study was strongly characterized by a methodological approach. Actually, the point with the study of wind turbine power curve upgrades is that it is difficult to assess them reliably using operation data analysis techniques such as the power curve, because of the multivariate dependence of the power of a wind turbine on climate conditions and working parameters. The problem of wind turbine power curve upgrades study therefore translates into the following question: how can the power of a wind turbine be modeled reliably? It is evident that the answer to this question can be exploited for several problems regarding the control and monitoring of wind turbines and, in general, of complex systems. As regards wind turbines, for example, similar approaches are employed in [42] for the study of how much the pitch misalignment impacts on the performance.

The turning point for the present study was practically adopting the other wind turbines in the wind farm as probes of on-site conditions. This somehow generalized the concept of rotor-equivalent wind speed, discussed, for example, in [36]: since the wind turbine acts as a filter, some working parameters such as active power, blade pitches, rotor or generator revolutions per minute can robustly describe the wind farm at the micro-scale level. Therefore, the idea of this study was modeling the power of the wind turbines of interest, according to their pre-upgrade behavior, as a linear function of the wind and operation conditions measured at the nearby wind turbines: this can basically be considered a generalization of the so-called power–power method, adopted, for example, in [30]. Since for the test cases considered in this work the possible covariates for a linear model displayed a remarkable collinearity, a principal component regression was adopted.

Using this modeling technique, the impact of the upgrades could be elaborated from how the residuals between power measurements and power model estimates vary after the upgrade with respect to before. The results for the selected test cases are the following: the yaw control optimization on the 2 MW wind turbine was estimated as 1.3% of the AEP; and the re-powering on the 850 kW wind turbine was estimated as 2.5% of the AEP.

There are at least two other remarkable aspects as regards the selected test cases. To the best of the authors knowledge, Test Case 1 is the first assessment in the literature of yaw control optimization using operation data and the obtained results indicate that the yaw management optimization is a promising direction for improving the power production of wind turbines. It is therefore valuable to push forward this line of research, as recently done, for example, in [35]. As regards Test Case 2, it was possible to obtain another estimate of the impact of the upgrade using the power curve study. Actually, with the re-powering, the anemometer sensors were updated and a sonic anemometer was installed. Furthermore, in the post upgrade period examined for this study, the operation of the wind turbine

was alternated: half an hour according to the pre-upgrade logic and half an hour according to the post-upgrade logic, and so on. The quality of the data and the fact that they were collected in the same period (avoiding seasonal biases) allowed studying the power curve reliably and the improvement estimate was shown to be in good agreement with the computation from the multivariate model.

There are several further directions of the present work. Currently, some test cases are at study for which a linear model is not adequate, probably because of complex climatology conditions on site. Therefore, it is planned to investigate nonlinear approaches for this kind of studies and to inquire what site characteristics call for nonlinearity. An interesting development is the use of the methods of this work for other control and monitoring issues related to wind turbine operation: for example, monitoring the effect of blade pitches re-alignment according to the technique proposed in [43], or monitoring the operation of the wind turbines [40]. Furthermore, a very promising direction of the studies about wind turbine power curve upgrades is the use of time-resolved data, having sampling time of the order of second: this kind of data have considerable potentiality for performance control and monitoring [44], but their time scale calls for more advanced time-series analysis [45].

References

1. Tchakoua, P.; Wamkeue, R.; Ouhrouche, M.; Slaoui-Hasnaoui, F.; Tameghe, T.A.; Ekemb, G. Wind turbine condition monitoring: State-of-the-art review, new trends, and future challenges. *Energies* **2014**, *7*, 2595–2630. [CrossRef]
2. Parada, L.; Herrera, C.; Flores, P.; Parada, V. Wind farm layout optimization using a Gaussian-based wake model. *Renew. Energy* **2017**, *107*, 531–541. [CrossRef]
3. Shakoor, R.; Hassan, M.Y.; Raheem, A.; Wu, Y.K. Wake effect modeling: A review of wind farm layout optimization using Jensen's model. *Renew. Sustain. Energy Rev.* **2016**, *58*, 1048–1059. [CrossRef]
4. Feng, J.; Shen, W.Z. Solving the wind farm layout optimization problem using random search algorithm. *Renew. Energy* **2015**, *78*, 182–192. [CrossRef]
5. Sorkhabi, S.Y.D.; Romero, D.A.; Yan, G.K.; Gu, M.D.; Moran, J.; Morgenroth, M.; Amon, C.H. The impact of land use constraints in multi-objective energy-noise wind farm layout optimization. *Renew. Energy* **2016**, *85*, 359–370. [CrossRef]
6. Chen, Y.; Li, H.; He, B.; Wang, P.; Jin, K. Multi-objective genetic algorithm based innovative wind farm layout optimization method. *Energy Convers. Manag.* **2015**, *105*, 1318–1327. [CrossRef]
7. Park, J.; Law, K.H. Cooperative wind turbine control for maximizing wind farm power using sequential convex programming. *Energy Convers. Manag.* **2015**, *101*, 295–316. [CrossRef]
8. Park, J.; Law, K.H. A data-driven, cooperative wind farm control to maximize the total power production. *Appl. Energy* **2016**, *165*, 151–165. [CrossRef]
9. Wang, F.; Garcia-Sanz, M. Wind farm cooperative control for optimal power generation. *Wind Eng.* **2018**, *42*, 547–560. [CrossRef]
10. Gebraad, P.; Thomas, J.J.; Ning, A.; Fleming, P.; Dykes, K. Maximization of the annual energy production of wind power plants by optimization of layout and yaw-based wake control. *Wind Energy* **2017**, *20*, 97–107. [CrossRef]
11. Gebraad, P.; Teeuwisse, F.; Van Wingerden, J.; Fleming, P.A.; Ruben, S.; Marden, J.; Pao, L. Wind plant power optimization through yaw control using a parametric model for wake effects—A CFD simulation study. *Wind Energy* **2016**, *19*, 95–114. [CrossRef]
12. Fleming, P.A.; Ning, A.; Gebraad, P.M.; Dykes, K. Wind plant system engineering through optimization of layout and yaw control. *Wind Energy* **2016**, *19*, 329–344. [CrossRef]

13. Campagnolo, F.; Petrović, V.; Bottasso, C.L.; Croce, A. Wind tunnel testing of wake control strategies. In Proceedings of the IEEE American Control Conference (ACC), Boston, MA, USA, 6–8 July 2016; pp. 513–518.

14. Fleming, P.; Annoni, J.; Shah, J.J.; Wang, L.; Ananthan, S.; Zhang, Z.; Hutchings, K.; Wang, P.; Chen, W.; Chen, L. Field test of wake steering at an offshore wind farm. *Wind Energy Sci.* **2017**, *2*, 229–239. [CrossRef]

15. Barlas, T.K.; Van Kuik, G. Review of state of the art in smart rotor control research for wind turbines. *Prog. Aerosp. Sci.* **2010**, *46*, 1–27. [CrossRef]

16. Tsai, K.C.; Pan, C.T.; Cooperman, A.M.; Johnson, S.J.; Van Dam, C. An innovative design of a microtab deployment mechanism for active aerodynamic load control. *Energies* **2015**, *8*, 5885–5897. [CrossRef]

17. Fernández-Gámiz, U.; Marika Velte, C.; Réthoré, P.E.; Sørensen, N.N.; Egusquiza, E. Testing of self-similarity and helical symmetry in vortex generator flow simulations. *Wind Energy* **2016**, *19*, 1043–1052. [CrossRef]

18. Aramendia, I.; Fernandez-Gamiz, U.; Ramos-Hernanz, J.A.; Sancho, J.; Lopez-Guede, J.M.; Zulueta, E. Flow Control Devices for Wind Turbines. In *Energy Harvesting and Energy Efficiency*; Springer: Berlin, Germany, 2017; pp. 629–655.

19. Fernandez-Gamiz, U.; Zulueta, E.; Boyano, A.; Ansoategui, I.; Uriarte, I. Five megawatt wind turbine power output improvements by passive flow control devices. *Energies* **2017**, *10*, 742. [CrossRef]

20. Fernandez-Gamiz, U.; Gomez-Mármol, M.; Chacón-Rebollo, T. Computational Modeling of Gurney Flaps and Microtabs by POD Method. *Energies* **2018**, *11*, 2091. [CrossRef]

21. Gutierrez-Amo, R.; Fernandez-Gamiz, U.; Errasti, I.; Zulueta, E. Computational Modelling of Three Different Sub-Boundary Layer Vortex Generators on a Flat Plate. *Energies* **2018**, *11*, 3107. [CrossRef]

22. Fernandez-Gamiz, U.; Errasti, I.; Gutierrez-Amo, R.; Boyano, A.; Barambones, O. Computational Modelling of Rectangular Sub-Boundary Layer Vortex Generators. *Appl. Sci.* **2018**, *8*, 138. [CrossRef]

23. Aramendia, I.; Fernandez-Gamiz, U.; Zulueta, E.; Saenz-Aguirre, A.; Teso-Fz-Betoño, D. Parametric Study of a Gurney Flap Implementation in a DU91W (2) 250 Airfoil. *Energies* **2019**, *12*, 294. [CrossRef]

24. Lee, G.; Ding, Y.; Xie, L.; Genton, M.G. A kernel plus method for quantifying wind turbine performance upgrades. *Wind Energy* **2015**, *18*, 1207–1219. [CrossRef]

25. Astolfi, D.; Castellani, F.; Terzi, L. Wind Turbine Power Curve Upgrades. *Energies* **2018**, *11*, 1300. [CrossRef]

26. Astolfi, D.; Castellani, F.; Berno, F.; Terzi, L. Numerical and Experimental Methods for the Assessment of Wind Turbine Control Upgrades. *Appl. Sci.* **2018**, *8*, 2639. [CrossRef]

27. Bossanyi, E.; King, J. Improving wind farm output predictability by means of a soft cut-out strategy. In Proceedings of the European Wind Energy Conference and Exhibition EWEA, Copenhagen, Denmark, 16–19 April 2012; Volume 2012.

28. Petrović, V.; Bottasso, C.L. Wind turbine optimal control during storms. *J. Phys. Conf. Ser.*. **2014**, *524*, 012052. [CrossRef]

29. Astolfi, D.; Castellani, F.; Lombardi, A.; Terzi, L. About the extension of wind turbine power curve in the high wind region. *J. Solar Energy Eng.* **2019**, *141*, 014501. [CrossRef]

30. Hwangbo, H.; Ding, Y.; Eisele, O.; Weinzierl, G.; Lang, U.; Pechlivanoglou, G. Quantifying the effect of vortex generator installation on wind power production: An academia-industry case study. *Renew. Energy* **2017**, *113*, 1589–1597. [CrossRef]

31. Astolfi, D.; Castellani, F.; Terzi, L. A SCADA data mining method for precision assessment of performance enhancement from aerodynamic optimization of wind turbine blades. *J. Phys. Conf. Ser.* **2018**, *1037*, 032001. [CrossRef]

32. Terzi, L.; Lombardi, A.; Castellani, F.; Astolfi, D. Innovative methods for wind turbine power curve upgrade assessment. *J. Phys. Conf. Ser.* **2018**, *1102*, 012036. [CrossRef]

33. Astolfi, D.; Castellani, F.; Fravolini, M.L.; Cascianelli, S.; Terzi, L. Precision Computation of Wind Turbine Power Upgrades: An Aerodynamic and Control Optimization Test Case. *J. Energy Resour. Technol.* **2019**, *141*, 051205. [CrossRef]

34. Song, D.; Yang, J.; Fan, X.; Liu, Y.; Liu, A.; Chen, G.; Joo, Y.H. Maximum power extraction for wind turbines through a novel yaw control solution using predicted wind directions. *Energy Convers. Manag.* **2018**, *157*, 587–599. [CrossRef]

35. Saenz-Aguirre, A.; Zulueta, E.; Fernandez-Gamiz, U.; Lozano, J.; Lopez-Guede, J.M. Artificial Neural Network Based Reinforcement Learning for Wind Turbine Yaw Control. *Energies* **2019**, *12*, 436. [CrossRef]

36. Wagner, R.; Cañadillas, B.; Clifton, A.; Feeney, S.; Nygaard, N.; Poodt, M.; St Martin, C.; Tüxen, E.; Wagenaar, J. Rotor equivalent wind speed for power curve measurement—Comparative exercise for IEA Wind Annex 32. *J. Phys. Conf. Ser.* **2014**, *524*, 012108. [CrossRef]

37. Green, W.H. *Econometric Analysis*; Maxwell Macmillan International: New York City, NY, USA, 1997.

38. Pope, P.; Webster, J. The use of an F-statistic in stepwise regression procedures. *Technometrics* **1972**, *14*, 327–340. [CrossRef]

39. Frank, L.E.; Friedman, J.H. A statistical view of some chemometrics regression tools. *Technometrics* **1993**, *35*, 109–135. [CrossRef]

40. Pozo, F.; Vidal, Y. Wind turbine fault detection through principal component analysis and statistical hypothesis testing. *Energies* **2016**, *9*, 3. [CrossRef]

41. Refaeilzadeh, P.; Tang, L.; Liu, H. Cross-validation. In *Encyclopedia of Database Systems*; Springer: Berlin, Germany, 2009; pp. 532–538.

42. Astolfi, D. A Study of the Impact of Pitch Misalignment on Wind Turbine Performance. *Machines* **2019**, *7*, 8. [CrossRef]

43. Elosegui, U.; Egana, I.; Ulazia, A.; Ibarra-Berastegi, G. Pitch angle misalignment correction based on benchmarking and laser scanner measurement in wind farms. *Energies* **2018**, *11*, 3357. [CrossRef]

44. Gonzalez, E.; Stephen, B.; Infield, D.; Melero, J.J. Using high-frequency SCADA data for wind turbine performance monitoring: A sensitivity study. *Renew. Energy* **2019**, *131*, 841–853. [CrossRef]

45. Rodrigues, P.M.; Salish, N. Modeling and forecasting interval time series with threshold models. *Adv. Data Anal. Classif.* **2015**, *9*, 41–57. [CrossRef]

Multiple Wind Turbine Wakes Modeling Considering the Faster Wake Recovery in Overlapped Wakes

Zhenzhou Shao, Ying Wu, Li Li, Shuang Han and Yongqian Liu *

State Key Laboratory of Alternate Electrical Power System with Renewable Energy Sources,
North China Electric Power University, Changping District, Beijing 102206, China; ncepushao@163.com (Z.S.);
wu_ying@ncepu.edu.cn (Y.W.); lili@ncepu.edu.cn (L.L.); hanshuang1008@sina.com (S.H.)

* Correspondence: yqliu@ncepu.edu.cn; Tel.: +86-010-6177-2048

check for
updates

Abstract: In a wind farm some wind turbines may be affected by multiple upwind wakes. The commonly used approach in engineering to simulate the interaction effect of different wakes is to combine the single analytical wake model and the interaction model. The higher turbulence level and shear stress profile generated by upwind turbines in the superposed area leads to faster wake recovery. The existing interaction models are all analytical models based on some simple assumptions of superposition, which cannot characterize this phenomenon. Therefore, in this study, a mixing coefficient is introduced into the classical energy balance interaction model with the aim of reflecting the effect of turbulence intensity on velocity recovery in multiple wakes. An empirical expression is also given to calculate this parameter. The performance of the new model is evaluated using data from the Lillgrund and the Horns Rev I offshore wind farms, and the simulations agree reasonably with the observations. The comparison of different interaction model simulation results with measured data show that the calculation accuracy of this new interaction model is high, and the mean absolute percentage error of wind farm efficiency is reduced by 5.3% and 1.58%, respectively, compared to the most commonly used sum of squares interaction model.

Keywords: wind farm; analytical model; wake interaction model; turbulence intensity; mixing coefficient; wind farm efficiency

1. Introduction

The wake from upwind wind turbines leads to decreased wind power output and increased fatigue load of downwind turbines. In a large wind farm, the power loss caused by the wake effect normally accounts for about 10% to 20% of all output produced in an entire year [1]. The accurate prediction of wake deficits is of vital importance for calculating wind farm power output [2], optimizing operations [3], the micro-siting of wind farms [4], etc. Wake models, the most frequently used tool for the prediction of wake effects, are now generally classified into three families: the roughness length-based model, the field model, and the kinematic model. The roughness length-based model treats wind turbines as obstacle elements or roughness elements that impact the atmospheric wind profile, which is specifically used in predicting the wake loss over a large wind farm or the wake interaction between wind farms [5]. The field model, or the computational fluid dynamics (CFD) model solves the Navier–Stokes equation to obtain detailed flow field information [6,7], and has high precision but is time consuming and computationally expensive, which hinders applications in engineering fields that require multiple computations of the wind farm power, such as wind farm layout optimization. The kinematic model (or empirical model) analytically obtains the wake velocity distribution behind a single turbine based on some ideal hypotheses. With the merits of a simple formulation, acceptable precision, and quick calculation speed, it has been widely used in engineering.

Many previous studies have introduced, analyzed, and compared the commonly used empirical wake models in detail [8–11].

One wind turbine may lie within the superimposed area of wakes from upwind turbines, and the interaction mechanism of multiple wakes is not well understood due to the extreme complexity of the turbulent structures within them. The commonly used approach in engineering to simulate the interaction effect of different wakes is to combine the single analytical wake models with some simple assumptions about superposition. When many turbines are aligned with the wind direction, it has been experimentally observed that the second turbine suffers the maximum power loss, while the subsequent turbines have relatively smaller further losses (e.g., turbines in a row under the west wind in the Horns Rev offshore wind farm [12]). Based on this observation, Leuven [13] assumed the given wind turbine was influenced only by the wake from the nearest upwind turbine in his wind farm model (WINDPARK) to calculate power. The result showed that this method obtained a good agreement between its prediction and the measurements in the Zeebrugge wind farm. A more frequently used method is using superposition models to analytically describe the effect of multiple wakes. There are four available superposition models: namely the geometric superposition (GS) model, linear superposition (LS) model, sum of squares (SS) model, and energy balance (EB) model. Among them, the latter three are the most common. They are based on a similar principle that the flow characteristics in the superposed area are caused by the accumulation of all wakes from upwind turbines, while the only distinction is in the different mathematical expressions of wake deficits from the upwind turbines.

To be specific, the LS model was proposed by Lissaman [14] and predicts the velocity deficit of superposed wakes by summing the velocity deficit of all upwind turbines. Crespo [15] argued that this assumption would lead to an overestimation of wake deficit in the superposed area and could even obtain a negative speed for large perturbations. However, when the wake velocity in the interference region is relatively small, such as the wake interaction from upwind turbines abreast of each other, the LS model performs well in predicting the overlapped wake deficit [16]. The SS model was presented by Katic [17] in his classical literature about the Park model and assumes the velocity deficit in the superposed area equals the square root of the sum of squares of the velocity deficit from each upwind turbine. The prediction of this model was verified to be in better agreement with experiments compared to the LS model when many wakes are combined [15]. Voutsinas [18] applied an explicit energy equation to develop the EB model, assuming that the total energy loss in the superposition wake equals the sum of the energy losses for each individual upwind turbine.

In order to evaluate the precision and effect of the different superposition models, Erik [19] compared the model predictions with wind tunnel measurements and found that the SS model could obtain more accurate results for almost all cases, followed by the EB model. Tian [20] integrated the two-dimensional Jensen model into different superposition models to calculate the power loss of the Horns Rev wind farm and reached the same conclusion. In fact, associating the SS model with the classical Jensen model [17,21], also known as the Park model, is the most popular approach to predict the wake deficit of wind farms [22–25] and is also the standard implementation in the wind resource assessment of many commercial software such as WAsP [26] and WindPRO [27], despite being proposed for more than 30 years.

In recent years, the SS model has been found to be unsuitable for simulating deep array effects, as the power outputs calculated for downwind turbines reach a constant too quickly. However, this does not preclude the widespread use of the SS model as before. The GS, LS, and SS models are all experience-based analytical models without definite physical basis, which makes it difficult to improve these engineering interaction models by theoretical analysis and numerical simulation. The only one that employs physics is the EB model, based on a simplified energy equation without considering the energy exchange between the wake region and ambient atmosphere. Kuo [28] took such energy into account and introduced the kinetic energy correction factor to revise the EB model. It is worth noting that the correction factor should be determined experimentally. The author suggested the value of

this factor to be 1 if no measurements or CFD simulation data are available, which corresponds to the conventional EB model. An experimental study by Smith and Taylor [29] found that for a configuration of two turbines in a row, the wake velocity of the downwind turbine recovers more rapidly than the one upwind; i.e., at the same relative position, the velocity deficit of the downwind turbine wake is smaller. This might be because of the higher turbulence level and shear stress profile generated by upwind turbines in the superposed wake area, which enhances momentum diffusion and thus leads to faster wake recovery. In order to reflect this character in the engineering interaction model aiming to improve its precision, this study introduces a mixing coefficient to revise the classical EB model based on this phenomenon and proposes a new interaction wake model with higher accuracy.

This paper is organized as follows. In Section 2, a complete simulation method for wake flow in the wind farm is presented. First, a brief introduction of the single wake model used in this study is given in Section 2.1. Then, a new interaction model that considers the effect of increased turbulence intensity in the superposed area is proposed in Section 2.2. In addition, when predicting the wake flow in a wind farm, the relative location between wind turbines under an arbitrary wind direction is needed, and so a simple and convenient approach for this challenge is provided in Section 2.3. The newly proposed model and method are implemented for the offshore Lillgrund and Horns Rev I wind farms, and the results are compared with measurements in Section 3. Finally, a summary and conclusions are given in Section 4.

2. The New Analytical Wind Farm Wake Model

2.1. Wind Turbine Wake Model

The widely used 1D Jensen model is adopted to quantify the reduction of the downwind wind speed behind a wind turbine in this study. It is a linear wake model based on mass conservation, first proposed by N.O. Jensen [21] of the Denmark Risø Laboratory in 1982. Assuming a circular cylinder wake zone, the width of the wind turbine wake is expanded linearly with increasing downwind distances, and the wake velocity on the cross-section is equal at all spots; i.e., a top-hat distribution. The wind speed in the wake u_w, is a function of the thrust coefficient C_t, and wake decay coefficient k, which can be formulated as:

$$u_w = u_0 \left[1 - \left(1 - \sqrt{1 - C_t} \right) \left(\frac{r_0}{r_0 + kx} \right)^2 \right] \tag{1}$$

where u_0 is the inflow velocity, x is the distance behind the wind turbine, r_0 is the rotor radius, and $r_0 + kx$ is the wake radius at the downwind position x. For a given thrust coefficient and downwind distance, the only adjustable parameter in the Jensen wake model is the wake decay coefficient k, which is sensitive to many factors including the roughness, hub height, turbine-induced turbulence, ambient turbulence, or atmospheric stability. Based on long-term project practice, the value of k recommended in WAsP [26] is 0.075 and 0.05 for onshore and offshore wind farms, respectively. Several analytical models have been developed to estimate the wake decay coefficient, such as in References [9,30,31]. The focus of this paper is on developing the interaction model, and so the recommended values in WAsP that are most widely used are employed in our calculations.

2.2. Wake Superposition

The four frequently used wake interaction models in engineering are listed as follows:

$$\text{Geometric Sum (GS)} \quad \frac{u_i}{u_0} = \prod_{j}^{N} \frac{u_{ji}}{u_j}$$

$$\text{Linear Sum (LS)} \quad \left(1 - \frac{u_i}{u_0}\right) = \sum_{j}^{N}\left(1 - \frac{u_{ji}}{u_j}\right)$$

$$\text{Energy Balance (EB)} \quad u_0^2 - u_i^2 = \sum_{j}^{N}\left(u_j^2 - u_{ji}^2\right)$$

$$\text{sum of Squares (SS)} \quad \left(1 - \frac{u_i}{u_0}\right)^2 = \sum_{j}^{N}\left(1 - \frac{u_{ji}}{u_j}\right)^2$$

where N is the total number of upwind turbines which affect the target wind turbine i by their wakes; u_i is the inflow speed of target turbine i; u_j is the inflow speed of the upwind turbine j; and u_{ji} denotes the wind speed at turbine i due to the single wake from turbine j that can be obtained by using empirical wake models such as the Jensen wake model (Equation (1)).

Except for the GS model, all models first calculate the wake losses of each upwind turbine at the position of the target turbine and then overlay them as the total loss due to upwind turbines. Hence, the only distinction between the superposition models is that the wake deficit is expressed in different ways. Figure 1 gives a schematic for the typical wake superposition along a row of four turbines. As shown, wind turbine 3 is located in the superimposed zone of upwind turbines 1 and 2. When calculating the velocity distribution before turbine 3 in scenario I, first, the superposition should be divided into scenario II and scenario III. Then, the wake deficits caused by turbines 1 and 2 are computed separately and finally combined as the total loss caused by upwind turbine.
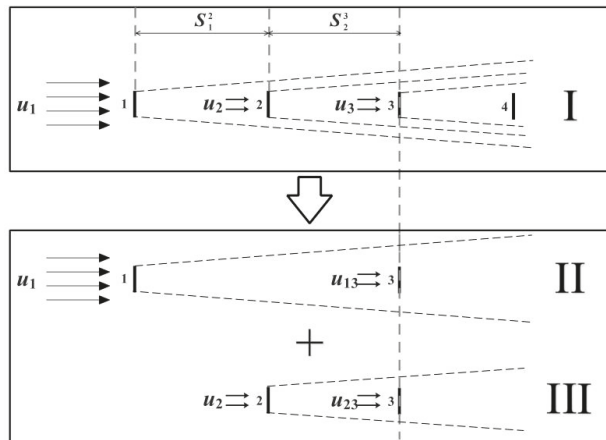

Figure 1. Schematic diagram of three overlapping turbine wakes. The simulation of the inflow velocity at turbine 3 in scenario I is decomposed into scenarios II and III, and then superimposed.

In the far wake region, turbulence plays a leading role in the flow development. The turbulent environment re-energises the low-momentum wake regions within wind farms [32]. The wind speed gradient between the wake and the free flow outside the wake results in additional shear-generated turbulence, which assists the transfer of momentum into the wake from the surrounding flow. Thus the wake and the surrounding flow start to mix. The rate of decay of the velocity deficit is strongly dependent on the ambient turbulence levels [33,34]. As a general rule of thumb [35,36], the stronger the ambient turbulent intensity, the faster the wake recovery. Some wind tunnel experiments and CFD simulations [37,38] have shown that the turbulence intensity in the wake overlay area is higher than that of the undisturbed wind turbine at the same location. Meanwhile, as mentioned above, for a particular experiment of two turbines in a row, the wake velocity of the downwind turbine recovers

more rapidly than that of the upwind one. So this can be explained by the fact that the turbulence level generated by the upwind turbines is higher, which creates more momentum diffusion, leading to a faster recovery in the superposed area. Traditional interaction models are merely the mathematical expressions of the wake losses and simple superimposition. They cannot take account of the effect induced by the increased turbulence intensity. To overcome this limitation, this study multiplies the superimposed total loss—i.e., terms at the right of equal-sign in the traditional models—by a mixing coefficient less than 1 to characterize the faster velocity recovery caused by an increased turbulence intensity in the superposed wake area. The mixing coefficient can be described by an empirical formula as follows:

$$S_{\text{ave}} = \frac{1}{N-1} \sum_{j}^{N-1} S_j^{j+1}$$
$$\alpha = 1 - \frac{d_T}{S_{\text{ave}}}$$

(2)

where S_j^{j+1} refers to the spacing between every two upwind adjacent turbines along the wind direction as shown in Figure 1; d_T is the rotor diameter; and S_{ave} is their average value.

The mixing coefficient can be calculated fast using Equations (2) which is only based on the spacing between upwind turbines. This expression meets two requirements: First, the coefficient is always less than 1 characterizing less total loss in the wake overlay area due to the higher turbulence level. Second, according to some experimental results [39,40], smaller upwind turbine spacing could lead to larger turbulence intensity in the superimposed area. So the mixing coefficient tends to be smaller with denser upwind turbines, which means faster velocity recovery.

With the exception of the EB model, all traditional interaction models are empirical descriptions without a clear physical basis. With this in mind, the mixing coefficient is combined with the EB model, and then the modified energy balance model (MEB for short) is proposed as follows:

$$u_0^2 - u_i^2 = \alpha \sum_{j}^{N} \left(u_j^2 - u_{ji}^2 \right)$$

(3)

Having a similar form to the EB model, the MEB model can be used with ease and no additional complexity is added to the flow field calculation. However, it should be noted that this modification is appropriate only if there are large perturbations in the wake superposition, such as an array of wind turbines along the wind direction. When considering the superposition of two wakes abreast, the relative spacing along the wind direction between the two turbines is 0, so the mixing coefficient which is based on this spacing cannot be solved and the MEB model does not apply. For this case the traditional EB model is recommended to predict the velocity deficit in the interference region.

2.3. Relative Position of Wind Turbines under Arbitrary Directions

When the wind direction changes, the wind turbine conducts yaw control to ensure that the rotor swept plane is always perpendicular to the inflow direction, which changes the relative positions of the turbines and the wake effect. Therefore, determining the relative position of wind turbines efficiently under arbitrary wind direction is a required process for predicting wake deficits [41]. We use a simple method to solve this problem in this research. As shown in Figure 2, north is regarded as 0° and has the established coordinate frame XOY. The coordinate origin can be chosen from any point in the wind farm, and the Y axis points to the 0° wind direction. T1 represents an arbitrary wind turbine with position (x, y). When the wind direction changes to β, the coordinates are rotated β degrees clockwise and a new coordinate system X'OY' is obtained. The coordinates of the wind turbine in frame X'OY' can be obtained by:

$$\begin{pmatrix} x' \\ y' \end{pmatrix} = \begin{pmatrix} \cos\beta & -\sin\beta \\ \sin\beta & \cos\beta \end{pmatrix} \begin{pmatrix} x \\ y \end{pmatrix}$$

(4)
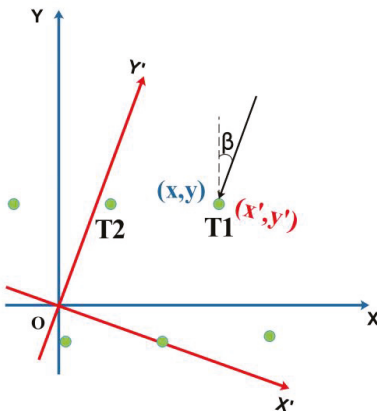
Figure 2. Schematic representation of the coordinate transformation. Green points represent wind turbines.

After the coordinate transformation, the relative positions of the wind turbines can be determined. Combining with the single wake model and the above-mentioned interaction wake model, the wake velocity distribution and power output can be obtained for varying wind directions in wind farm.

3. Benchmarking Study

3.1. Lillgrund Wind Farm

3.1.1. Introduction

The Lillgrund wind farm consists of 48 SWT-2.3-93 Simens wind turbines with a wind rotor diameter of 92.6 m and hub height of 65 m. Since the typical characteristic of this park is that the internal spacing between adjacent turbines is relatively small, the power loss due to the wake effect is bound to be very large. Figure 3 gives the layout of the Lillgrund offshore wind farm. As shown, the turbine spacing is 3.3D and 4.3D rotor diameters under the wind direction of 120° and 222°, respectively.
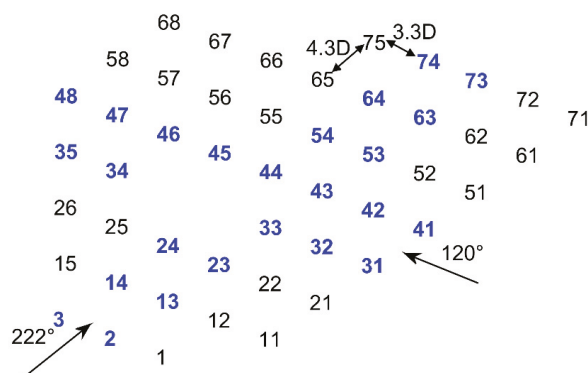
Figure 3. Layout of the Lillgrund offshore wind farm.

3.1.2. Results and Discussion

The co-axial arrangement of wind turbines can be observed in the above two directions. In order to test the accuracy of different models, the Jensen model is combined with three previous interaction wake models (LS, EB, SS) and with the proposed MEB model to calculate the power deficit along rows with and without missing turbines (in blue in Figure 3). The inflow mean velocity at hub height is 9 m/s in all cases. The wake expansion rate of the Jensen model is set to be 0.05 according to the recommended value for offshore conditions. The calculations are performed for various wind directions, consistent with those of the inflow sector of processed SCADA (Supervisory Control and Data Acquisition System) data [−2.5°,2.5°] [11], and are performed in 0.5° steps for both arrays in this research. The results for these cases are given in Figures 4 and 5. The power deficit of the wind turbine can be defined as $1 - P_i/P_0$, where P_i is the actual power of a specific turbine i and P_0 is the power of a turbine not disturbed by a wake.
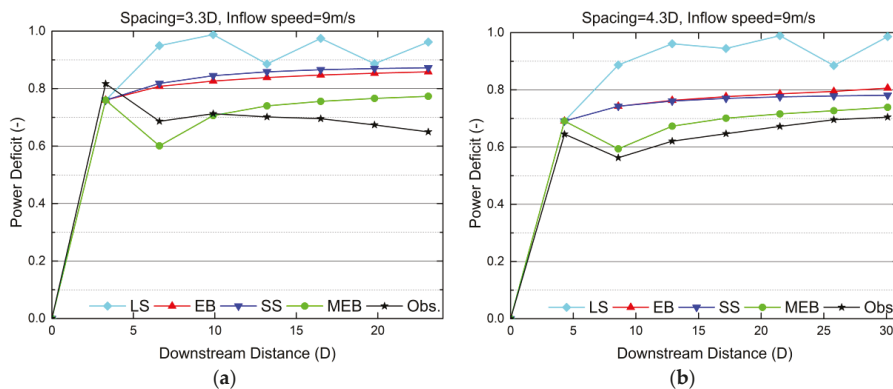
Figure 4. Lillgrund power deficit in a complete row with (**a**) 3.3D spacing and (**b**) 4.3D spacing.
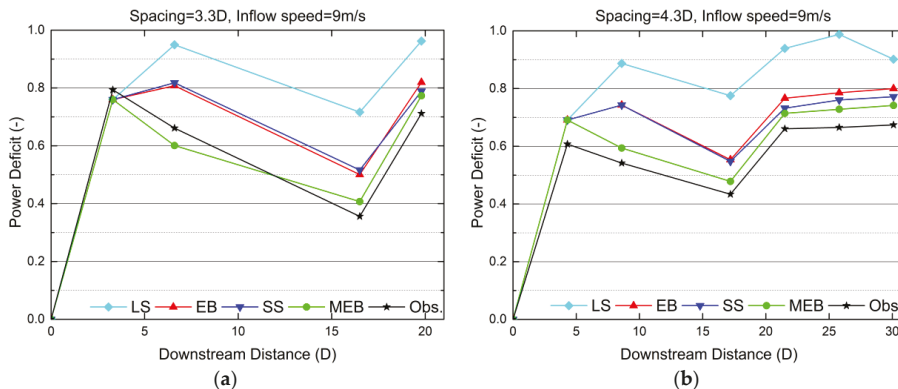
Figure 5. Lillgrund power deficit in a row with (**a**) 3.3D spacing with two missing turbines and (**b**) 4.3D spacing with one missing turbine.

Figure 4 shows the variation of power deficit for different turbine separation distances in the complete arrays along the two directions. In these two cases, the results from the EB model and SS model are very similar, while the LS model seriously over-predicts the deficit and presents a zig-zag pattern. This is because when the calculated inflow is less than the rated speed of the wind turbine, the turbine will stop operating, and no wake is produced in this study. Specifically, without a

superposition effect, the power deficits of the second turbine predicted by different models are the same and reach up to about 82% and 65%, respectively, because of the small spacing. As for the third turbine, the power deficit significantly decreases compared with the former one. Neither of the three typical models could capture this trend, but show rather a continuous decrease of power. Only the proposed MEB model perfectly predicts the power recovery of the third turbine. For the case with 4.3D spacing, the MEB model simulation results of the fourth and subsequent turbines agree very well with observations. However, what should be noted is that none of the superposition models predict the trend of power recovery after the third turbine for the case of 3.3D spacing. Perhaps this is because of the error in the single wake model due to the overly close spacing of 3.3D. Katic [17] also admitted that the calculation of the near-wake zone will involve large errors using the Jensen wake model.

The input data and the characteristics of the cases shown in Figure 5 are more or less the same as in the previous ones, except that some turbines are missing in the studied rows. The absence of turbines causes wakes to further recover to some extent from the third turbine to the fourth. The traditional model results also show this pattern, simply because a smaller predicted inflow before the third turbine leads to a lower overall velocity deficit (the right hand of the model equation) and so a higher inflow before the fourth turbine in the calculation. The MEB model proposed in this study not only catches the sustained power recovery of turbines three and four, but also agrees with the measurements better than the other models in both cases.

In addition to power deficit, the efficiency of the wind farm is another performance indicator measuring the precision of the interaction wake model, which is defined as the ratio between the wind farm actual total output power and the power of the wind farm without considering the wake effect for each turbine. The efficiency can be expressed as:

$$eff = \frac{\sum\limits_{i} P_i}{MP_0} \tag{5}$$

where M is the number of wind turbines in the wind farm. The Jensen model is integrated with four superposition models to calculate the park efficiency under all the wind directions with a span of 3°. In every direction, the inflow mean velocity is 9 m/s. Comparisons of the simulation results with field measurements are given in Figure 6. In general, all the four models could broadly predict the variation of efficiency with changing wind direction and the location of the extreme points. However, there still exist some biases between the model results and observations, especially for the LS model.
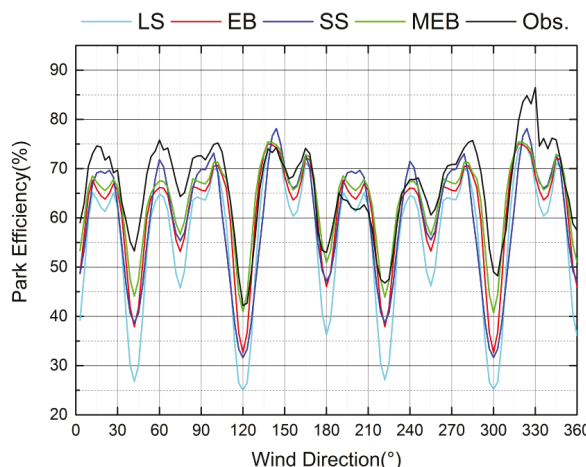

Figure 6. Park efficiency of the Lillgrund wind farm for the inflow sector 0–360° with 3° increments.

To conduct quantitative analysis, the root mean square error (RMSE) and the mean absolute percentage error (MAPE) are adopted to measure the difference between predictions and observations and to evaluate the model performance. Their definitions are as follows:

$$\text{RMSE} = \sqrt{\frac{1}{K}\sum_{i}^{K}(eff_{model,i} - eff_{obs,i})^2} \tag{6}$$

$$\text{MAPE} = \frac{1}{K}\sum_{i}^{K}\left|\frac{eff_{model,i} - eff_{obs,i}}{eff_{obs,i}}\right| \times 100\% \tag{7}$$

where K is the total number of simulated cases in different wind directions; $eff_{model,i}$ and $eff_{obs,i}$ refer to the efficiency from the model prediction and field measurement of the ith given wind direction. The RMSE and MAPE of different model simulation results are listed in Table 1, and the error of models under prevailing wind direction sectors ($240°–270°$) is also shown. It can be seen that under the inflow sector ($0–360°$), the park efficiency calculated by the MEB model reduces the RMSE by 3.79% and decreases the MAPE by 5.3% in comparison to the most commonly used SS model. Moreover, these values are reduced by 1.96% and 2.48%, respectively, in the dominant wind direction range.

Table 1. Simulation error of the park efficiency using different models.

Error	$0°–360°$				Prevailing Wind Directions			
	LS	EB	SS	MEB	LS	EB	SS	MEB
Root mean square error (RMSE) (%)	12.55	7.26	8.99	**5.20**	8.99	4.60	5.07	**3.11**
Mean absolute percentage error (MAPE) (%)	17.06	9.24	11.78	**6.48**	12.84	6.20	6.22	**3.74**

3.2. Horns Rev I Wind Farm

3.2.1. Introduction

The Horns Rev I offshore wind farm is located about 14 km off the west coast of Denmark. It has been extensively studied in evaluating its wake effect and power production, with plenty of meteorological and SCADA data available for comparison. The wind farm consists of 80 Vestas V80 2 MW turbines with a rotor diameter of 80 m and hub height of 70 m. The wind farm's 10 columns and 8 rows are aligned in a parallelogram shape, as seen in Figure 7. The spacing distance between turbines in both lines and columns is 7D, and those under the wind direction of 221° and 312° are 9.4D and 10.4D, respectively.
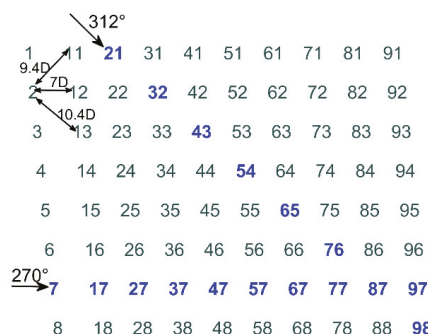
Figure 7. Layout of the Horns Rev I offshore wind farm.

3.2.2. Results and Discussion

The Jensen model is also chosen in this benchmark with $k = 0.05$. Four different interaction models are applied to predict the power deficit of each turbine along rows with an internal spacing of 7D and 10.4D, respectively (in blue in Figure 7). The comparisons between simulation results obtained from different models and extracted SCADA data [22] with an inflow velocity of 7.5 m/s are given in Figures 8 and 9. The cases in Figure 8 correspond to narrow wind direction sizes $[-2°,2°]$, and the cases in Figure 9 correspond to a broader direction interval $[-15°,15°]$, which is considered to decrease the error of wind direction uncertainty as much as possible. All of the runs were performed at a $1°$ step.
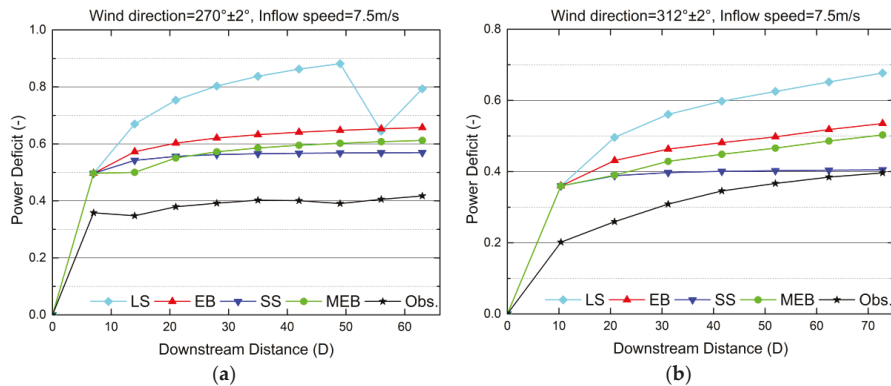
Figure 8. Horns Rev I power deficit in (**a**) a row with 7D spacing and $270 \pm 2°$, and (**b**) a row with 10.4D spacing and $312 \pm 2°$.

When the wind directions are $270°$ and $312°$, the spacing between two turbines undergoes a minimum value of 7D and a maximum value of 10.4D, respectively. Observing the power deficit of the second turbine in Figure 8, there is a large discrepancy when comparing numerical simulations using the Jensen model with wind farm production data. In addition to the reasons for the calculation accuracy of the wake model itself, another important reason is the large wind direction uncertainty included in the datasets while the numerical simulations are carried out for narrow wind direction sectors. Thus, when comparing the performance of different wake interaction models, the primary concern is whether the simulation results can match the changing trend of the measured data. It can be seen from Figure 8a that, with an internal spacing of 7D, the power of the third turbine has recovered more or less compared with the second one. After that, the power deficit tends to gradually increase with a very small range further downwind until the last turbine. The improved MEB model simulation catches the recovery of the power of the third turbine, and the power deficit of the latter turbines increases gradually with a slightly greater amplitude than the measured value. On the other hand, the simulation results of the SS model tend to be in an equilibrium value starting from the third turbine. When the spacing is 10.4D, the power deficit caused by the wake is relatively small due to the larger interval between turbines, and it can be clearly seen from Figure 8b that the deficit along the wind direction increases in steps. At this time, the SS model calculation result, which reach a constant, are obviously inconsistent with the changing trend of the measured values, although the calculated downwind turbine power is closer to the measured value. The power deficit variation curves simulated by the new MEB model and the EB model more closely match the observed values. In fact, the results of the MEB and EB model show the similar changing trend after the third turbine. This is because the MEB model just multiplies a coefficient to the original EB model. In essence, the mathematical structure of these two models is consistent.
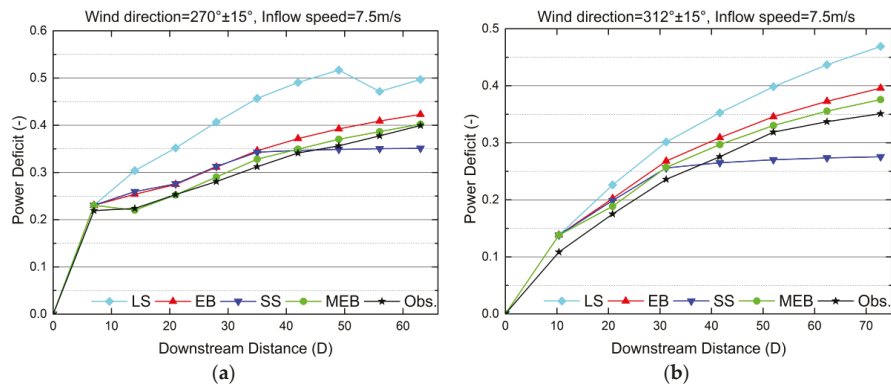
Figure 9. Horns Rev I power deficit in (**a**) a row with 7D spacing and $270 \pm 15°$, and (**b**) a row with 10.4D spacing and $312 \pm 15°$.

With a broader sector $[-15°, 15°]$, the comparisons in Figure 9 show that the Jensen model coupled with interaction models matches much better with all the measured points due to the smaller direction uncertainty error, especially for the new MEB and EB models. The LS model still seriously overestimates the wake loss in the superposition region, while the SS model fails to model the deep array effect as it quickly reaches an equilibrium state. Note that, with the internal spacing of 7D, as seen in Figure 9a, the power of the third turbine restores compared to the second one simulated by the MEB model; nevertheless, the measurements show a slight decrease. This departure may be due to the different frequency of wind directions within the sector $[-15°, 15°]$. The authors in Reference [24] pointed out that a normal distribution fits well with the measured wind direction variations within an averaging period at Horns Rev I around the wind direction of 270°. That is to say, there are a greater number of available measurements for data analysis near 270°, and the number of measurements which are close to the wind direction interval boundary are relatively small. Thus, data for directions near 270°, of which the wake losses of downwind turbines are much heavier, contribute more to the final processing results. However, simulations in this study are performed for a wide range of wind directions ($\pm15°$) with a resolution of 1°. These single simulated powers are then averaged within the range. Therefore, the effect of the cases under directions further away from 270° is overestimated, which results in less deficit in the turbines. In addition, since the turbines are far apart from each other, the upwind wake has restored to a certain degree when it develops to the downwind turbine. The turbulence intensity in the far wake superimposed area tends to be similar to the single wake, which leads to the calculation results of the MEB model and EB being relatively close, as shown in Figure 9b. The farther the spacing, the closer the mixing coefficient is to 1, and so the closer the calculation result of the new model is to the EB model.

Similar models as in the previous benchmark are considered to calculate the park efficiency, and the inflow sector is taken as 0–360° with a span of 5°. In every direction, the inflow mean velocity is 8 m/s. The comparison of the simulation results with measurements is shown in Figure 10. There are significant differences in some wind directions where the wake has a large impact, such as for 0° and 270°. The RMSE and MAPE of different model simulation results are listed in Table 2. It can be seen that under the inflow sector (0–360°), compared with the SS model, the MEB model reduces the wind farm efficiency RMSE by 1.39% and MAPE by 1.58%. Under the dominant wind direction, the wind farm efficiency RMSE decreased by 1.79%, and the MAPE decreased by 2.52%. The results show that for wind farms such as Horns Rev I, which conducts reasonable layout optimization and has a relatively large spacing distance between turbines, the performance of the MEB model has a certain degree of improvement compared with the EB and SS model. However, this improvement is not as good for the Lillgrund wind farm with smaller intervals between turbines.
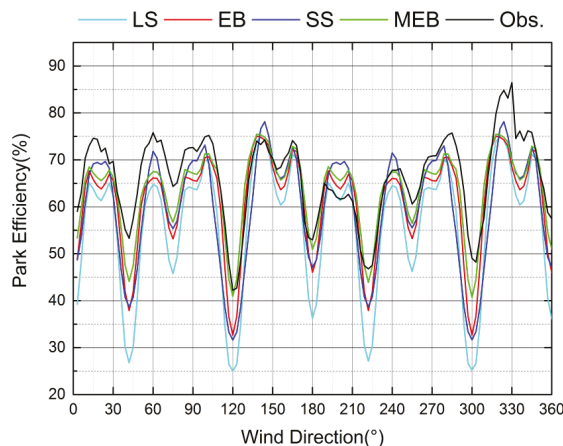
Figure 10. Park efficiency of the Horns Rev I wind farm for inflow sector 0–360° with a 5° increment.

Table 2. Simulation error of park efficiency using different models.

Error	0°–360°				Prevailing Wind Directions			
	LS	EB	SS	MEB	LS	EB	SS	MEB
RMSE (%)	10.04	6.08	6.59	**5.20**	11.65	6.76	7.52	**5.73**
MAPE (%)	8.94	5.92	6.78	**5.20**	10.73	6.70	8.33	**5.81**

4. Conclusions

The conventional interaction wake models separately compute the velocity deficit from each upwind turbine and then linearly superpose them without considering the faster wake recovery caused by a higher turbulence intensity in the superposed wake region, when compared to a single wake area. This omission might contribute to lower model precision. To compensate for this, a new interaction wake model based on the improvement of the energy balance model is proposed to predict the velocity distribution and wind farm power in this paper. A mixing coefficient is introduced to characterize the above phenomenon in the energy balance model, and an empirical expression is also given to calculate this parameter. In order efficiently to provide support for simulating the wake speed distribution under varying wind directions, a simple method to determine the relative position between wind turbines is also given.

A validation of the proposed interaction model is performed using the observations in the Lillgrund and Horns Rev I offshore wind farms, mainly focusing on the power loss of every single turbine and the efficiency of the wind farms. Compared to other commonly used superposition models in engineering, the presented model can better capture the power changing tendency of wind turbines arranged in an array with different spacing, regardless of whether there are missing turbines or not. Especially for turbines in a row in the Lillgrund offshore wind farm with smaller turbine spacing, an obvious power recovery appears at the third turbine, which is only predicted by the presented model. As for the wind farm efficiency, all the interaction models can obtain the changing trend of wind farm output with varying wind direction and determine the location of limit points, while the proposed model in particular is observed to be in better agreement with the measurements.

The proposed interaction model has similar simplicity but higher precision compared with the commonly used interaction models, without increasing the complexity and computational cost of the simulation because the former only multiplies the traditional one by a mixing coefficient. This coefficient is used to characterize the phenomenon that the higher turbulence level and shear stress profile generated by upwind turbines in the superposed wake area leads to a faster wake

recovery, which is obtained by an empirical expression in this paper. Although the modification yields reasonable predictions, a more physical and more accurate model describing the effect of turbulence intensity on the velocity recovery of multiple wakes will be the focus of future research.

References

1. Barthelmie, R.J.; Rathmann, O.; Frandsen, S.T.; Hansen, K.; Politis, E.; Prospathopoulos, J.; Rados, K.; Cabezón, D.; Schlez, W.; Phillips, J.; et al. Modelling and measuring flow and wind turbine wakes in large wind farms offshore. *Wind Energy* **2009**, *12*, 431–444. [CrossRef]
2. Wang, Y.; Liu, Y.; Li, L.; Infield, D.; Han, S. Short-term wind power forecasting based on clustering pre-calculated CFD method. *Energies* **2018**, *11*, 854. [CrossRef]
3. Tian, J.; Zhou, D.; Su, C.; Soltani, M.; Chen, Z.; Blaabjerg, F. Wind turbine power curve design for optimal power generation in wind farms considering wake effect. *Energies* **2017**, *10*, 395. [CrossRef]
4. Herbert-Acero, J.F.; Probst, O.; Réthoré, P.E.; Larsen, G.C.; Castillo-Villar, K.K. A review of methodological approaches for the design and optimization of wind farms. *Energies* **2014**, *7*, 6930–7016. [CrossRef]
5. Peña, A.; Rathmann, O. Atmospheric stability-dependent infinite wind-farm models and the wake-decay coefficient. *Wind Energy* **2014**, *17*, 1269–1285. [CrossRef]
6. Ferrer, E.; Browne, O.M.F.; Valero, E. Sensitivity Analysis to Control the Far-Wake Unsteadiness behind Turbines. *Energies* **2017**, *10*, 1599. [CrossRef]
7. Munters, W.; Meyers, J. Dynamic strategies for yaw and induction control of wind farms based on large-eddy simulation and optimization. *Energies* **2018**, *11*, 177. [CrossRef]
8. Renkema, D.J. Validation of Wind Turbine Wake Models. Master's Thesis, Delft University of Technology, Delft, Holland, 2007.
9. Niayifar, A.; Porté-Agel, F. Analytical modeling of wind farms: A new approach for power prediction. *Energies* **2016**, *9*, 741. [CrossRef]
10. Jeon, S.; Kim, B.; Huh, J. Comparison and verification of wake models in an onshore wind farm considering single wake condition of the 2MW wind turbine. *Energy* **2015**, *93*, 1769–1777. [CrossRef]
11. Göçmen, T.; Laan, P.V.D.; Réthoré, P.E.; Diaz, A.P.; Larsen, G.C.; Ott, S. Wind turbine wake models developed at the technical university of Denmark: A review. *Renew. Sust. Energy Rev.* **2016**, *60*, 752–769. [CrossRef]
12. Hasager, C.B.; Rasmussen, L.; Peña, A.; Jensen, L.E.; Réthoré, P.-E. Wind farm wake: The Horns Rev photo case. *Energies* **2013**, *6*, 696–716. [CrossRef]
13. Van Leuven, J. The Energetic Effectiveness of a Cluster of Wind Turbines. Master's Thesis, Universite Catholique de Louvain, Louvain-la-Neuve, Belgium, 1992.
14. Lissaman, P.B.S. Energy effectiveness of arbitrary arrays of wind turbines. *J. Energy* **1979**, *3*, 323–328. [CrossRef]
15. Crespo, A.; Hernández, J.; Frandsen, S. Survey of modelling methods for wind turbine wakes and wind farms. *Wind Energy* **1999**, *2*, 1–24. [CrossRef]
16. Crespo, A.; Manuel, F.; Hernández, J. Numerical modelling of wind turbine wakes. In Proceedings of the 1990 European Community Wind Energy Conf., Madrid, Spain, 8–12 March 1990; pp. 66–170.
17. Katic, I.; Højstrup, J.; Jensen, N.O. A simple model for cluster efficiency. In Proceedings of the European Wind Energy Association Conference & Exhibition, Rome, Italy, 7–9 October 1986; pp. 407–410.
18. Rados, K.G.; Voutsinas, S.G.; Zervos, A. Wake effects in wind parks. A new modelling approach. In *Scientific Proceedings*; EWEC: Travemunde, Germany, 1993; pp. 444–447.

19. Erik, D. Evaluation of the Software Program Windfarm and Comparisons with Measured Data from Alsvik. Master's Thesis, Royal Institute of Technology, Stockholm, Sweden, 2000.
20. Tian, L.L.; Zhu, W.J.; Shen, W.Z.; Yong, Y.L.; Zhao, N. Prediction of multi-wake problems using an improved Jensen wake model. *Renew. Energy* **2017**, *102*, 457–469. [CrossRef]
21. Jensen, N.O. *A Note on Wind Generator Interaction*; Technical Report Risoe-M-2411(EN); Risø National Laboratory: Roskilde, Denmark, 1983.
22. VanLuvanee, D.R. Investigation of Observed and Modeled Wake Effects at Horns Rev Using WindPRO. Master's Thesis, Technical University of Denmark, Copenhagen, Denmark, 2006.
23. Peña, A.; Réthoré, P.E.; Hasager, C.B.; Hansen, K.S. *Results of Wake Simulations at the Horns Rev I and Lillgrund Wind Farms Using the Modified Park Model*; DTU Wind Energy-E-Report-0026(EN); Risø Campus: Roskilde, Denmark, 2013.
24. Gaumond, M.; Rethoré, P.E.; Ott, S.; Peña, A.; Bechmann, A.; Hansen, K.S. Evaluation of the wind direction uncertainty and its impact on wake modelling at the Horns Rev offshore wind farm. *Wind Energy* **2014**, *17*, 1169–1178. [CrossRef]
25. Gao, X.X.; Yang, H.X.; Lu, L. Optimization of wind turbine layout position in a wind farm using a newly-developed two-dimensional wake model. *Appl. Energy* **2016**, *174*, 192–200. [CrossRef]
26. Mortensen, N.G.; Heathfield, D.N.; Myllerup, L.; Landberg, L.; Rathmann, O. *Getting Started with WAsP 9*; Technical Report Risø-I-2571(EN); Risø National Laboratory: Roskilde, Denmark, 2007.
27. Thørgersen, M.; Sørensen, T.; Nielsen, P.; Grötzner, A.; Chun, S. *WindPRO/PARK: Introduction to Wind Turbine Wake Modelling and Wake Generated Turbulence*; EMD International A/S: Aalborg, Denmark, 2005.
28. Kuo, J.Y.J.; Romero, D.A.; Amon, C.H. A mechanistic semi-empirical wake interaction model for wind farm layout optimization. *Energy* **2015**, *93*, 2157–2165. [CrossRef]
29. Smith, D.; Taylor, G.J. Further analysis of turbine wake development and interaction data. In Proceedings of the 13th BWEA Wind Energy Conf., Swansea, Wales, 20–26 October 1991; pp. 325–331.
30. Frandsen, S. On the wind speed reduction in the center of large clusters of wind turbines. *J Wind Eng. Ind. Aerod.* **1992**, *39*, 251–265. [CrossRef]
31. Peña, A.; Réthoré, P.-E.; van der Laan, M.P. On the application of the Jensen wake model using a turbulence-dependent wake decay coefficient: The Sexbierum case. *Wind Energy* **2016**, *19*, 763–776. [CrossRef]
32. Tobin, N.; Chamorro, L.P. Modulation of turbulence scales passing through the rotor of a wind turbine. *J. Turbul.* **2018**, 1–11. [CrossRef]
33. Burton, T.; Sharpe, D.; Jenkins, N.; Bossanyi, E. *Wind Energy Handbook*; John Wiley & Sons Ltd.: Chichester, UK, 2001; pp. 35–37. ISBN 0-471-48997-2.
34. Makridis, A. Modelling of Wind Turbine Wakes in Complex Terrain Using Computational Fluid Dynamics. Master's Thesis, the University of Edinburgh, Edinburgh, UK, 2012.
35. Crespo, A.; Herna´ndez, J. Turbulence characteristics in wind-turbine wakes. *J. Wind Eng. Ind. Aerod.* **1996**, *61*, 71–85. [CrossRef]
36. Duckworth, A.; Barthelmie, R.J. Investigation and validation of wind turbine wake models. *Wind Eng.* **2008**, *32*, 459–475. [CrossRef]
37. Veisi, A.A.; Shafiei Mayam, M.H. Effects of blade rotation direction in the wake region of two in-line turbines using Large Eddy Simulation. *Appl. Energy* **2017**, *197*, 375–392. [CrossRef]
38. Lee, S.; Vorobieff, P.; Poroseva, S. Interaction of Wind Turbine Wakes under Various Atmospheric Conditions. *Energies* **2018**, *11*, 1442. [CrossRef]
39. Liu, H.; Hayat, I.; Jin, Y.; Chamorro, L.P. On the evolution of the integral time scale within wind farms. *Energies* **2018**, *11*, 93. [CrossRef]
40. Chamorro, L.P.; Porté-Agel, F. Turbulent flow inside and above a wind farm: A wind-tunnel study. *Energies* **2011**, *4*, 1916–1936. [CrossRef]
41. Gu, B.; Liu, Y.; Yan, J.; Li, L.; Kang, S. A wind farm optimal control algorithm based on wake fast-calculation model. *J. Sol. Energy Eng.* **2016**, *138*, 024501:1–024501:6. [CrossRef]

Dynamic Stall of a Vertical-Axis Wind Turbine and Its Control Using Plasma Actuation

Lu Ma, Xiaodong Wang *, Jian Zhu and Shun Kang

Key Laboratory of Power Station Energy Transfer Conversion and System, Ministry of Education, North China Electric Power University, Beijing 102206, China; 1162102037@ncepu.edu.cn (L.M.); 1111170919@ncepu.edu.cn (J.Z.); Kangs@ncepu.edu.cn (S.K.)
* Correspondence: Wangxd@ncepu.edu.cn

Abstract: In this paper, a dynamic stall control scheme for vertical-axis wind turbine (VAWT) based on pulsed dielectric-barrier-discharge (DBD) plasma actuation is proposed using computational fluid dynamics (CFD). The trend of the wind turbine power coefficient with the tip speed ratio is verified, and the numerical simulation can describe the typical dynamic stall process of the H-type VAWT. The tangential force coefficient and vorticity contours of the blade are compared, and the regular pattern of the VAWT dynamic stall under different tip speed ratios is obtained. Based on the understanding the dynamic stall phenomenon in flow field, the effect of the azimuth of the plasma actuation on the VAWT power is studied. The results show that the azimuth interval of the dynamic stall is approximately 60° or 80° by the different tip speed ratio. The pulsed plasma actuation can suppress dynamic stall. The actuation is optimally applied for the azimuthal position of 60° to 120°.

Keywords: DBD plasma actuation; dynamic stall; vertical-axis wind turbine; active flow control

1. Introduction

Dielectric-barrier-discharge (DBD) plasma actuation is an active flow control technology developed in the mid-1960s [1]. The actuator is a plasma-generating device, which is composed of two electrodes, dielectric between the electrodes, and an external high voltage power source. When the actuator is working, the air near the electrode is ionized to ions and electrons. Due to the asymmetry of the electrode arrangement, the ions move in an orientated direction within the electric field, generating a body force that drives the neutral gas molecules to produce a tangential jet, achieving boundary layer flow control. DBD plasma actuation has good performance in boundary layer flow separation control [2], dynamic stall vortex control [3], and so on [4].

The dynamic stall phenomenon can be removed by unsteady pitch control of the blade and the boundary layer separation [5]. Dynamic stall is an inherent feature of VAWT. The angle of attack and relative speed of a blade are changing dramatically during each VAWT rotation cycle. The boundary layer separates and a leading edge vortex is formed on the suction side. This causes the VAWT dynamic stall. Dynamic stall will bring about VAWT structure vibration, noise, and efficiency reduction [6]. VAWT dynamic stall is a complex unsteady flow phenomenon. When the blade moves, the relative velocity and direction are time varying, and the blade is affected by the upstream wake. Although researchers are extremely interested in using flow control methods to improve wind turbine performance [7–10], few researchers have addressed the problem of VAWT dynamic stall. Previous works have only focused on the relationship between the lift/drag and the angle of attack [11], or simply flow field [12,13]. However, there is still a need for investigating the correspondence between the vortex motion and the tangential force of a blade.

There is a considerable amount of research on plasma dynamic stall control for an oscillating airfoil or a flat plate. There is still little knowledge about plasma control of VAWT. In 2006, Post & Corke [3] placed the actuator at the leading edge of NACA0015 airfoil, and the effect of DBD plasma for flow separation and dynamic stall control on an oscillating airfoil was studied experimentally. It was found that the plasma actuation was able to suppress separation and delay stall, and the pulsed actuation was more advantageous. Sato et al. [14] studied the lift enhancement of an oscillating plate by plasma actuation through wind tunnel experiments and numerical simulations. They pointed out that plasma actuation could effectively suppress the flow separation on the flat plate during the up-stroke motion. Phan & Shin [15] using numerical method investigated the impact on the aerodynamic performance at different plasma actuation parameters and actuation positions for an oscillating NACA0012 airfoil. They believed that plasma could increase the lift of the airfoil and suggested to consider the energy consumption of the actuator to achieve the optimal control authority. Greenblatt et al. [16,17] placed a plasma actuator on the leading edge of a small vertical-axis wind turbine and conducted related research. The actuator is placed at the leading edge in a pulsed actuation mode. The results showed that after applying control, the power of the wind turbine increased and the fluctuation decreased, because plasma actuation reduced the leading edge vortex. They also argued that plasma actuation is only effective on the upwind side; however, it was not clear what specific azimuthal interval should be applied actuation. It is valuable and practical to formulate a scientific and economic control strategy to reduce the excited energy consumption and increase the power of the wind turbine.

Two methods can be used to study dynamic stall phenomena: numerical methods [18,19] and wind tunnel experimental methods [20]. Due to the complexity of the VAWT dynamic stall phenomenon, wind tunnel experiments are difficult to capture the full detailed flow field. Therefore, the numerical simulation method is used to study the VAWT dynamic stall problem. The load of VAWT can be calculated using the empirical formula model [21] and the theoretical model [22]. The former is calculated formula fitted by the experimental data, which is easy to implement and low in cost; the latter is mainly solved by the CFD method, and a complex flow field with high kinetic energy and shearing can be obtained, but its more time consuming. Buchner et al. [23] used a theoretical model to study the dynamic stall phenomenon of VAWT and found that the tip speed ratio was less than 3, which significantly reduced the power of VAWT. Most of the dynamic stall effects occur in the low tip speed ratio (less than 3), while the VAWTs actually operate mainly within it, which highlights the industrial relevance of the dynamic stall problem.

A suitable actuator simplified model needs to be selected for numerical simulation of DBD plasma flow control. Shyy et al. [24], Massines et al. [25], Suzen et al. [26], and Abdollahzadeh et al. [27–29] proposed their actuator simplified models based on different assumptions, respectively. The most widely used is the phenomenological model proposed by Shyy et al., which loads the plasma reduced body force into the fluid momentum equation as a source term. The advantages of the Shyy's model are simplicity, fast response, ease of application, and so on. However, the oversimplified model severely overestimates the body forces generated by the plasma actuator. Therefore, the experimental correction of the Shyy's model must be performed before the numerical calculation. The following literature use the corrected Shyy's model for numerical simulation studies [30,31]. Considering the complex unsteadiness of the VAWT dynamic stall and the accuracy of the phenomenological model, in this paper, the modified Shyy's model is selected for numerical simulation.

In this paper, the unsteady CFD method is used to study the dynamic stall phenomenon of VAWT at different tip speed ratios, and the azimuthal position corresponding to the start and end of dynamic stall is found. The modified plasma phenomenological model is used to analyze the influence of plasma actuation on VAWT in different azimuthal intervals. An optimal control strategy for dynamic stall of a vertical-axis wind turbine based on plasma actuation is proposed.

2. Computational Model and Numerical Method

2.1. H-Type VAWT Model

In this paper, a two-dimensional model is used for numerical simulation. The three-blade H-type VAWT model computational domain is shown in Figure 1, which is consistent with the reference [22,32]. *D* represents the diameter of the wind turbine. Inlet, outlet, upper, and lower boundary are 2.5*D*, 4.5*D*, and 2*D* from the VAWT center, respectively.
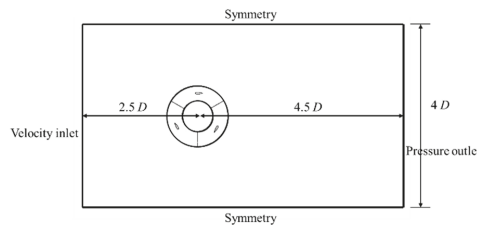

Figure 1. Computational domain and boundary conditions.

The radius of VAWT is $R = 0.3$ m. The blade adopts the NACA0022 airfoil with a chord length c = 0.1 m. The inlet velocity is $U_\infty = 5.07$ m/s. The rotational speed $\omega = 16.9\sim50.7$ rad/s, are studied, corresponding to the tip speed ratio $\lambda = 1$ to 3. θ is the azimuth, and the position where the blade 1 is located in Figure 2 is defined as $\theta = 0°$. $\theta = 0°\sim180°$ is the upwind side, and $\theta = 180°\sim360°$ is the downwind side.
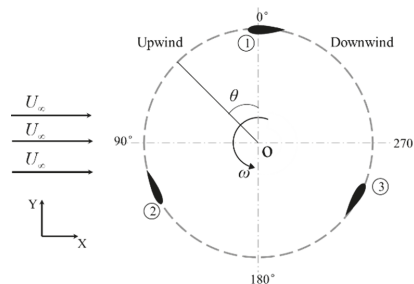
Figure 2. Position of each blade of VAWT.

The plasma actuator is placed at 5~90% c from the leading edge, and the purple triangle represents the plasma region (The actuator is placed at 30% c), as shown in Figure 3.
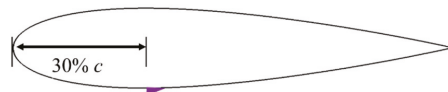
Figure 3. Position of the plasma actuator on a blade.

2.2. Plasma Actuator Model

The Shyy's model [24] simplifies the complex body force generated by plasma into linear electric field force. The basic mechanism of the actuator is shown in Figure 4.

Ignoring the secondary factors, assuming that the plasma density ρ_c is constant and the electric field is linearly distributed, the electric field distribution in the OAB is obtained as

$$\left|\overrightarrow{E}\right| = E_0 - k_1 x - k_2 y \tag{1}$$

where $E_0 = 1.2 \times 10^4$ kV/m is the maximum electric field strength, and the coefficients $k_1 = 1.8 \times 10^9$ kV/m^2 and $k_2 = 3.6 \times 10^9$ kV/m^2 are obtained from the electric field distribution [30].

The body force induced by the plasma actuator can be expressed as electric field force

$$\overrightarrow{F} = \overrightarrow{E}\rho_c e\alpha \tag{2}$$

where $e = 1.602 \times 10^{-19}$ C [24] is elementary charge, and $\rho_c = 1 \times 10^{17}$ m^3 [24]. The $\alpha = 0.3$ is the correction factor [30].

The duty cycle is: $D_{tc} = T_d/T$, where T_d is the duration of the plasma actuation and T is the period.

The original Shyy's model is a great oversimplification; hence, the model used in this paper is calibrated by experiment [33]. In the present study, the height and width of the plasma region in Figure 4 are OA = 2.5 mm and OB = 5 mm [34,35]. In Equation (2), The electric field strength is multiplied by the correction factor of 0.3. Figure 5 is the comparison between the computational and experimental [33] streamwise velocity distribution, where u_p is the plasma reduced velocity, and $u_{p,max} = 5.9$ m/s is the maximum plasma reduced velocity. The ordinate represents the distance from the wall. It can be seen from Figure 5 that the corrected model has a good agreement with the experimental values.
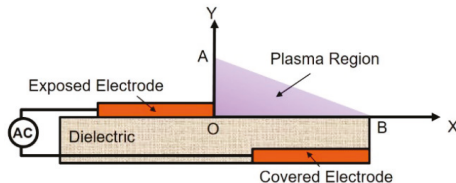

Figure 4. Sketch of the plasma actuator.
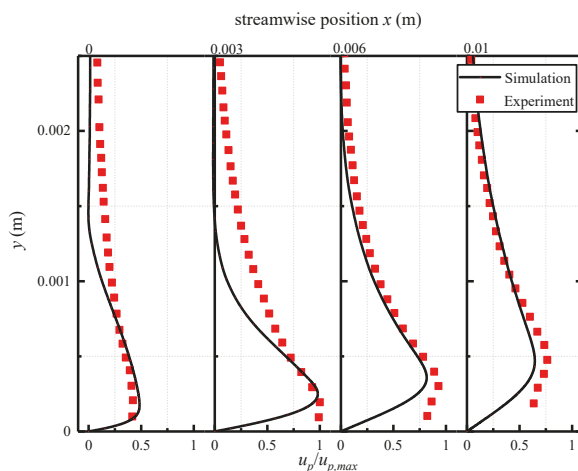
Figure 5. Velocity distribution at different streamwise positions.

2.3. Numerical Method and Boundary Conditions

Figure 6 shows the global mesh of the computational domain. The structured grid is generated, and the total number of cells is 300,000. The sliding mesh is used to establish the rotation domain and the number of cells is 260,000. The grids number along the circumference of a blade is 500. The first cell height of the blade is 0.01 mm, which guarantees $y^+ < 1$, as shown in Figure 7.

Inlet is velocity inlet. Outlet is pressure outlet. Upper and lower boundary are symmetry. The blade surface is a non-slip wall. The electric field force generated by the plasma actuation is loaded as a body force source term though the user-defined function.

Numerical simulations are calculated using ANSYS FLUENT. The turbulence model is k-ω SST model. The blades rotate 0.2 degrees per time step.
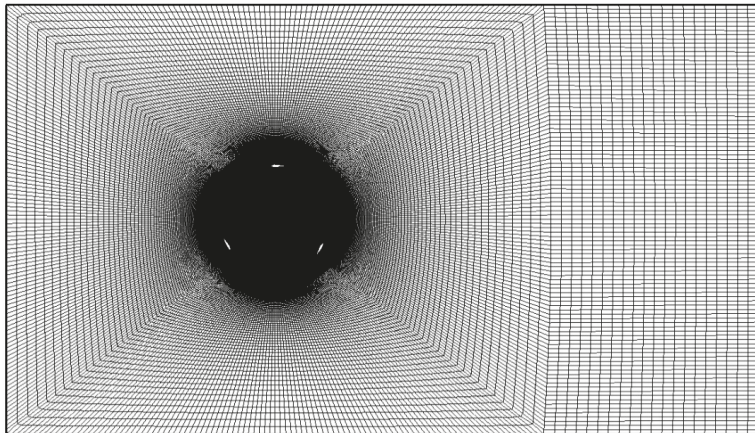
Figure 6. Global mesh of computational domain.
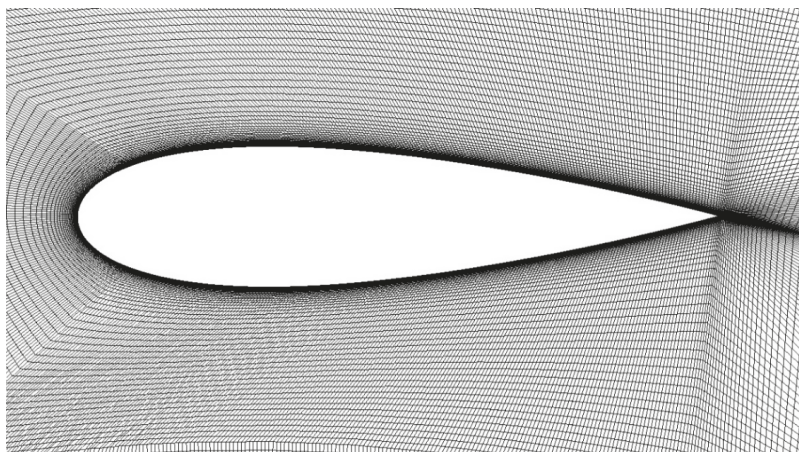
Figure 7. Mesh around the blade.

2.4. CFD Validation

In Figure 8a, grid sensitivity verification is performed on base-line case (U_∞ = 5.07 m/s, λ = 2.15) of three different numbers of cells. As a constant, the first cell height of the blade is 0.01 mm, which guarantees $y^+ < 1$. The grids number along the circumference of a blade are 500, 250, and 125,

respectively. As can be seen from the figure, the difference between the three grids is small. Considering the requirements of the plasma model for the grid, the fine mesh (260,000 cells) is selected.

VAWT dynamic stall is a complex unsteady flow phenomenon; hence, the time step sensitivity verification is necessary. Figure 8b shows the verification of three different the time step sizes on base-line case. It can be seen that large time step size (Δt = 0.0003 s) makes the tangential force larger. Since the frequency of the plasma pulsed actuation is high, the minimum time step size is selected. When the time step size is Δt = 0.0001 s, the blades rotate 0.2 degrees per time step.

It is important and necessary to choose a suitable turbulence model for numerical simulation. A large number of scholars [36–39] have used *k-ω* SST model to solve VAWT problems. Therefore, this paper does not perform additional verification on the turbulence model.

The convergence criterions are that all the parameters was set to 10^{-4} at each time step and the tangential force coefficient of a blade exhibits significant periodicity. Figure 9 shows the variation of the tangential force coefficient with azimuth over 15 cycles. As can be seen from the Figure 9, the solution of the last 10 cycles have converged. In this paper, we use the time average result of the last 10 cycles.
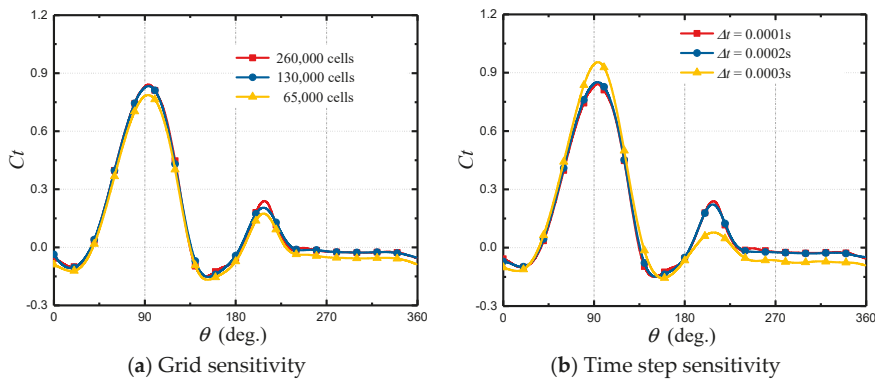

**Figure 8.** CFD validation: the tangential force coefficient with azimuth.
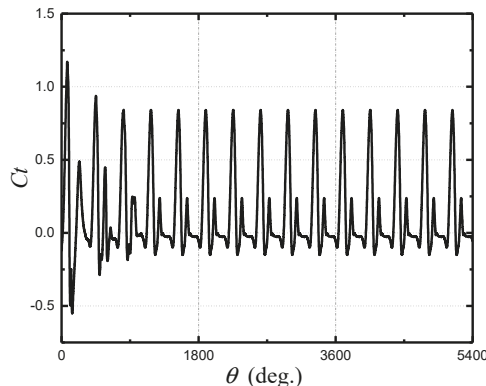
Figure 9. Convergence criterion: the tangential force coefficient with azimuth.

2.5. H-Type VAWT Aerodynamic Parameters

Several major aerodynamic parameters are described below to characterize VAWT dynamic stall.

The tip speed ratio λ is the blade linear velocity to the free stream velocity U_∞, which is used to describe the blades' rotation speed. It is defined as

$$\lambda = R\Omega/U_\infty \tag{3}$$

where R is the radius of the rotor and Ω is the angular velocity of the rotor.

The relative velocity ratio $\hat{U}_{rel}$ is the instantaneous relative velocity of the blade U_{rel} to the free stream velocity. It is defined as

$$\hat{U}_{rel} = \frac{U_{rel}}{U_\infty} \tag{4}$$

The angle of attack based on the instantaneous relative velocity is

$$\alpha_{rel} = \tan^{-1}\left(\frac{\sin\theta}{\lambda + \cos\theta}\right) \tag{5}$$

The α_{rel} varying with azimuth is shown in the Figure 10. It can be seen that the lower the tip speed ratio, the larger the amplitude of α_{rel}.

The tangential force coefficient C_t and the power coefficient C_p represent the ability of the blade and the rotor to generate energy, respectively.

The tangential force coefficient is defined as

$$C_t = \frac{F_t}{1/2\rho U_\infty^2 S} \tag{6}$$

where F_t is tangential force of a blade, and S is the maximum projected area of a blade.

The power coefficient is defined as

$$C_p = \frac{3F_t \cdot \lambda}{1/2\rho U_\infty^2 A} \tag{7}$$

where A is the frontal projected area of wind turbine.
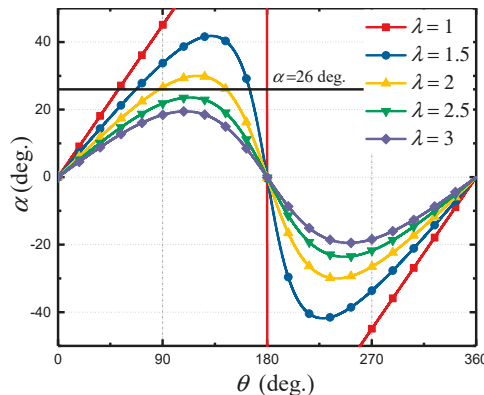
Figure 10. Angle of attack with azimuth.

2.6. Parameter Settings

The research scheme is shown in Table 1. In Scheme 1, the VAWT dynamic stall at five different tip speed ratios is studied. On the basis of Scheme 1, taking $\lambda = 2.15$ as an example, given the actuation duty cycle, and the pulse actuation frequency f, the effects of five plasma actuator positions on VAWT

are investigated. In Scheme 3, given the plasma actuator position, the effects of 10 plasma actuation intervals on VAWT dynamic stall are studied.

Table 1. Parameters of the simulations.

Parameter Settings	λ	Actuator Position	Dtc	f/Hz	Actuation Interval
Scheme 1	1~3	-	-	-	-
Scheme 2	2.15	5 different positions	0.2	383	-
Scheme 3	2.15	0.3c	0.2	383	10 different actuation intervals

3. Results and Discussion

3.1. Computational Results Verification

Figure 11 shows the comparison of the experimental data [32] and the two-dimensional numerical simulation data for wind turbine power coefficient. It can be found that the simulation results of both Zuo et al. [22] and this paper can reflect the variation tendency of C_p, but the numerical values are always larger than the experimental values. Because the two-dimensional numerical simulations ignore the end loss of the three-dimensional blades [40] and the influence of the support structure. Reference [40] pointed out that the two-dimensional URANS simulation can capture most of the details for the VAWT flow field. This paper mainly studies the flow separation and control technology on the VAWT, so the two-dimensional URANS simulation is adopted.
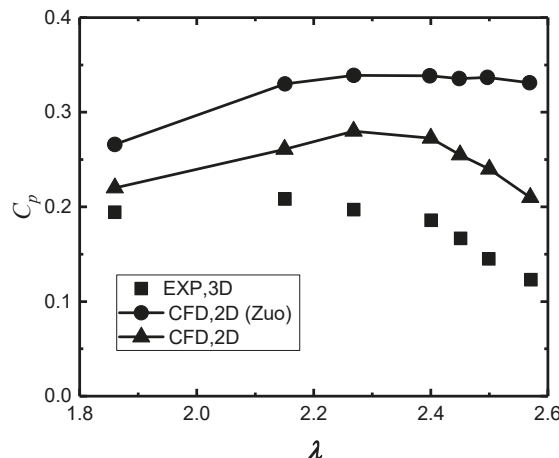

Figure 11. Comparison of experimental data and numerical simulated data for wind turbine power coefficient.

3.2. Influence of Tip Speed Ratio

Five tip speed ratios, $\lambda = 1$, 1.5, 2, 2.5, and 3, were investigated. Figure 12 shows the variation of the blade tangential force coefficient C_t with azimuth at different tip speed ratios. In a rotation cycle, the C_t basically exhibits a double-peak variation. The maximum tangential force coefficient $C_{t\,max}$ and its corresponding azimuth $\theta_{ct.max}$, with increasing tip speed ratio, increase first and then remain unchanged. It can be seen that when the blade moves to the downwind side, the C_t value is around 0 due to the influence of the upstream wakes.
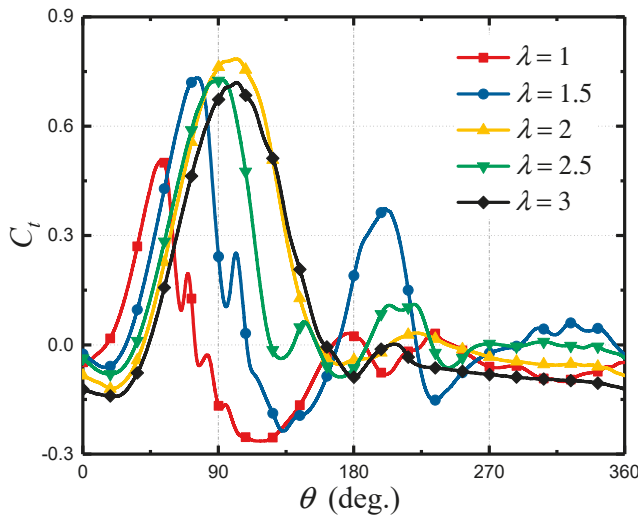
Figure 12. Tangential force coefficient of a blade with azimuth.

In [20], the VAWT consists of NACA0015 airfoil, which is a thin thickness airfoil. The dynamic stall phenomenon of this kind of wind turbine is expressed as the formation, development and shedding of the leading edge vortex on the blade or airfoil. The VAWT selected in this paper consists of the NACA0022 airfoil, which is a medium thickness airfoil. In [41], the aerodynamic performance of the four VAWT airfoils (NACA0012, NACA0022, NACA5522, and LS0421) was compared. The study found that the NACA0022 airfoil performs better at small tip speed ratios. The dynamic stall phenomenon is not exactly the same as the above literature. The main difference is that there is not only the leading edge vortex on the blade, but also a trailing edge vortex with the same direction of rotation.

Figure 13 shows the vorticity (normalized to $c\omega_z/U_\infty$) contour at specific azimuths for blade 1 during a cycle at $\lambda = 1.5$. For ease of understanding, the correspondence between vortex and C_t is indicated by arrows. It should be pointed out that only under this condition, the dynamic stall occurs twice, which is represented by two distinct peaks on the C_t curve, which is the same as the case studied in [11]. The first dynamic stall has gone through four stages a, b, c, and d. The α at point a is small, resulting in a minor C_t. As the angle of attack increases with azimuth, C_t increases significantly. The azimuth of point b corresponds to the maximum of C_t, in which the flow separation from the trailing edge almost rolls up to the leading edge. It can be considered that the movement process of the blade in range a to b is in keeping with the static stall feature. At azimuth c, a leading edge vortex appears, and the vortex adheres to the surface and keep on growing. Under the influence of the leading edge vortex and the non-slip wall condition, a secondary vortex whose rotation direction is opposite to the leading edge vortex is formed. Point d is the minimum of C_t. At this time, the leading-edge vortex extends to one chord length above the suction side, while the boundary layer rolls up and forms a trailing edge vortex close to the surface. Those two vortices interact with each other and obtain circulation in the shear layer to strengthen the vorticity. After that, the leading edge vortex and the trailing edge vortex gradually shed off, and the boundary layer reattaches to the leading edge. The first dynamic stall ends. At the same time, the second dynamic stall occurs on the downwind side. The four typical moments (e, f, g, and h) correspond to the formation, development, and shedding of the leading-edge vortex, and the reattachment of the boundary layer at leading edge. Different from the upwind-side dynamic stall, the trailing edge vortex on the downwind side is not formed on the surface, which is affected by the free flow below the rotor. In this figure, the trajectories of the leading edge vortex and the trailing edge vortex on the upwind and the downwind side can also be observed.
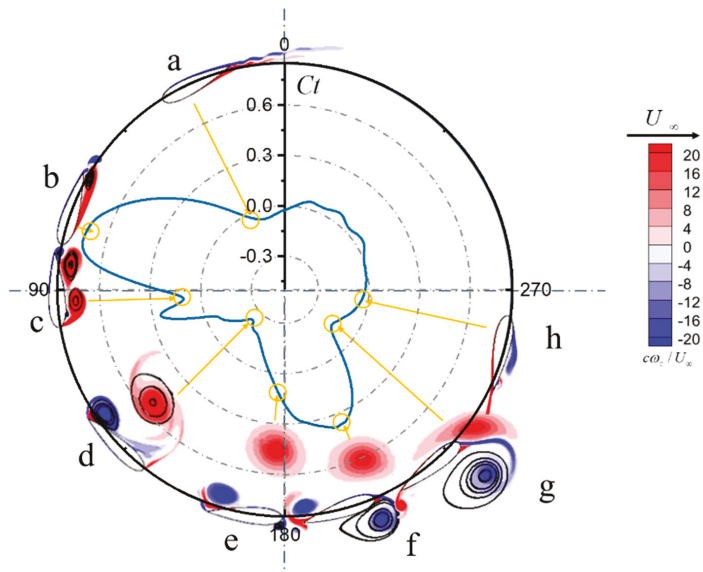
Figure 13. Tangential force coefficient of a blade and vorticity contours with $\lambda = 1.5$.

Figure 14 shows the vorticity (normalized to $c\omega_z/U_\infty$) contours of the blade 1 for selected azimuth at different tip speed ratios. The major vortex structure and its motion state can be clearly observed. The development and their interaction of the leading edge vortex and a pair of trailing edge vortices can be found out. Comparing the vorticity contours, we can see the delay effect of the VAWT dynamic stall at high tip speed ratio. The delay effect means that as the tip speed ratio rises, the VAWT dynamic stall is delayed. The higher the tip speed ratio, the smaller the amplitude of the angle of attack and the relative speed, and the less evidently the dynamic stall occurs.
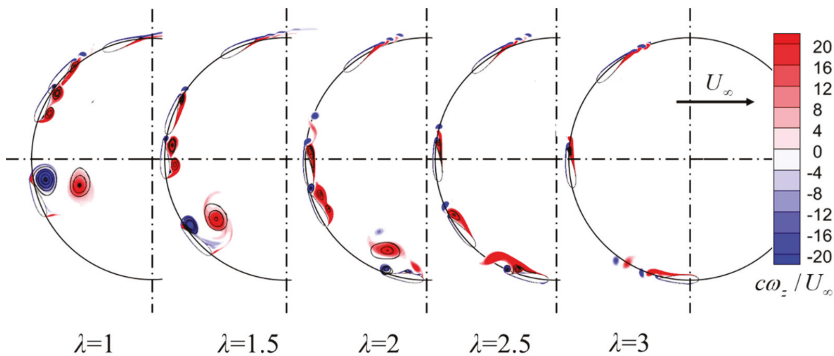

Figure 14. Vorticity contours with different λ for selected azimuth.

Figure 15 shows the vorticity contours for different tip speed ratios at $\theta = 120°$. In order to facilitate the observation and comparison, the coordinates of the blade are transformed. Although the blades rotate to the same azimuth, the vorticity contours are totally different. It can be considered that these five vorticity fields (from $\lambda = 3$ to $\lambda = 1$) can represent the VAWT dynamic stall at different stages. At the same azimuth, the high tip speed ratio corresponds to a small angle of attack, and the dynamic stall delay is more distinct at high tip speed ratios.
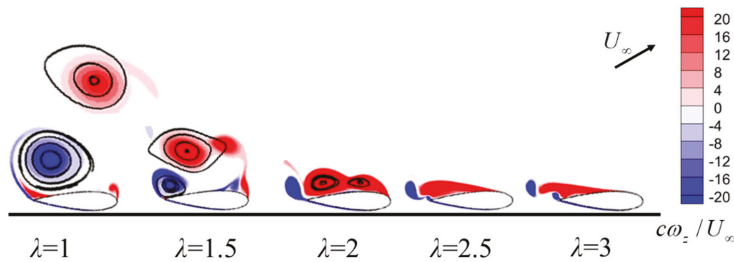
Figure 15. Vorticity contours with different λ at $\theta = 120°$.

Figure 16 shows the azimuth of the maximum tangential force coefficient $\theta_{ct.max}$ as a function of the tip speed ratio, and the horizontal axis is divided by five tip speed ratios. It can be seen from the figure that the $\theta_{ct.max}$ increases first and at a level between 90° and 100° with the increase of λ. Figure 17 shows the angle of attack of the maximum tangential force coefficient $\alpha_{ct.max}$ as a function of the tip speed ratio. It was found that when $\lambda \leq 2$, the $\alpha_{ct.max}$ is approximately above 26°, which is similar to the result observed in [15]. As can be seen from Figure 10, the relative angle of attack of the blade can be higher than 26° only when $\lambda \leq 2$; when $\lambda > 2$, $\theta_{ct.max} = \theta_{\alpha, max}$, where $\theta_{\alpha, max}$ represents the azimuth of the maximum angle of attack, which is also observed in Figure 17. In summary, it can be considered that when the blade moves to an angle of attack higher than 26°, or when moving to the maximum angle of attack (the maximum angle of attack α_{max} is less than 26°), the tangential force reaches a maximum value and the flow begins to stall. The specific reasons have been analyzed above, as shown in Figures 10 and 15.
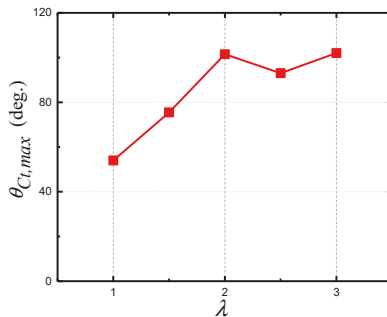

**Figure 16.** $\theta_{ct.max}$ of a blade with λ.
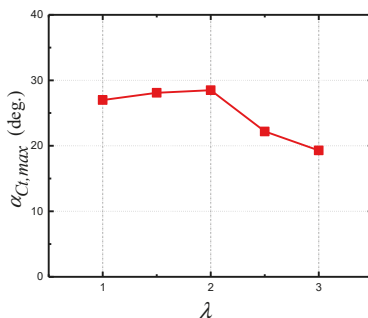
Figure 17. $\alpha_{ct.max}$ of a blade with λ.

Figures 18 and 19 show the change of the azimuth $\theta_{ct.mix}$ and the angle of attack $\alpha_{ct.mix}$ with the tip speed ratio, respectively, where the minimum tangential force coefficient is located. It was found that $\theta_{ct.mix}$ rised with the tip speed ratio, while $\alpha_{ct.mix}$ reduced with the tip speed ratio. The tangential force stall azimuth interval is defined as $\theta_{ct.stall'}$,

$$\theta_{ct.stall'} = \theta_{ct.mix} - \theta_{ct.max}. \tag{8}$$

Figure 20 shows the variation of $\theta_{ct.stall'}$ with the tip speed ratio.

It is found that the tangential force stall azimuth is about $60° \pm 5°$ when the blade is moving at a low tip speed ratio (i.e., $\alpha_{max} > 26°$); while the stall azimuth is about $80° \pm 5°$ at high tip speed ratio.
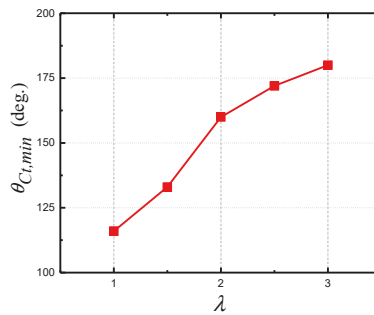
**Figure 18.** $\theta_{ct.mix}$ of a blade with λ.
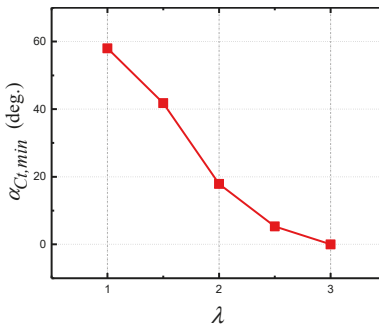


Figure 19. $\alpha_{ct.mix}$ of a blade with λ.
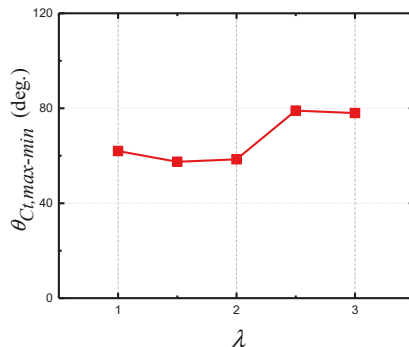

Figure 20. $\theta_{ct.max-mix}$ of a blade with λ.

3.3. Influence of Plasma Actuation Flow Control Strategy on VAWT

In this part, the wind turbine is selected to operate at a tip speed ratio of 2.15. Because according to Figure 11, when the tip speed ratio is 2.15, the wind turbine has a maximum power coefficient in the experiment.

The effect of the plasma actuator positions on VAWT was studied. The actuator is placed at 5% c, 30% c, 50% c, 70% c, and 90% c from the leading edge, respectively. C_p of the VAWT with different plasma actuation positions is shown in Table 2. The baseline case is uncontrolled VAWT rotate at a tip speed ratio of 2.15. In contrast, it has been found that using plasma actuator at these five positions can increase the C_p of the VAWT. The optimal position is at 30% c and the power is increased by 36%. Figure 21 shows the variation of the tangential force coefficient with azimuth at different plasma actuator positions. In general, the actuation increases the maximum tangential force of the blade. At $15° < \theta < 165°$, plasma actuation can significantly increase the tangential force. However, when $\theta > 165°$, the actuation has less effect.

Table 2. C_p with different plasma actuator positions.

| Position of the Plasma Actuator	C_p
Baseline	0.261
5% c	0.324
30% c	0.358
50% c	0.355
70% c	0.315
90% c	0.262
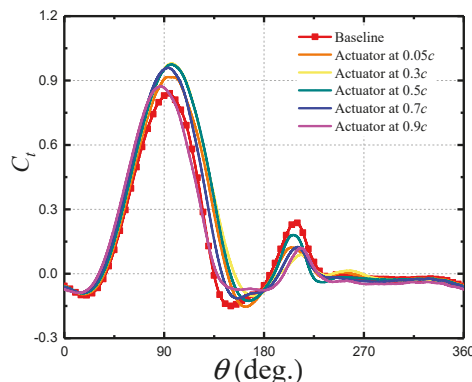
Figure 21. Tangential force coefficient with azimuth at different plasma actuator positions.

Figure 22 shows the relative velocity contour with relative velocity streamlines. The flow fields before and after the controlled (the plasma actuator is at 30% c) were compared. When the actuator is at 30% c, plasma actuation can suppress flow separation, but does not completely eliminate flow separation. The baseline case forms a secondary vortex at $\theta = 135°$, while the controlled case is formed at $\theta = 155°$. Therefore, arranging the plasma actuator at 30% c, plasma actuation will delay the formation of the secondary vortex. It can also be seen from the comparison that the plasma actuation can accelerate the detachment of the vortex on the blade.
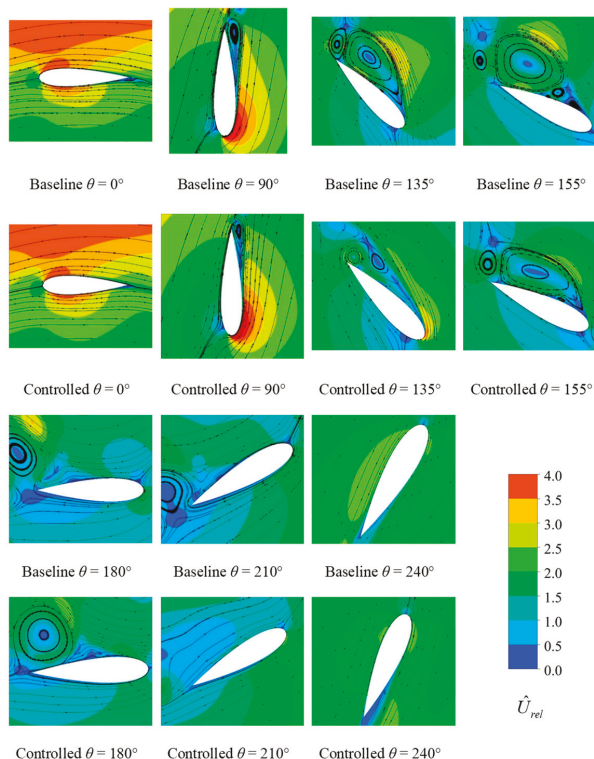
Figure 22. Relative streamlines and relative velocity contours with azimuth for baseline and plasma controlled case (actuator at 30% *c*).

Ten control strategies were studied. The research schemes are shown in Tables 1 and 3. According to that mentioned above, when the tip speed ratio is 2.15, it can be predicted that the H-type VAWT tangential force starts to stall at $\theta = 95° \pm 5°$, and ends the stall at $\theta = 155° \pm 5°$. The plasma actuation control strategies are developed accordingly.

The specific control strategy is shown in Table 3. Case 1 is a baseline and no plasma actuation is applied. In Case 2, the plasma is continuously pulsed on each of the blades during the rotation cycle. In Cases 3–10, the plasma is pulsed in different azimuthal intervals.

Table 3. Strategies of plasma actuation control.

Strategy	Actuation Azimuth Interval	Strategy	Actuation Azimuth Interval
Case 1	No control	Case 6	70° to 150°
Case 2	Global control	Case 7	60° to 150°
Case 3	90° to 160°	Case 8	60° to 130°
Case 4	90° to 150°	Case 9	60° to 120°
Case 5	80° to 150°	Case 10	50° to 110°

Figure 23 shows the variation of the tangential force coefficient with azimuth at the plasma actuation. It can be confirmed from the Case 1 curve that the above prediction is accurate. In general, within $90° < \theta < 180°$, the tangential force coefficient is significantly improved by plasma, and has little effect on other azimuths. Cases 3, 4, and 7–9 show that the end azimuth of the actuation has little impact on the tangential force. Case 4–7 are used to investigate the effect of the starting actuation

azimuth on the tangential force. It is found that the early actuation increases the tangential force and the peak value is higher. Cases 9 and 10 are a set of controlled trials. In the case of the same actuation interval size, the influence of the starting and ending position on the tangential force is studied. There is no significant difference between Case 9 and 10, however, when $\theta > 150°$ the tangential force of Case 10 is lower than Case 9.
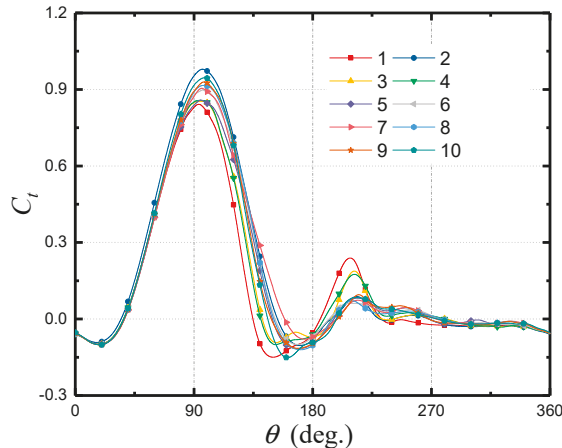

Figure 23. Tangential force coefficient of a blade with azimuth at plasma actuation.

Aerodynamic figure of merit (AFM) [42] is introduced to determine whether the active flow control strategy is cost effective. AFM is defined as

$$\text{AFM} = \frac{P_\text{controlled} - P_\text{actuators}}{P_\text{baseline}} \tag{9}$$

where $P_\text{controlled}$ is the power of controlled VAWT, $P_\text{actuators}$ is the plasma actuators consumption, and P_baseline is the power of uncontrolled VAWT. When AFM > 1, the power consumption of actuators is less than the additional output of VAWT, and the control strategy is feasible.

Table 4 shows the C_p and AFM for different control strategies. The power of VAWT can be directly calculated from the above, and the energy consumption of the plasma exciter is 6.67 W/m [16,17,43]. It can be seen that Case 2 increases the C_p up to 36%, but it is not suitable. Cases 6–10 are feasible, and the maximum C_p can be increased by 34.3%, in which Case 9 is optimal. Considering the consumption of the plasma actuator, Case 9 has the highest AFM value, which means that Case 9 consumes less energy and produces considerable power. Within the scope of the study, it is necessary to apply control in advance to achieve better control results.

Table 4. C_p and AFM at plasma actuation.

Strategy	C_p	AFM	Strategy	C_p	AFM
Case 1	0.261	-	Case 6	0.331	1.033
Case 2	0.358	0.304	Case 7	0.343	1.048
Case 3	0.296	0.928	Case 8	0.331	1.062
Case 4	0.299	0.968	Case 9	0.326	1.072
Case 5	0.310	0.982	Case 10	0.322	1.056

4. Conclusions

In this paper, the phenomenological model and URANS simulation are used to study the VAWT dynamic stall phenomenon with different tip speed ratios. The effects of plasma actuation on the aerodynamic performance of the blade are explored, and the following conclusions are drawn:

1. As the dynamic stall of the vertical-axis wind turbine occurs, the boundary layer separation moves from the trailing edge to the leading edge. The boundary layer will reattach to the blade surface with the leading edge vortex and the secondary vortex shedding. With the increase of the tip speed ratio, the delay effect of the dynamic stall is more obvious.
2. The tip speed ratio affects the maximum and minimum values of the tangential force for a blade. When the tip speed is low, the maximum tangential force is at the azimuth of the $\alpha = 26°$, and the minimum value is at the following $60° \pm 5°$ azimuth. When the tip speed is high, the maximum tangential force is at the azimuth where the maximum angle of attack is, and the minimum is at the following $80° \pm 5°$ azimuth.
3. The pulsed plasma actuation can effectively enhance the power of the vertical-axis wind turbine, and the actuation at $60°$ to $120°$ azimuth is optimal.

Author Contributions: Conceptualization, L.M.; Data curation, L.M.; Formal analysis, L.M.; Funding acquisition, X.W.; Investigation, L.M.; Project administration, X.W.; Supervision, J.Z.; Validation, J.Z. and S.K.; Writing—original draft, L.M.; Writing—review & editing, L.M.

Conflicts of Interest: The authors declare no conflicts of interest.

References

1. Kantrowitz, A.R. A survey of physical phenomena occurring in flight at extreme speeds. In Proceedings of the Conference on High-Speed Aeronautics, New York, NY, USA, 20–22 January 1955; Volume 1955, pp. 335–339.
2. Roth, J.R.; Sherman, D.M.; Wilkinson, S.P. *Boundary Layer Flow Control with a One Atmosphere Uniform Glow Discharge Surface Plasma*; American Institute of Aeronautics and Astronautics: Reston, VA, USA, 1998.
3. Post, M.L.; Corke, T. Separation control using plasma actuators: Dynamic stall vortex control on oscillating airfoil. *AIAA J.* **2006**, *44*, 3125–3135. [CrossRef]
4. Liu, Y.; Kolbakir, C.; Hu, H.; Meng, X.; Hu, H. An experimental study on the thermal effects of duty-cycled plasma actuation pertinent to aircraft icing mitigation. *Int. J. Heat Mass Transf.* **2019**, *136*, 864–876. [CrossRef]
5. McCroskey, W. *The Phenomenon of Dynamic Stall*; NASA TM-81264; National Aeronuatics and Space Administration Moffett Field Ca Ames Research Center: Mountain View, CA, USA, 1981.
6. Araya, D.B.; Dabiri, J.O. Vertical axis wind turbine in a falling soap film. *Phys. Fluids* **2015**, *27*, 091108. [CrossRef]
7. Liu, Q.; Miao, W.; Li, C. Effects of trailing-edge movable flap on aerodynamic performance and noise characteristics of VAWT. *Energy* **2019**, *192*, 58–79.
8. Liu, Q.; Hao, W.; Li, C.; Miao, W.; Ding, Q. Numerical Simulation on the Forced Oscillation of Rigid Riser with Helical Strakes in Different Section Shapes. *Ocean Eng.* **2019**, *191*, 106439. [CrossRef]
9. Zhu, H.; Hao, W.; Li, C. Numerical investigation on the effects of different wind directions, solidity, airfoils and building configurations on the aerodynamic performance of building augmented vertical axis wind turbines. *Int. J. Green Energy* **2019**, *16*, 1216–1230.
10. Miao, W.; Li, C.; Wang, Y.; Xiang, B.; Liu, Q.; Deng, Y. Study of Adaptive Blades in Extreme Environment using Fluid-Structure Interaction Method. *J. Fluids Struct.* **2019**, *91*, 102734. [CrossRef]
11. Zhu, C.; Wang, T. Comparative Study of Dynamic Stall under Pitch Oscillation and Oscillating Freestream on Wind Turbine Airfoil and Blade. *Appl. Sci.* **2018**, *8*, 1242. [CrossRef]
12. Yanzhao, Y.; Guo, Z.; Zhang, Y.; Jinyama, H.; Li, Q. Numerical Investigation of the Tip Vortex of a Straight-Bladed Vertical Axis Wind Turbine with Double-Blades. *Energies* **2017**, *10*, 1721.

13. Qian, C.; Liu, X.; Ji, H.S.; Kim, K.C.; Yang, B. Aerodynamic Analysis of a Helical Vertical Axis Wind Turbine. *Energies* **2017**, *10*, 575.

14. Sato, S.; Yokoyama, H.; Iida, A. Control of Flow around an Oscillating Plate for Lift Enhancement by Plasma Actuators. *Appl. Sci.* **2019**, *9*, 776. [CrossRef]

15. Phan, M.K.; Shin, J. Numerical investigation of aerodynamic flow actuation produced by surface plasma actuator on 2D oscillating airfoil. *Chin. J. Aeronaut.* **2016**, *29*, 882–892. [CrossRef]

16. Greenblatt, D.; Lautman, R. Inboard/outboard plasma actuation on a vertical-axis wind turbine. *Renew. Energy* **2015**, *83*, 1147–1156. [CrossRef]

17. Benharav, A.; Greenblatt, D. Plasma-based feed-forward dynamic stall control on a vertical axis wind turbine. *Wind Energy* **2016**, *19*, 3–16. [CrossRef]

18. Fujisawa, N.; Shibuya, S. Observations of dynamic stall on Darrieus wind turbine blades. *J. Wind Eng. Ind. Aerodyn.* **2001**, *89*, 201–214. [CrossRef]

19. Wang, X.D.; Ye, Z.; Kang, S.; Hu, H. Investigations on unsteady aerodynamic characteristics of a horizontal-axis wind turbine during dynamic yaw process. *Energies* **2019**, *12*, 3124. [CrossRef]

20. Buchner, A.J.; Soria, J.; Honnery, D.; Smits, A.J. Dynamic stall in vertical axis wind turbines: Scaling and topological considerations. *J. Fluid Mech.* **2018**, *841*, 746–766. [CrossRef]

21. Christian, M.; Christophe, L.; Ion, P. Appropriate Dynamic-Stall Models for Performance Predictions of VAWTs with NLF Blades. *Int. J. Rotating Mach.* **1998**, *4*, 129–139.

22. Zuo, W.; Wang, X.; Kang, S. Numerical simulations on the wake effect of H-type vertical axis wind turbines. *Energy* **2016**, *106*, 691–700. [CrossRef]

23. Buchner, A.J.; Soria, J.; Honnery, D.; Smits, A.J. Dynamic stall in vertical axis wind turbines: Comparing experiments and computations. *J. Wind Eng. Ind. Aerodyn.* **2015**, *146*, 163–171. [CrossRef]

24. Shyy, W.; Jayaraman, B.; Andersson, A. Modeling of glow discharge-induced fluid dynamics. *J. Appl. Phys.* **2002**, *92*, 6434–6443. [CrossRef]

25. Massines, F.; Rabehi, A.; Decomps, P.; Ben Gadri, R.; Ségur, P.; Mayoux, C. Experimental and theoretical study of a glow discharge at atmospheric pressure controlled by dielectric barrier. *J. Appl. Phys.* **1998**, *83*, 2950–2957. [CrossRef]

26. Suzen, Y.B.; Huang, G.; Jacob, J.; Ashpis, D. Numerical simulations of plasma based flow control applications. *AIAA Pap.* **2005**, *4633*, 2005.

27. Abdollahzadeh, M.; Páscoa, J.; Oliveira, P.J.; Abdollahzadehsangroudi, M.; Páscoa, J. Modified split-potential model for modeling the effect of DBD plasma actuators in high altitude flow control. *Curr. Appl. Phys.* **2014**, *14*, 1160–1170. [CrossRef]

28. Abdollahzadeh, M.; Pascoa, J.; Oliveira, P.J.; Abdollahzadehsangroudi, M.; Páscoa, J. Implementation of the classical plasma-fluid model for simulation of dielectric barrier discharge (DBD) actuators in OpenFOAM. *Comput. Fluids* **2016**, *128*, 77–90. [CrossRef]

29. Abdollahzadeh, M.; Pascoa, J.C.; Oliveira, P.J. Comparison of DBD plasma actuators flow control authority in different modes of actuation. *Aerosp. Sci. Technol.* **2018**, *78*, 183–196. [CrossRef]

30. Ma, L.; Wang, X.; Zhu, J.; Kang, S. Effect of DBD plasma actuation characteristics on turbulent separation over a hump model. *Plasma Sci. Technol.* **2018**, *20*, 139–149. [CrossRef]

31. Ebrahimi, A.; Hajipour, M. Flow separation control over an airfoil using dual actuation of DBD plasma actuators. *Aerosp. Sci. Technol.* **2018**, *79*, 658–668. [CrossRef]

32. Howell, R.; Qin, N.; Edwards, J.; Durrani, N. Wind tunnel and numerical study of a small vertical axis wind turbine. *Renew. Energy* **2010**, *35*, 412–422. [CrossRef]

33. Maden, I.; Maduta, R.; Kriegseis, J.; Jakirlić, S.; Schwarz, C.; Grundmann, S.; Tropea, C. Experimental and computational study of the flow induced by a plasma actuator. *Int. J. Heat Fluid Flow* **2013**, *41*, 80–89. [CrossRef]

34. Jayaraman, B.; Thakur, S.; Shyy, W. Modeling of fluid dynamics and heat transfer induced by dielectric barrier plasma actuator. *J. Heat Transf.-Trans. ASME* **2007**, *129*, 517–525. [CrossRef]

35. Jayaraman, B.; Shyy, W. Modeling of dielectric barrier discharge-induced fluid dynamics and heat transfer. *Prog. Aerosp. Sci.* **2008**, *44*, 139–191. [CrossRef]

36. Ostos, I.; Ruiz, I.; Gajic, M.; Gómez, W.; Bonilla, A.; Collazos, C. A modified novel blade configuration proposal for a more efficient VAWT using CFD tools. *Energy Convers. Manag.* **2019**, *180*, 733–746. [CrossRef]

37. Bai, H.; Chan, C.; Zhu, X.; Li, K. A numerical study on the performance of a Savonius-type vertical-axis wind turbine in a confined long channel. *Renew. Energy* **2019**, *139*, 102–109. [CrossRef]

38. Sagharichi, A.; Zamani, M.; Ghasemi, A. Effect of solidity on the performance of variable-pitch vertical axis wind turbine. *Energy* **2018**, *161*, 753–775. [CrossRef]

39. Wong, K.H.; Chong, W.T.; Poh, S.C.; Shiah, Y.-C.; Sukiman, N.L.; Wang, C.-T. 3D CFD simulation and parametric study of a flat plate deflector for vertical axis wind turbine. *Renew. Energy* **2018**, *129*, 32–55. [CrossRef]

40. Qin, N.; Howell, R.; Durrani, N.; Hamada, K.; Smith, T. Unsteady flow simulation and dynamic stall behaviour of vertical axis wind turbine blades. *Wind Eng.* **2011**, *35*, 511–527. [CrossRef]

41. Danao, L.A.; Qin, N.; Howell, R. A numerical study of blade thickness and camber effects on vertical axis wind turbines. *Proc. Inst. Mech. Eng. Part A* **2012**, *226*, 867–881. [CrossRef]

42. Stalnov, O.; Kribus, A.; Seifert, A. Evaluation of active flow control applied to wind turbine blade section. *J. Renew. Sustain. Energy* **2010**, *2*, 063101. [CrossRef]

43. Corke, T.; Post, M.L.; Orlov, D.M. Single-dielectric barrier discharge plasma enhanced aerodynamics: Concepts, optimization, and applications. *J. Propuls. Power* **2008**, *24*, 935–945. [CrossRef]

MDPI